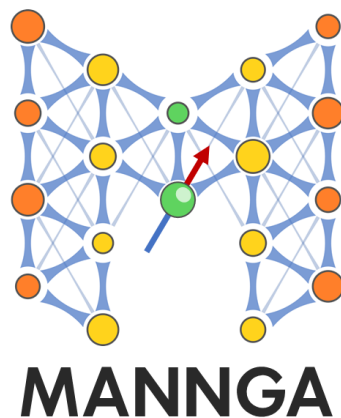


*Theory notes for the MANNGA project (incomplete)*

FIFTEEN MEN  
ON A DEAD MAN'S CHEST



NOVEMBER 8, 2023



# Contents

<b>Contents</b>	<b>1</b>
<b>List of Figures</b>	<b>2</b>
<b>List of Tables</b>	<b>4</b>
<b>I Key concepts: local oscillators in magnonics</b>	<b>5</b>
I.1 A linear driven oscillator . . . . .	5
I.2 A “Kittel dipole” . . . . .	8
I.3 Resonant-level model in one dimension . . . . .	11
I.4 Off-resonant contributions and Fano-like resonances . . . . .	15
<b>II Amplification in parametrically pumped resonators</b>	<b>19</b>
II.1 Parametrically excited oscillator (linear theory) . . . . .	19
II.2 A linear chiral parametric resonator . . . . .	22
II.3 A parametrically pumped Kittel dipole . . . . .	25
<b>III Nonlinear scattering by chiral resonators</b>	<b>27</b>
III.1 Cubic nonlinearities and frequency shifts . . . . .	27
III.2 Nonlinear Kittel modes . . . . .	30
III.3 Nonlinearities in resonant scattering . . . . .	31
<b>IV Multidimensional linear scattering: general framework</b>	<b>34</b>
IV.1 The model . . . . .	34
IV.2 Free propagation and Green’s function . . . . .	35
IV.3 Propagation in the time domain . . . . .	40
IV.4 Dynamics of the resonator and its self-energy . . . . .	41
IV.5 Solving the resonant-scattering problem . . . . .	44
<b>V Two-dimensional scattering in thin magnetic films</b>	<b>47</b>
V.1 Propagating modes in thin films . . . . .	47
V.2 Dipolar coupling between a thin film and a point Kittel dipole . . . . .	51
V.3 The off-resonant coupling . . . . .	59
V.4 Scattering of thin-film modes by large resonators. . . . .	59
<b>VI Modelling large resonators</b>	<b>65</b>
VI.1 Mathematical structure of the LLG equations . . . . .	65
VI.2 Treatment of the Gilbert damping . . . . .	71
VI.3 The near-field approximation . . . . .	73

VI.4	Multi-mode analysis . . . . .	82
VI.5	Semi-realistic case: a large synthetic antiferromagnet . . . . .	86
VI.6	The case of a smaller resonator . . . . .	91
<b>VII</b>	<b>Outlook: nonlinear multidimensional resonators</b>	<b>96</b>

# List of Figures

I.1	Complex plane of $\varphi(t)$ . . . . .	7
I.2	Magnetic precession . . . . .	8
I.3	A rectangular magnonic resonator . . . . .	8
I.4	One-dimensional resonant scattering . . . . .	11
I.5	Purely resonant scattering . . . . .	15
I.6	Circle swept by $T(\omega)$ . . . . .	15
I.7	Fano scattering . . . . .	17
II.1	Parametric transmission (pseudocolor) . . . . .	24
II.2	Parametric transmission . . . . .	24
III.1	Deformation of trajectories under a nonlinear transform . . . . .	28
III.2	Foldover effect in nonlinear resonators . . . . .	33
IV.1	Wavenumber and group velocity for anisotropic dispersion . . . . .	36
IV.2	Propagation in $\mathbf{k}$ -space and in real space . . . . .	38
V.1	Magnons in a thin film . . . . .	47
V.2	Magnon dispersion in a YIG film . . . . .	51
V.3	Green's function in $\mathbf{k}$ -space . . . . .	52
V.4	Constant frequency contour for 1.5 GHz . . . . .	52
V.5	Constant frequency contour for 3 GHz . . . . .	52
V.6	A point-like Kittel dipole is placed at distance $s$ from a film carrying spin waves. . . . .	53
V.7	Directivity of coupling for Damon-Eshbach orientation, 1.5 and 3 GHz, chiral case . . . . .	55
V.8	Directivity of coupling for reverse Damon-Eshbach orientation, 1.5 and 3 GHz, chiral case . . . . .	55
V.9	Directivity of coupling for backward-volume orientation, 1.5 and 3 GHz, chiral case . . . . .	56
V.10	Directivity of coupling for Damon-Eshbach orientation, 1.5 and 3 GHz, non-chiral case . . . . .	56
V.11	Directivity of coupling for reversed orientation, 1.5 and 3 GHz, non-chiral case . . . . .	57
V.12	Directivity of coupling for backward-volume orientation, 1.5 and 3 GHz, non-chiral case . . . . .	57

V.13	Frequency dependence of the emission rate for $d = 20\text{ nm}$ (left panel) and $d = 50\text{ nm}$ (right panel). Different curves correspond to different values of the spacing $s$ . . . . .	59
V.14	Directivity of coupling for a finite-size resonator . . . . .	61
V.15	Scattered wave in $\mathbf{k}$ -space . . . . .	62
V.16	Radiative linewidth for a finite-size resonator . . . . .	63
V.17	Total scattering cross-section for a uniform mode . . . . .	63
V.18	Radiative linewidth for an antiferromagnetic mode . . . . .	64
V.19	Total cross-section for an antiferromagnetic mode . . . . .	64
V.20	Forward and backward scattering . . . . .	64
VI.1	Area of precession ellipse . . . . .	69
VI.2	Phase space trajectory for a one-dimensional mechanical system. The element of the area swept by the trajectory is $d\mathbf{p}d\mathbf{q}$ , integrating it over vertical stripes as shown in the figure yields the abbreviated action $\mathbf{p}\mathbf{q}$ . . . . .	70
VI.3	Area swept by the spin on the unit sphere . . . . .	70
VI.4	Resonator coupled to a medium via near fields . . . . .	74
VI.5	Stray field amplitude . . . . .	78
VI.6	Stray field distribution . . . . .	78
VI.7	Transmission and reflection for a one-dimensional resonator . . . . .	78
VI.8	Precession ellipses in the near-field approximation . . . . .	79
VI.9	Magnetisation distribution in the near-field approximation . . . . .	80
VI.10	Transmission and reflection resonances for $f = 3.94\text{ GHz}$ . . . . .	80
VI.11	Transmission resonances for $f = 1.94\text{ GHz}$ , $s = 100\text{ nm}$ and $s = 200\text{ nm}$ . . . . .	81
VI.12	Transmission resonances for $f = 2.77\text{ GHz}$ , $s = 50\text{ nm}$ and $s = 100\text{ nm}$ . . . . .	81
VI.13	Transmission resonances for $f = 1.80\text{ GHz}$ , $s = 50\text{ nm}$ and $s = 20\text{ nm}$ . . . . .	82
VI.14	Transmission resonances for $f = 2.70\text{ GHz}$ , $s = 20\text{ nm}$ and $s = 10\text{ nm}$ . . . . .	82
VI.15	Transmission resonances for $f = 1.80\text{ GHz}$ , $f = 2.70\text{ GHz}$ , $s = 20\text{ nm}$ and $s = 10\text{ nm}$ . . . . .	84
VI.16	Transmission resonances for $f = 1.80\text{ GHz}$ , $f = 2.70\text{ GHz}$ , $s = 20\text{ nm}$ and $s = 10\text{ nm}$ . . . . .	85
VI.17	Transmission resonances for $f = 1.80\text{ GHz}$ , $f = 2.70\text{ GHz}$ , $s = 10\text{ nm}$ and $s = 20\text{ nm}$ . . . . .	87
VI.18	Magnetisation components in the lowest-lying mode in sAFM . . . . .	88
VI.19	Magnetisation components in the first-excited mode of an sAFM . . . . .	88
VI.20	Phase variation for the lowest-lying modes in sAFM . . . . .	88
VI.21	Radiative linewidth for the two lowest modes of an sAFM . . . . .	89
VI.22	Radiative linewidth for the two lowest modes of an sAFM . . . . .	89
VI.23	Angular dependence of the coupling $\Delta_{\mathbf{k}}$ for the $1.8\text{ GHz}$ mode . . . . .	90
VI.24	Angular dependence of the coupling $\Delta_{\mathbf{k}}$ for the $1.8\text{ GHz}$ mode . . . . .	90
VI.25	Scattered wave function in the $\mathbf{k}$ -space for the $1.8\text{ GHz}$ mode . . . . .	90
VI.26	Scattered wave function in the $\mathbf{k}$ -space for the $3\text{ GHz}$ mode . . . . .	90
VI.27	Frequency dependence of the forward scattering cross-section for both resonant modes. . . . .	91
VI.28	Radiative linewidth for the $4\text{ GHz}$ quasi-uniform mode (left) and $8\text{ GHz}$ dark mode(right) for several values of the spacing. . . . .	92
VI.29	Scattering and absorption cross-sections for a $200 \times 120\text{ nm}$ synthetic antiferromagnet . . . . .	92
VI.30	Scattering cross-section for the $4\text{ GHz}$ and $8\text{ GHz}$ modes . . . . .	92

VI.31	Directivity of the 4 GHz mode . . . . .	93
VI.32	Directivity of the 8 GHz mode . . . . .	93
VI.33	Scattered waves in the $k$ -space . . . . .	93
VI.34	Radiative linewidth for the 4 GHz quasi-uniform mode (left) and 8 GHz dark mode(right) for several values of the spacing. . . . .	94
VI.35	Scattering cross-section for the 4 GHz and 8 GHz modes . . . . .	95

## List of Tables

VI.1	Frequencies of the resonant modes in the near-field approximation . . . . .	77
VI.2	Dissipative linewidths in the near-field approximation . . . . .	77
VI.3	Radiative linewidths in the near-field approximation . . . . .	79
VI.4	Frequencies (in GHz) of the lowest-lying modes for various spacings $s$ between the resonator and the film. . . . .	87
VI.5	Resonant frequencies for a $120 \times 200$ nm resonator (antiparallel) . . . . .	91
VI.6	Resonant frequencies for a $120 \times 200$ nm resonator(parallel) . . . . .	94

# Chapter I

## Key concepts: local oscillators in magnonics

Intermediate goals of the MANNGA project include modelling of spin-wave scattering in chiral resonators, including non-linear effects. In other words, we have to deal with interaction between propagating modes and localised oscillators representing individual resonant modes. The purpose of this chapter is to introduce the models and formalism to describe such systems. We begin by introducing complex-valued variable  $\varphi(t)$  describing an individual oscillating mode in the abstract form. The report will make an extensive use of these variables. An example of a quasi-uniform mode (a Kittel dipole model) is then discussed in this language. We then proceed with a simple model in which one-dimensional propagating modes interact with a local oscillator. This will introduce an important concept of hybridisation coupling  $\Delta$  and radiative contributions  $\Gamma_{L,R}$  to the resonant linewidth. We also show how such a problem can be reduced to a standard driven-oscillator problem, and link the transmission and reflection coefficients to the solution of such a problem. The model involving only resonant scattering, however, is often a rather crude simplification. For this reason, we discuss how the conclusions are modified if a weak non-resonant scattering is also present. We show that the dynamics of the local mode can be still described by a driven oscillator.

Let us also state explicitly the key assumption of our approach. We assume that the resonant non-damped Kittel precession is the dominant effect in dynamics of both local and propagating modes. The dissipation due to Gilbert damping, resonant coupling to the oscillator, nonlinearities of the oscillating modes, and perhaps parametric pumping are considered weak effects on the top of resonant Kittel precession. (The quantitative criterion is obtained by comparing the relevant rates, such as radiative emission rate with the Kittel frequency.) For this reason, we will assume these effects to act additively at short time scales. This will also enable us to focus upon the relevant resonant contributions that accumulate at longer times, mostly ignoring non-resonant terms.

### I.1 A linear driven oscillator

The standard way to represent a linear driven oscillator is as follows:

$$\ddot{x} + 2\Gamma\dot{x} + \Omega_0'^2 x = F(t) . \quad (\text{I.1.1})$$

Here  $x(t)$  is the coordinate of the oscillator at time instant  $t$ , the parameter  $(\Omega'_0)^2$  represents the restoring force,  $\Gamma$  describes energy dissipation, and  $F(t)$  is the external driving. [For an  $RLC$  circuit,  $\Omega'_0 = 1/\sqrt{LC}$ , and  $\Gamma = R/(2L)$ , where  $L$  is the inductance,  $C$  the capacitance, and  $R$  the resistance in the circuit.] For a mass  $m$  on a spring of constant  $k$  with a linear damping force  $-b\dot{x}$ , one finds  $\Omega'_0 = \sqrt{k/m}$  and  $\Gamma = b/(2m)$ .]

Free motion of the oscillator ( $F(t) = 0$ ) is a decaying simple harmonic motion, with a slight shift in the frequency:

$$x_{\text{free}}(t) \propto e^{\pm i\Omega_0 t} e^{-\Gamma t}, \quad \Omega_0 \equiv \sqrt{\Omega'_0^2 - \Gamma^2}. \quad (\text{I.1.2})$$

For this reason, we shall write the equation above in the form

$$\ddot{x} + 2\Gamma\dot{x} + (\Omega_0^2 + \Gamma^2)x = F(t), \quad (\text{I.1.3})$$

so that the parameter  $\Omega_0$  gives the “true” period which can be obtained e.g. by counting zero crossings of the trajectory  $x(t)$ . We also see that the decay rate parameter  $\Gamma$  gives the inverse lifetime of the mode. We shall also refer to it as the linewidth, because it gives half-width at half-maximum of the resonant curve in the linear regime.

In this report, however, we shall describe linear harmonic oscillators differently, by introducing a complex-valued variable  $\varphi(t)$  that obeys the equation

$$i\dot{\varphi} = (\Omega_0 - i\Gamma)\varphi + \Phi(t), \quad (\text{I.1.4})$$

where  $\Phi(t)$  is a complex-valued driving source. (In particular, the resonant level model was defined in terms of such a variable.) To show this, we introduce the real and imaginary components by writing  $\varphi(t) = x(t) + iy(t)$ . Then, the two variables  $x(t)$  and  $y(t)$  obey the system of two first-order equations:

$$\dot{x} = \Omega_0 y - \Gamma x + \text{Im } \Phi(t), \quad (\text{I.1.5})$$

$$\dot{y} = -\Omega_0 x - \Gamma y - \text{Re } \Phi(t). \quad (\text{I.1.6})$$

We can now use the first of the two equations to eliminate  $y(t)$  as follows:

$$y(t) = \frac{\dot{x} + \Gamma x}{\Omega_0} - \frac{1}{\Omega_0} \text{Im } \Phi(t). \quad (\text{I.1.7})$$

This can be substituted into the second equation, so that it takes the form

$$\frac{\ddot{x} + \Gamma\dot{x}}{\Omega_0} - \frac{1}{\Omega_0} \text{Im } \dot{\Phi}(t) = -\Omega_0 x - \frac{\Gamma\dot{x} + \Gamma^2 x}{\Omega_0} + \frac{\Gamma}{\Omega_0} \text{Im } \Phi(t) - \text{Re } \Phi(t). \quad (\text{I.1.8})$$

The latter relation can be simplified to

$$\ddot{x} + 2\Gamma\dot{x} + (\Omega_0^2 + \Gamma^2)x = \text{Im } [\dot{\Phi}(t) + \Gamma\Phi(t)] - \Omega_0 \text{Re } \Phi(t). \quad (\text{I.1.9})$$

Comparing this with Eq.(I.1.3), we see that Eq.(I.1.4) is fully equivalent to it, if we express the force  $F(t)$  in terms of the complex-valued source  $\Phi(t)$  as

$$F(t) = \text{Im} \left[ \left( \frac{d}{dt} + \Gamma - i\Omega_0 \right) \Phi(t) \right]. \quad (\text{I.1.10})$$

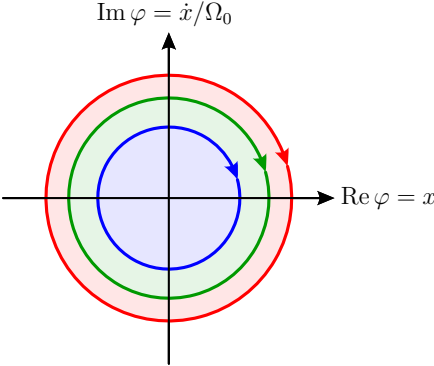


Figure I.1: Complex plane of  $\varphi(t)$  is in fact phase space  $(x, \dot{x})$ . Free motion of an undamped oscillator is represented as circles in this plane.

The meaning of this relation is that it discards the “wrong” mode  $\exp(-\Gamma t + i\Omega_0 t)$  from  $\Phi(t)$  by projecting it out.

The link between  $x(t)$  and  $\varphi(t)$  becomes particularly transparent if one considers free precession of an undamped oscillator. For  $\Gamma = 0$  and  $\Phi(t) = 0$ , one finds  $\varphi = x(t) + i\dot{x}/\Omega_0$ . Thus the complex  $\varphi(t)$  plane is in fact the phase space of the oscillator  $(x, \dot{x})$ . The simple harmonic motion is seen as a circular motion  $\varphi(t) = \varphi_0 \exp(-i\Omega_0 t)$ , see Fig. I.1. Thus,  $\varphi_0$  can be considered as complex-valued amplitude of the oscillations.

In what follows, we shall normalise the oscillating modes via the following requirement: the energy  $E$  of the oscillator takes the form  $E = \Omega_0 |\varphi|^2$ . In other words, the quantity  $|\varphi|^2$  has the meaning of the number of excited quanta. In the Hamiltonian formalism, this also means that the Poisson brackets between the mode components are as follows:

$$\{\text{Im } \varphi, \text{Re } \varphi\} = \frac{1}{2}, \quad \text{or} \quad \{\varphi, \bar{\varphi}\} = i. \quad (\text{I.1.11})$$

(This is the classical analogue of the commutator  $[\hat{a}, \hat{a}^\dagger] = 1$  between the ladder operators  $\hat{a}, \hat{a}^\dagger \propto (\hat{x} \pm i\hat{p})$  of a quantum harmonic oscillator, so that  $\varphi(t)$  and  $\bar{\varphi}(t)$  can be considered as classical analogues of these operators in Heisenberg’s picture.) One may use this fact to introduce the Poisson brackets between two quantities  $F(\varphi, \bar{\varphi})$  and  $G(\varphi, \bar{\varphi})$  in terms of complex-valued variables as

$$\{F(\varphi, \bar{\varphi}), G(\varphi, \bar{\varphi})\} \equiv i \left( \frac{\partial F}{\partial \varphi} \frac{\partial G}{\partial \bar{\varphi}} - \frac{\partial F}{\partial \bar{\varphi}} \frac{\partial G}{\partial \varphi} \right). \quad (\text{I.1.12})$$

In analytical dynamics, equations of motions can be derived from a known Hamiltonian  $H(\varphi, \bar{\varphi})$  via

$$\frac{\partial F}{\partial t} = \{H, F\}. \quad (\text{I.1.13})$$

Applying this relation to the Hamiltonian  $\Omega_0 \varphi \bar{\varphi}$ , one re derives the equations of motion

$$\dot{\varphi} = \{H, \varphi\} = -i\Omega_0 \varphi. \quad (\text{I.1.14})$$

One may also notice that this normalisation brings energy dissipation  $\dot{E}$  to the form  $\dot{E} = -2\Omega_0 \Gamma_0 |\varphi|^2$ , which may be helpful in identifying the damping  $\Gamma_0$  from a microscopic model.

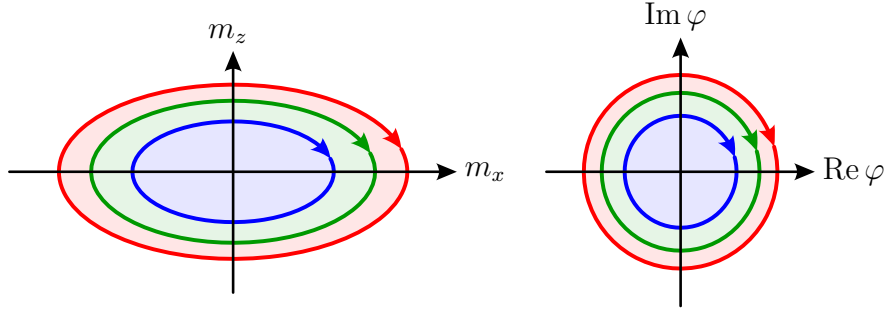


Figure I.2: Magnetic precession in a Kittel mode and the corresponding trajectories in the  $\varphi$  plane.

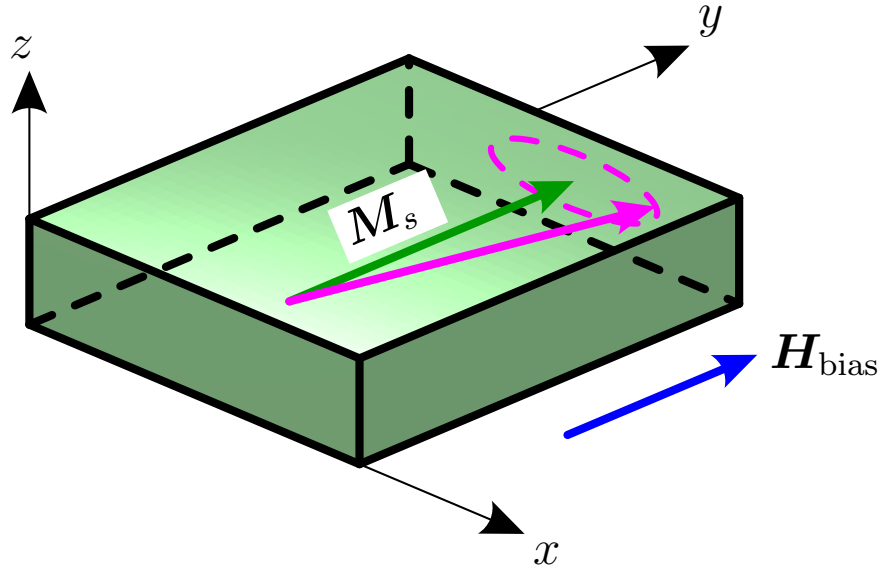


Figure I.3: A rectangular magnetic resonator with uniform saturation magnetisation  $M_s$  (green) is magnetised along the  $y$  axis and biased by the field  $\mathbf{H}_{\text{bias}}$  (blue). Dynamical magnetisation components  $m_x$  and  $m_z$  circumscribe an ellipse in the  $xz$  plane (magenta).

## I.2 A “Kittel dipole”

An example of a linear oscillator described above is a quasi-uniform Kittel mode (QUM). Consider a magnet with static saturation magnetisation  $M_s$  directed along the  $\hat{\mathbf{y}}$  axis, biased by the field  $H_{\text{bias}}\hat{\mathbf{y}}$  as shown in Fig. I.3. In this setup, the only active magnetisation components are  $m_x$  and  $m_z$ , which we find convenient to treat as dimensionful quantities, with units of  $M_s$ . (Dimensionless magnetisation components often employed elsewhere are  $m_{x,z}/M_s$ .) The dipolar coupling results in a demagnetising field which can be approximated as uniform<sup>1</sup>:  $H_x \approx -N_x m_x$ ,  $H_z \approx -N_z m_z$ , with demagnetisation coefficients  $N_x$  and  $N_z$  along the two perpendicular axes. (The effects of magnetic anisotropy can be also incorporated into the demagnetising tensor.) The dynamical magnetisation ( $m_x$ ,  $m_z$ ) obeys the linearised Landau-Lifshitz-Gilbert equations that take the form

$$\dot{m}_x - \alpha \dot{m}_z = \Omega_z m_z , \quad (\text{I.2.1})$$

$$\dot{m}_z + \alpha \dot{m}_x = -\Omega_x m_x , \quad (\text{I.2.2})$$

<sup>1</sup> If the shape of the magnet is an ellipsoid, the demagnetising field is indeed uniform

where  $\alpha$  is the Gilbert damping. The two frequencies  $\Omega_x$  and  $\Omega_z$  in Eqs.(I.2.1) are the parameters that characterise the precession, and (I.2.2) are given by

$$\Omega_{x,z} = \gamma_s \mu_0 (H_{\text{bias}} + N_{x,z} M_s) , \quad (\text{I.2.3})$$

with  $\gamma_s \equiv g_s e / (2m_e)$  the gyromagnetic ratio for  $g$ -factor  $g_s \approx 2$ , and  $\mu_0$  the magnetic constant. Writing  $m_{x,z} \propto \exp(-i\omega t)$ , one finds the eigenvalue equation

$$\omega^2 = (\Omega_x - i\omega\alpha)(\Omega_z - i\omega\alpha) . \quad (\text{I.2.4})$$

Its solution for  $\alpha \ll 1$  can be written in the form

$$\omega = \Omega_0 - i\Gamma_0 , \quad \Omega_0 \equiv \sqrt{\Omega_x \Omega_z} , \quad \Gamma_0 \equiv \frac{\alpha}{2}(\Omega_x + \Omega_z) . \quad (\text{I.2.5})$$

The magnetic energy of the mode can be written as

$$\begin{aligned} E &= -\mu_0 V \mathbf{H} \cdot \mathbf{M} = \mu_0 V H_{\text{bias}} M_y + \frac{\mu_0 V}{2} (N_x m_x^2 + N_z m_z^2) \\ &= \frac{V}{2\gamma_s M_s} (\Omega_x m_x^2 + \Omega_z m_z^2) , \end{aligned} \quad (\text{I.2.6})$$

where  $V$  is the volume of the resonator. Here we have employed the relation

$$M_y = \sqrt{M_s^2 - m_x^2 - m_z^2} \approx M_s - \frac{m_x^2 + m_z^2}{2M_s} . \quad (\text{I.2.7})$$

The eigenvectors of Eqs. (I.2.1), (I.2.2) are proportional to  $(\sqrt{\Omega_z}, \pm i\sqrt{\Omega_x})$ . Taking this into account, we define the complex-valued mode variable  $\varphi(t)$  via

$$\boxed{\varphi(t) = \sqrt{\frac{V}{2\gamma_s M_s \Omega_0}} (\sqrt{\Omega_x} m_x \pm i\sqrt{\Omega_z} m_z)} . \quad (\text{I.2.8})$$

Indeed, if one computes  $i\dot{\varphi}$  with the help of Eqs. (I.2.1), (I.2.2), one finds

$$i\dot{\varphi} = C \left( i\sqrt{\Omega_x} \Omega_z m_z + \sqrt{\Omega_z} \Omega_x m_x \right) = \sqrt{\Omega_x \Omega_z} \varphi , \quad (\text{I.2.9})$$

where  $C$  is the normalisation coefficient in Eq. (I.2.8). Thus, Eq. (I.1.4) is indeed obeyed by the mode  $\varphi(t)$ . The energy (I.2.6) then takes the form  $E = \Omega_0 |\varphi(t)|^2$ . Free precession of  $\varphi(t)$  of the form  $\varphi(t) = \varphi_0 \exp(-i\Omega_0 t)$  describes magnetisation  $\mathbf{m}(t)$  precessing with ellipticity  $e_{xz} \equiv \sqrt{\Omega_x / \Omega_z}$ , see Fig. I.2:

$$m_x = A_x \cos(\Omega_0 t + \arg \varphi_0) , \quad m_z = \pm A_x e_{xz} \sin(\Omega_0 t + \arg \varphi_0) , \quad (\text{I.2.10})$$

with amplitude  $A_x = C|\varphi_0|\sqrt{\Omega_x}$ . The above expression for  $\varphi(t)$  can be also rewritten in the form

$$\boxed{\varphi(t) = \sqrt{\frac{V}{2\gamma_s M_s}} (e_{xz}^{1/2} m_x \pm i e_{xz}^{-1/2} m_z)} . \quad (\text{I.2.11})$$

The two magnetisation components  $m_x$  and  $m_z$  play the roles of the coordinate  $x$  and momentum  $\dot{x}$ .

It is also instructive to derive the above equation for  $\varphi(t)$  via a different method. First, the expression for  $\varphi$  should ‘rectify’ precession of ellipticity  $e_{xz}$  into a circular motion, which yields the ratio of the two coefficients in  $\varphi(t)$ . To determine their magnitudes, one may recall that components of angular momentum  $\mathbf{J}$  of the magnet obey the Poisson brackets (or quantum commutation relations)

$$\{J_x, J_z\} = -J_y . \quad (\text{I.2.12})$$

For a uniformly magnetised body of volume  $V$  with a fixed gyromagnetic ratio  $\gamma_s$ , one may write

$$J_{x,z} = \frac{m_{x,z}V}{\gamma_s} , \quad J_y \approx \frac{M_s V}{\gamma_s} . \quad (\text{I.2.13})$$

(In the linear approximation, one may approximate  $M_y$  by  $M_s$ .) Hence

$$\{m_z, m_x\} = \frac{\gamma_s M_s}{V} . \quad (\text{I.2.14})$$

(In other words, the two dynamical components of the magnetisation can be treated as the position and momentum of the relevant oscillator.) Therefore, defining  $\varphi(t)$  as in Eq.(I.2.8) above, one finds  $\{\varphi, \bar{\varphi}\} = i$ .

The latter observation can be generalised to non-uniform modes which could include the effects of exchange fields, etc. Solving the LLG equations, one finds the eigenmodes  $m_x^{(\nu)}(\mathbf{r})$ ,  $m_z^{(\nu)}(\mathbf{r})$  where  $\nu$  enumerates the individual modes. The frequencies  $\Omega_\nu$  of the modes can be positive or negative. But as the full solution is supposed to be real-valued, it suffices to consider positive-frequency modes only. Solution of the linear system yields the modes only up to a constant normalisation factor. The latter should be determined via the normalisation condition (see Sec. VI.1 for derivation and discussion)

$$\text{Im} \int_V d^3\mathbf{r} \bar{m}_x^{(\nu)}(\mathbf{r}) m_z^{(\nu)}(\mathbf{r}) = -2\gamma_s M_s , \quad (\text{I.2.15})$$

which corresponds to a single magnon in the mode. (If the static magnetisation texture  $\mathbf{M}_s(\mathbf{r})$ , one should define local coordinate frame with  $x$  and  $z$  axes perpendicular to  $\mathbf{M}_s(\mathbf{r})$ , and state the normalisation condition (I.2.15) in terms of these local axes.) One may also show that different modes  $\nu' \neq \nu$  obey the orthogonality condition:

$$\int d^3\mathbf{r} [\bar{m}_x^{(\nu)}(\mathbf{r}) m_z^{(\nu')}(\mathbf{r}) - \bar{m}_z^{(\nu)}(\mathbf{r}) m_x^{(\nu')}(\mathbf{r})] = 0 . \quad (\text{I.2.16})$$

Then, writing the magnetisation components as a sum over all the modes,

$$m_{x,z}(t, \mathbf{r}) = \text{Re} \sum_\nu m_{x,z}^{(\nu)}(\mathbf{r}) \varphi_\nu(t) , \quad (\text{I.2.17})$$

one can bring the energy to the form of a collection of independent oscillators:

$$E = \sum_\nu \Omega_\nu |\varphi_\nu|^2 , \quad (\text{I.2.18})$$

where  $\Omega_\nu$  is the respective eigenvalue. For a uniform mode, this gives

$$m_x^{(\text{uni})}(\mathbf{r}) = \sqrt{\frac{2\gamma_s M_s}{V}} e_{xz}^{-1/2} , \quad m_z^{(\text{uni})}(\mathbf{r}) = -i \sqrt{\frac{2\gamma_s M_s}{V}} e_{xz}^{1/2} . \quad (\text{I.2.19})$$

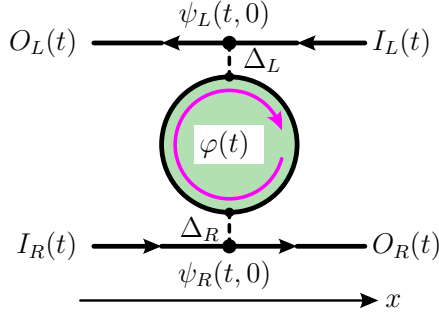


Figure I.4: Resonant mode coupled to two propagating modes in a one-dimensional channel.

When a Kittel dipole is placed in a dynamical external field with components  $h_x(t)$  and  $h_z(t)$ , the field can be viewed as a driving source. The resulting contribution to the LLG equations are

$$\dot{m}_x = \dots + \gamma_s \mu_0 M_s h_z(t) , \quad \dot{m}_z = \dots - \gamma_s \mu_0 M_s h_x(t) . \quad (\text{I.2.20})$$

Computing the respective contributions into  $i\dot{\varphi}$  defined by Eq. (I.2.8), one obtains the source

$$i\dot{\varphi} = \dots + \Phi_h(t) , \quad \Phi_h(t) \equiv i\mu_0 \sqrt{\frac{V\gamma_s M_s}{2}} [e_{xz}^{1/2} h_z(t) \pm ie_{xz}^{-1/2} h_x(t)] . \quad (\text{I.2.21})$$

One may notice that the responses to two circular polarisations are determined by the quantities  $(1 \pm e_{xz})$ . A resonator with  $N_x \approx N_z$  is therefore chiral: it responds only to either left or right circular polarisation, depending upon orientation of its saturation magnetisation  $M_s$ ; the coupling to the spin wave of opposite handedness is suppressed.

### I.3 Resonant-level model in one dimension

To describe a single resonant mode coupled to a waveguide, as shown in Fig. I.4, one may employ the following approximation. The resonant mode by itself can be described by a complex-valued mode  $\varphi(t)$ . Let the right- and left-propagating modes be  $\psi_R(t, x)$  and  $\psi_L(t, x)$  respectively. We then introduce the following Hamiltonian:

$$H = \Omega_0 |\varphi|^2 \int dx \left[ -iv_R \bar{\psi}_R \partial_x \psi_R + iv_L \bar{\psi}_L \partial_x \psi_L \right] + \Delta_R \varphi \bar{\psi}_R(x=0) + \Delta_L \varphi \bar{\psi}_L(x=0) + \text{c.c.} \quad (\text{I.3.1})$$

Here  $v_R$  and  $v_L$  represent group velocities of the modes, obtained by linearising their spectrum  $\omega(k)$  in the vicinity of the resonant frequency:  $\omega(k) = \Omega_0 \pm v_{R,L}(k - k_{R,L})$ , so that  $v_{R,L} > 0$ . The parameters  $\Delta_{R,L}$  describe hybridisation<sup>2</sup> between the propagating modes and the local resonance. The hybridisation couplings, in general, are complex-valued, and have units of  $[L]^{1/2}/[T]$ , where  $[L]$  represents the distance unit, and  $[T]$  the time unit. Then, the modes obey the following

<sup>2</sup> In what follows, the hybridisation coupling  $\Delta$  will be defined in such a way as to make the amplitude of the wave emitted into the channel to be proportional to  $\Delta$ , see Eqs.(I.3.3) and (I.3.4) below. This definition is opposite to the one given in the PRB paper.

equations:

$$\begin{aligned} i\frac{\partial\psi_R}{\partial t} &= -iv_R\frac{\partial\psi_R}{\partial x} + \Delta_R\delta(x)\varphi(t) , \\ i\frac{\partial\psi_L}{\partial t} &= iv_L\frac{\partial\psi_L}{\partial x} + \Delta_L\delta(x)\varphi(t) , \\ i\dot{\varphi} &= (\Omega_0 - i\Gamma_0)\varphi + \bar{\Delta}_R\psi_R(t, x = 0) + \bar{\Delta}_L\psi_L(t, x = 0) . \end{aligned} \quad (\text{I.3.2})$$

The parameters  $\Omega_0$  and  $\Gamma_0$  are the eigenfrequency and decay rate of the resonance. Note that the couplings are complex-conjugated to each other, this follows from the Hermitianness of the respective Hamiltonian operator, i.e., from real-valuedness of the total energy. (In general, the couplings are only proportional to complex-conjugated reciprocal counterparts. To eliminate the proportionality constant, one has to normalise the mode  $\varphi(t)$  per one magnon, as was explained above. This makes the variables  $\varphi(t)$  and  $\bar{\varphi}(t)$  a classical counterpart of the quantum ladder operators  $\hat{a}$  and  $\hat{a}^\dagger$ .) The Hamiltonian introduced here corresponds to the well-known rotating-wave approximation in optics, when only the resonant terms of the form  $\hat{a}\hat{b}^\dagger$  are retained, so that each term in the Hamiltonian preserves the total number of excitations in the system. Classically, this can be justified by noting that for  $\psi_{R,L} \propto \exp(-i\Omega_0 t)$ ,  $\varphi(t) \propto \exp(-i\Omega_0 t)$  the terms of the form  $\bar{\psi}\varphi$  and  $\psi\bar{\varphi}$  are time-independent, and their effects accumulate in time. In contrast to this, the terms proportional to  $\psi\varphi$  or  $\bar{\psi}\bar{\varphi}$  are fastly-oscillating, and their effect does not accumulate over many cycles. A generic hybridisation Hamiltonian, however, would include both resonant and off-resonant terms.

The equations above can be readily solved. However, a proper causality must be enforced: the right-going mover  $\psi_R(t, x < 0)$  should be unaffected by scattering at  $x < 0$  and thus is given by the incoming wave  $I_R(t - x/v_R)$  in the right channel. Similarly, the left mover  $\psi_L(t, x)$  is unaffected at  $x > 0$ , so it is equal to the incoming wave  $I_L(t + x/v_L)$ . For the outgoing waves, one finds

$$\psi_R(t, x > 0) = I_R\left(t - \frac{x}{v_R}\right) - \frac{i\Delta_R}{v_R}\varphi\left(t - \frac{x}{v_R}\right) , \quad (\text{I.3.3})$$

$$\psi_L(t, x < 0) = I_L\left(t + \frac{x}{v_L}\right) - \frac{i\Delta_L}{v_L}\varphi\left(t + \frac{x}{v_L}\right) . \quad (\text{I.3.4})$$

Note that these relations are in fact rather general, as they only assume linearity of the waveguide. Therefore, they hold even if the resonator is in the nonlinear regime, but the waveguide is not.

To derive the equation obeyed by the resonant mode, we have to regularise the values  $\psi_{R,L}(t, x = 0)$ , as  $\psi_{R,L}(t, x)$  are discontinuous at  $x = 0$ . Taking the average value on the two sides of the discontinuity, one may write

$$i\dot{\varphi} = (\Omega_0 - i\Gamma_0)\varphi - i\left(\frac{|\Delta_R|^2}{2v_R} + \frac{|\Delta_L|^2}{2v_L}\right)\varphi(t) + \bar{\Delta}_R I_R(t) + \bar{\Delta}_L I_L(t) . \quad (\text{I.3.5})$$

We see that the coupling to the waveguide broadens the resonance. The broadening describes the effect of radiative friction: when a wave is emitted into a channel, it exerts a back-action on the local mode so that the energy loss of the oscillator is equal to the energy carried away by the wave. Therefore, one may introduce the total linewidth as the sum of the intrinsic linewidth  $\Gamma_0$  and the radiative linewidths

$\Gamma_L$  and  $\Gamma_R$ :

$$\boxed{\Gamma_{\text{tot}} = \Gamma_0 + \Gamma_R + \Gamma_L , \quad \text{with} \quad \Gamma_i \equiv \frac{|\Delta_i|^2}{2|v_i|} ,} \quad (\text{I.3.6})$$

where  $i = R, L$ . The quantities  $\Gamma_{L,R}$  have units of inverse time. Physically, they represent the rate of emission of outgoing waves in the respective channels. In scattering theory, such parameters are known as partial widths. Physically, they give the lifetime  $(2\Gamma_i)^{-1}$  of the resonant mode if it were allowed to decay only into the respective channel<sup>3</sup>. Branching ratios  $\Gamma_L/\Gamma_{\text{tot}}$ ,  $\Gamma_R/\Gamma_{\text{tot}}$ ,  $\Gamma_0/\Gamma_{\text{tot}}$  determine the probability that the mode decays by emitting left or right magnon, or via the Gilbert damping.

After that change, we see that the resonant mode obeys the complex oscillator equation (I.1.4),

$$\boxed{i\dot{\varphi} = (\Omega_0 - i\Gamma_{\text{tot}})\varphi(t) + \Phi(t) ,} \quad (\text{I.3.7})$$

with the source  $\Phi(t)$  determined by the incoming waves  $I_R(t)$  and  $I_L(t)$ :

$$\boxed{\Phi(t) = \bar{\Delta}_R I_R(t) + \bar{\Delta}_L I_L(t) .} \quad (\text{I.3.8})$$

Acting as before, one may readily derive a second-order equation obeyed by the real part  $x(t)$  of  $\varphi(t)$ :

$$\ddot{x} + 2\Gamma_{\text{tot}}\dot{x} + (\Omega_0^2 + \Gamma_{\text{tot}}^2)x = F_I(t) , \quad (\text{I.3.9})$$

which has the form of the linear-oscillator equation Eq.(I.1.3) with the linewidth  $\Gamma_{\text{tot}}$  and the driving force due to the incoming waves as per Eq.(I.1.10):

$$F_I(t) = \text{Im} \sum_{i=R,L} \left( \frac{d}{dt} + \Gamma_{\text{tot}} - i\Omega_0 \right) \bar{\Delta}_i I_i(t) . \quad (\text{I.3.10})$$

One may notice that this structure can be easily generalised to an arbitrary number of ports connected to a resonator: the resulting source term is given by the sum over ports, and the total linewidth should include the contributions from radiative friction in all the emission channels:

$$\Gamma_{\text{tot}} = \Gamma_0 + \sum_{\text{ports}} \frac{|\Delta_{\text{port}}|^2}{2|v_{\text{port}}|} , \quad \Phi(t) = \sum_{\text{ports}} \bar{\Delta}_{\text{port}} I_{\text{port}}(t) , \quad (\text{I.3.11})$$

and, as before,

$$F(t) = \text{Im} \left[ \frac{d}{dt} - i\Omega_0 + \Gamma_{\text{tot}} \right] \Phi(t) . \quad (\text{I.3.12})$$

For reference purposes, we rewrite the transmission coefficient in the resonant-scattering model. If the incoming wave is present only in the right-going channel,  $I_R(t) = I_0 \exp(-i\omega t)$ ,  $I_L(t) = 0$ , the response of the oscillator is

$$\varphi(t) = I_0 e^{-i\omega t} \frac{\bar{\Delta}_R}{\omega - \Omega_0 + i\Gamma_{\text{tot}}} . \quad (\text{I.3.13})$$

<sup>3</sup> In the context of scattering e.g. in nuclear physics, it is customary to insert a factor of  $1/2$ . to avoid writing it in many equations.

This induces the secondary wave in the channel which is superimposed with the incident wave into the transmitted wave:

$$O_R(t) \equiv \psi_R(t, x = +0) = I_R(t) - \frac{i\Delta_R \varphi(t)}{v_R} = I_0 e^{-i\omega t} \left[ 1 - \frac{i|\Delta_R|^2}{v_R(\omega - \Omega_0 + i\Gamma_{\text{tot}})} \right]. \quad (\text{I.3.14})$$

The quantity  $|\Delta_R|^2$  can be expressed in terms of the relevant linewidth  $\Gamma_R$ , so that the transmission coefficient is

$$T(\omega) = 1 - \frac{2i\Gamma_R}{\omega - \Omega_0 + i\Gamma_{\text{tot}}} = \frac{\omega - \Omega_0 + i\Gamma_0 + i\Gamma_L - i\Gamma_R}{\omega - \Omega_0 + i\Gamma_0 + i\Gamma_L + i\Gamma_R}. \quad (\text{I.3.15})$$

Similarly, reflectivity can be found by considering the outgoing left-moving wave,

$$O_L(t, x = -0) = \frac{-i\Delta_L}{v_L} \varphi(t). \quad (\text{I.3.16})$$

Defining the scattering coefficient by the relation  $O_L(t) = I_0 R(\omega) \sqrt{v_R/v_L} \exp(-i\omega t)$ , one finds

$$R(\omega) = -\frac{i\Delta_L \bar{\Delta}_R}{\sqrt{v_R v_L} (\omega - \Omega_0 + i\Gamma_{\text{tot}})}. \quad (\text{I.3.17})$$

The absorption  $A(\omega)$  can be found as the defect in the energy conservation relation:

$$A(\omega) = 1 - |T(\omega)|^2 - |R(\omega)|^2 = \frac{4\Gamma_0 \Gamma_R}{(\omega - \Omega_0)^2 + \Gamma_{\text{tot}}^2}. \quad (\text{I.3.18})$$

Another way to compute the absorption is by noticing that for free motion the energy is proportional to  $\exp(-2\Gamma_0 t)$  and therefore its dissipation is given by  $2\Gamma_0 |\varphi|^2$ . The incoming energy flux is given by  $v_R \Omega_0 |I_R(t)|^2 = v_R \Omega_0 |I_0|^2$ . Hence one can write

$$A(\omega) = 2\Gamma_0 \frac{|\varphi(t)|^2}{v_R |I_0|^2} = \frac{4\Gamma_0 \Gamma_R}{(\omega - \Omega_0)^2 + \Gamma_{\text{tot}}^2}. \quad (\text{I.3.19})$$

The behaviour of  $|T(\omega)|$ ,  $|R(\omega)|$  and  $A(\omega)$  is illustrated in Fig. I.5.

One can see therefore that the resonance is characterised by a dip in the transmission at the resonant frequency  $\omega = \Omega_0$ , and the corresponding peaks in reflectivity and absorption. At the resonance, the transmission is given by

$$T(\omega = \Omega_0) = \frac{\Gamma_0 + \Gamma_L - \Gamma_R}{\Gamma_{\text{tot}}} = 1 - \frac{2\Gamma_R}{\Gamma_{\text{tot}}}. \quad (\text{I.3.20})$$

The phase of the transmission coefficient at resonance is equal to either  $0^\circ$  or  $180^\circ$ . More specifically, it is equal to  $0^\circ$  for non-chiral resonators ( $\Gamma_R < 1/2\Gamma_{\text{tot}}$ ), and is equal to  $180^\circ$  otherwise. One can also show that the response circumscribes a circle in the complex plane ( $\text{Re } T(\omega)$ ,  $\text{Im } T(\omega)$ ). The diameter of the circle is defined by the behaviour far away from the resonance,  $\omega = 0$  and  $\omega = \infty$ , where  $T(\omega) = 1$ , and at the resonance, and the resonant value (I.3.20), see Fig. I.6. For a non-chiral resonator,  $\Gamma_R \approx \Gamma_L$  strongly coupled to the medium ( $\Gamma_R \gg \Gamma_0$ ), one finds very strong resonant attenuation:  $T_{\text{res}} \approx 0$ . For a fully chiral resonance,  $\Gamma_R \approx \Gamma_{\text{tot}}$ , the absolute value of the transmission is constant,  $|T(\omega)| = 1$ , and the interaction with the resonator is manifested primarily in the phase shift. Note that the bare magnitude of the transmission does not allow one to tell a strongly coupled chiral resonator from a weakly coupled one ( $\Gamma_R \ll \Gamma_0$ ), for which  $T(\omega) \approx 1$ .

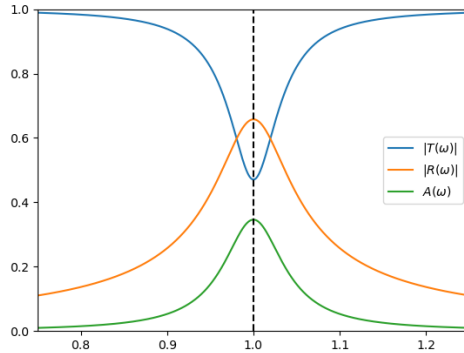


Figure I.5: Amplitude transmission coefficient  $|T(\omega)|$  (blue), reflection coefficient  $|R(\omega)|$  (orange) and energy absorption coefficient  $A(\omega)$  (green) for purely resonant scattering.

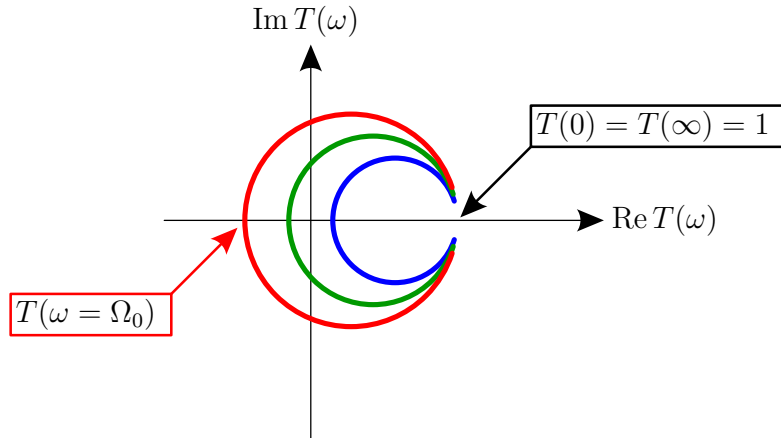


Figure I.6: The trajectory swept by the transmissivity  $T(\omega)$  in the complex plane is a circle with diameter defined by the resonant value. For  $\Gamma_R = 0$ , the circle is shrunk to a single point  $T(\omega) = 1$ . As the value of  $\Gamma_R/\Gamma_{\text{tot}}$  is increased (blue to red) the circle is expanded, reaching a unit circle in the chiral limit  $\Gamma_R = \Gamma_{\text{tot}}$ .

## I.4 Off-resonant contributions and Fano-like resonances

In general, the scattering may include an off-resonant component not associated with the local mode. In this section, we derive the relevant equations and demonstrate that the presence of short-ranged non-resonant scattering affects the dynamics of resonant scattering: the resonant frequency  $\Omega_0$  is shifted, the expressions for linewidths  $\Gamma_{R,L}$  is modified, and the form of the driving source also changes. More importantly, the shape of the resonant scattering dip in transmission and the associated peak in reflection becomes asymmetric, which is characteristic of the Fano resonance.

Simultaneous effect of resonant and non-resonant scattering can be represented

via the following system of equations:

$$i\dot{\psi}_R + iv_R \partial_x \psi_R = \mu \psi_L(0) \delta(x) + \Delta_R \varphi(t) \delta(x) , \quad (\text{I.4.1})$$

$$i\dot{\psi}_L - iv_L \partial_x \psi_L = \bar{\mu} \psi_R(0) \delta(x) + \Delta_L \varphi(t) \delta(x) , \quad (\text{I.4.2})$$

$$i\dot{\varphi} - (\Omega_0 - i\Gamma_0)\varphi = \bar{\Delta}_R \psi_R(0) + \bar{\Delta}_L \psi_L(0) . \quad (\text{I.4.3})$$

Here the parameter  $\mu$  describes non-resonant scattering between the left- and right movers that is present even if the local mode  $\varphi(t)$  is quenched. The remaining parameters are defined as in the previous section. The dynamics of the resonant mode is again reduced to the dynamics of a driven oscillator. Let us define the inputs  $I_R(t) = \psi_R(t, x = -0)$ ,  $I_L(t) = \psi_L(t, x = +0)$  and outputs  $O_R(t) = \psi_R(t, x = +0)$ ,  $O_L(t) = \psi_L(t, x = -0)$ . The above equations yield

$$iv_R [O_R(t) - I_R(t)] = \frac{\mu}{2} [I_R(t) + O_R(t)] + \Delta_R \varphi(t) , \quad (\text{I.4.4})$$

$$iv_L [O_L(t) - I_L(t)] = \frac{\bar{\mu}}{2} [I_L(t) + O_L(t)] + \Delta_L \varphi(t) , \quad (\text{I.4.5})$$

$$i\dot{\varphi} - (\Omega_0 - i\Gamma_0)\varphi = \frac{\bar{\Delta}_R}{2} [I_R(t) + O_R(t)] + \frac{\bar{\Delta}_L}{2} [I_L(t) + O_L(t)] . \quad (\text{I.4.6})$$

[Again, we regularise  $\psi_{R,L}(t, x = 0)$  as the average of  $I_{R,L}$  and  $O_{R,L}(t)$ .] Solving the first two equations for  $O_R(t)$  and  $O_L(t)$ , we write

$$O_R(t) = \frac{1}{1 + \eta} \left[ (1 - \eta) I_R - \frac{i\mu}{v_R} I_L - \frac{i}{v_R} \left( \Delta_R - \frac{i\mu \Delta_L}{2v_L} \right) \varphi \right] , \quad (\text{I.4.7})$$

$$O_L(t) = \frac{1}{1 + \eta} \left[ (1 - \eta) I_L - \frac{i\bar{\mu}}{v_L} I_R - \frac{i}{v_L} \left( \Delta_L - \frac{i\bar{\mu} \Delta_R}{2v_R} \right) \varphi \right] , \quad (\text{I.4.8})$$

where we introduced the notation

$$\eta \equiv \frac{|\mu|^2}{4v_R v_L} \quad (\text{I.4.9})$$

for convenience. The first terms here represent non-resonant transparency  $T_0$ ,  $\tilde{T}_0$  and reflectivity:

$$T_0 = \tilde{T}_0 = \frac{1 - \eta}{1 + \eta} , \quad R_0 = -\frac{i\bar{\mu}}{\sqrt{v_R v_L} (1 + \eta)} ,$$

$$\tilde{R}_0 = -\frac{i\mu}{\sqrt{v_R v_L} (1 + \eta)} . \quad (\text{I.4.10})$$

(Note that the reflectivity is defined with the extra factors  $\sqrt{v_L/v_R}$  to normalise the waves for unit energy flux.) Substituting the output modes into the equation for the resonant mode  $\varphi(t)$  brings it to the form

$$i\dot{\varphi} - (\Omega_0 - i\Gamma_0)\varphi = \frac{\bar{\Delta}_R I_R + \bar{\Delta}_L I_L}{1 + \eta} - \frac{i\mu \bar{\Delta}_R I_L}{2v_R(1 + \eta)} - \frac{i\bar{\mu} \bar{\Delta}_L I_R}{2v_L(1 + \eta)} \quad (\text{I.4.11})$$

$$+ \frac{1}{1 + \eta} \left( -i \frac{|\Delta_R|^2}{2v_R} - i \frac{|\Delta_L|^2}{2v_L} - \frac{\mu \Delta_L \bar{\Delta}_R}{4v_R v_L} - \frac{\bar{\mu} \bar{\Delta}_L \Delta_R}{4v_R v_L} \right) \varphi .$$

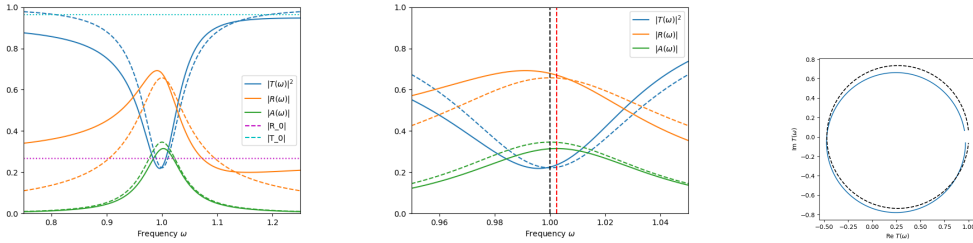


Figure I.7: The behaviour of  $T(\omega)$ ,  $R(\omega)$  and  $A(\omega)$  near a Fano resonance. Left panel:  $|T(\omega)|$ ,  $|R(\omega)|$  and  $|A(\omega)|$  are shown vs their purely resonant counterparts shown in dashed lines. Far away from the resonance,  $T(\omega)$  and  $R(\omega)$  tend to their non-resonant values shown as dotted lines. Middle panel: behaviour near the resonance. Bare frequency  $\Omega_0$  and renormalised value  $\omega_0 + \delta\Omega_0$  are shown as the vertical dashed lines (black and red). Renormalised absorption is peaked at the renormalised resonant frequency. Right panel: while in the purely resonant case the transmission coefficient circumscribes a circle centered about a point on the horizontal axis. For a Fano resonance, the circle is offset, due to the background contribution.

Note that the last two coefficients are complex-conjugate to each other, so that their sum is real. The real-valued contributions proportional to  $\varphi$  are manifested as a shift in the resonant frequency  $\delta\Omega_0$ , while the imaginary terms contribute to the radiative linewidths  $\Gamma_{R,L}$  as before. Hence the equation for  $\varphi(t)$  can be recast in the form of a driven complex oscillator,

$$i\dot{\varphi} - (\Omega_0 + \delta\Omega_0 - i\Gamma_0 - i\Gamma_R - i\Gamma_L)\varphi = \Phi(t) , \quad (\text{I.4.12})$$

with the source term

$$\Phi(t) \equiv \frac{\bar{\Delta}_R - i\frac{\bar{\mu}\bar{\Delta}_L}{2v_L}}{1 + \eta} I_R(t) + \frac{\bar{\Delta}_L - i\frac{\bar{\mu}\bar{\Delta}_R}{2v_R}}{1 + \eta} I_L(t) . \quad (\text{I.4.13})$$

The radiative linewidths  $\Gamma_{R,L}$  now include the extra corrective factor:

$$\Gamma_R \equiv \frac{|\Delta_R|^2}{2v_R(1 + \eta)} , \quad \Gamma_L \equiv \frac{|\Delta_L|^2}{2v_L(1 + \eta)} . \quad (\text{I.4.14})$$

The resonant frequency shift  $\delta\Omega_0$  is given by

$$\delta\Omega_0 = -\frac{1}{2} \operatorname{Re} \frac{\bar{\mu}\bar{\Delta}_R\Delta_L}{v_R v_L(1 + \eta)} . \quad (\text{I.4.15})$$

The similarity to the purely resonant case can be explained as follows. One may perform a rotation in the space of scattering channels to make the new channels to be eigenmodes of the scattering matrix. The new channels would couple to the oscillator in the same way as before, and will exhibit a similar radiative reaction, with somewhat different coupling constants. However, since the external sources send in the waves in original channel, the couplings to the external sources are affected.

As an application of the equations derived in this section, consider the mode driven by an input only in the right channel,  $I_R(t) = I_0 \exp(-i\omega t)$ ,  $I_L(t) = 0$ . The resonant response is then

$$\varphi(t) = I_R(t) \frac{\bar{\Delta}_R - \frac{i\bar{\mu}}{2v_L}\bar{\Delta}_L}{\omega - \Omega_0 - \delta\Omega_0 + i\Gamma_{\text{tot}}} , \quad (\text{I.4.16})$$

where  $\Gamma_{\text{tot}} = \Gamma_R + \Gamma_L + \Gamma_0$ . The absorption can be found from the expression for energy dissipation,

$$\frac{dE}{dt} = -2\Gamma_0 |\varphi(t)|^2 , \quad (\text{I.4.17})$$

and the incoming energy flux  $v_R |I_R(t)|^2$ . The respective absorption coefficient can be written as

$$A(\omega) = \frac{2\Gamma_0 \left| \bar{\Delta}_R - \frac{i\bar{\mu}}{2v_L} \bar{\Delta}_L \right|^2}{v_R(1+\eta)^2 [(\omega - \Omega_0 - \delta\Omega_0)^2 + \Gamma_{\text{tot}}^2]} \quad (\text{I.4.18})$$

Taking into account the expressions for radiative linewidths, this can be brought to the form

$$A(\omega) = \frac{4\Gamma_0 \left( \Gamma_R + \eta\Gamma_L - \frac{1}{2v_L v_R (1+\eta)} \text{Im } \mu \bar{\Delta}_R \bar{\Delta}_L \right)}{(1+\eta) [(\omega - \Omega_0 - \delta\Omega_0)^2 + \Gamma_{\text{tot}}^2]} . \quad (\text{I.4.19})$$

One can see that the absorption  $A(\omega)$  is indeed peaked at the renormalised resonant frequency,  $\omega = \Omega_0 + \delta\Omega_0$ .

To find the transmission  $T(\omega)$ , one can employ Eq.(I.4.7), which yields

$$T(\omega) = \frac{1-\eta}{1+\eta} - \frac{i}{v_R} \frac{\left( \Delta_R - \frac{i\mu}{2v_L} \Delta_L \right) \left( \bar{\Delta}_R - \frac{i\bar{\mu}}{2v_L} \bar{\Delta}_L \right)}{(1+\eta)^2 (\omega - \Omega_0 - \delta\Omega_0 + i\Gamma_{\text{tot}})} . \quad (\text{I.4.20})$$

This can be further rewritten as

$$T(\omega) = \frac{1}{(1+\eta)^2} \frac{(\omega - \Omega_0 + i\Gamma_0)(1 - \eta^2) + (1+\eta)^2(-i\Gamma_R + i\Gamma_L + \delta\Omega_0)}{\omega - \Omega_0 - \delta\Omega_0 + i\Gamma_{\text{tot}}} . \quad (\text{I.4.21})$$

Away from the resonance, this yields  $T_0$  given by Eq.(I.4.10). Unlike  $A(\omega)$ ,  $T(\omega)$  may be peaked at a different frequency because of the Fano interference between the two channels. At the renormalised resonant frequency, one finds

$$T(\Omega_0 + \delta\Omega_0) = \left[ \frac{\Gamma_{\text{tot}} - 2\Gamma_R}{\Gamma_{\text{tot}}} - \frac{\eta}{1+\eta} \frac{\Gamma_0}{\Gamma_{\text{tot}}} \right] + \frac{-i}{1+\eta} \frac{\delta\Omega_0}{\Gamma_{\text{tot}}} . \quad (\text{I.4.22})$$

The first term here represents the result for purely resonant scattering, while the rest arises from the interference between resonant and non-resonant effects. We also see that the phase of the transmission at the resonance is no longer  $0^\circ$  or  $180^\circ$ , due to the contribution  $\propto \delta\Omega_0$ .

Similarly, the reflectance can be found from Eqs.(I.4.16) and (I.4.7):

$$\sqrt{\frac{v_R}{v_L}} R(\omega) = -\frac{i\bar{\mu}}{v_L(1+\eta)} - \frac{i}{v_L(1+\eta)^2} \frac{\left( \bar{\Delta}_L - \frac{i\bar{\mu}}{2v_R} \bar{\Delta}_R \right) \left( \Delta_R - \frac{i\mu}{2v_L} \Delta_L \right)}{\omega - \Omega_0 - \delta\Omega_0 + i\Gamma_{\text{tot}}} . \quad (\text{I.4.23})$$

Again, the squares of the matrix elements here can be used to rewrite this in the form

$$\sqrt{\frac{v_R}{v_L}} R(\omega) = \frac{-i\frac{\bar{\mu}}{v_L}(1+\eta)(\omega - \Omega_0 + i\Gamma_0) - i\frac{\Delta_R \bar{\Delta}_L}{v_L}(1-\eta) + \frac{\bar{\mu}}{2v_L^2 v_R} \text{Im } \mu \Delta_R \bar{\Delta}_L}{(1+\eta)^2(\omega - \Omega_0 - \delta\Omega_0 + i\Gamma_{\text{tot}})} \quad (\text{I.4.24})$$

The resulting behaviour is illustrated in Fig. I.7

# Chapter II

## Amplification in parametrically pumped resonators

One problem that has to be overcome in the MANNGA project is gradual weakening of the signal as it propagates through the mesh of neurons. Indeed, an operation of a neuron is based upon its nonlinear transmission which features an absorption minimum. One method of overcoming this is to introduce active signal boosters into the network. One possible implementation of such a booster is a parametrically pumped Kittel resonator in which some parameters, e.g. anisotropy can be controlled externally at microwave frequencies. Such a booster would be described as a parametrically pumped linear oscillator coupled to the propagating modes. This introduces some changes in the conventional theory of parametric amplification, as it is now manifested not in the response of an oscillator, but rather in transmission and reflection coefficients. In this section, we briefly present the relevant theory.

### II.1 Parametrically excited oscillator (linear theory)

To consider a parametrically excited oscillator or resonator, one may be tempted to write its complex-valued equation of motion (I.1.4) by introducing a time-varying frequency:

$$i\dot{\varphi} = (\Omega_0 - i\Gamma_0)\varphi + \delta\Omega_0(t)\varphi(t) , \quad (\text{II.1.1})$$

where  $\delta\Omega_0(t)$  is a time-dependent contribution to the frequency. However, the dynamics described by the “naive” Eq. (II.1.1) does not involve parametric amplification or generation, as it does not increase the energy of the system. Indeed, it is easy to find the resulting free motion:

$$\varphi(t) \propto \exp \left( -\Gamma t - i\Omega_0 t - i \int \delta\Omega_0(t) dt \right) . \quad (\text{II.1.2})$$

Since  $|\varphi|^2$  is not affected by the pumping  $\delta\Omega_0(t)$ , there is no energy exchange between the pump and the oscillator, and the solution is always decaying in time.

To parametrically pump an oscillator, one has to modulate the *ellipticity* of its precession rather than the resonant frequency. To derive the correct form of the equation, one may start with the usual model of a pumped oscillator which we write in the form

$$\ddot{x} + \Omega_0^2 [1 + \epsilon(t) + \bar{\epsilon}(t)] x = 0 , \quad (\text{II.1.3})$$

where  $\epsilon(t) = \epsilon_p e^{-i\omega_p t}$  represents pumping at frequency  $\omega_p$ . The conventional treatment of parametric pumping interprets this as a shift of the resonant frequency:

$$\frac{\delta\Omega_0(t)}{\Omega_0} = \frac{1}{2} [\epsilon(t) + \bar{\epsilon}(t)] = \frac{\epsilon_p}{2} e^{-i\omega_p t} + \frac{\bar{\epsilon}_p}{2} e^{i\omega_p t} , \quad (\text{II.1.4})$$

so that the oscillation frequency is modulated between  $\Omega_0(1 \pm |\epsilon_p|)$ . The complex amplitude  $\epsilon_p$  will be called the pumping strength. We shall assume the pumping to be weak,  $\epsilon(t) \ll 1$ , so that the quadratic in  $\epsilon(t)$  terms in Eqs. (II.1.3) and (II.1.4) can be discarded. One may then derive the equation obeyed by the complex variable  $\varphi(t) = x + i\dot{x}/\Omega_0$ . It is easy to see that only the real part of  $i\dot{\varphi}$  is affected by the pumping:

$$\begin{aligned} i\dot{\varphi} - \Omega_0\varphi &= - \left( \frac{\ddot{x}}{\Omega_0} \right)_{\text{pump}} = \Omega_0 [\epsilon(t) + \bar{\epsilon}(t)] x \\ &= \Omega_0 [\epsilon(t) + \bar{\epsilon}(t)] [\varphi(t) + \bar{\varphi}(t)] . \end{aligned} \quad (\text{II.1.5})$$

Expanding the r.h.s., one obtains four different terms. We already know that the terms proportional to  $\varphi(t)$  do not describe the pumping, and can be ignored, to the lowest-order in  $|\epsilon_p|$ . To identify the relevant contribution proportional to  $\bar{\varphi}$ , we note the following. The variable  $\varphi(t)$  oscillates at frequencies close to  $\Omega_0$ , while the complex-conjugate variable  $\bar{\varphi}(t)$  oscillates at frequencies close to  $-\Omega_0$ . Multiplication by  $\epsilon(t)$  shifts the frequency by  $+\omega_p$ , while its complex-conjugate counterpart  $\bar{\epsilon}(t)$  shifts the frequency by  $-\omega_p$ . For  $\omega_p \approx 2\Omega_0$ , only the term  $\epsilon(t)\bar{\varphi}(t)$  is resonant with  $\varphi(t)$  itself, and thus results in resonant parametric pumping. Hence one may write a simplified equation for a pumped oscillator driven by an external source:

$i\dot{\varphi} - (\Omega_0 - i\Gamma)\varphi = \Omega_0\epsilon(t)\bar{\varphi}(t) + \Phi(t) ,$

$i\dot{\bar{\varphi}} + (\Omega_0 + i\Gamma)\bar{\varphi} = \Omega_0\bar{\epsilon}(t)\varphi(t) + \bar{\Phi}(t) .$

(II.1.6)

(Since the pump mixes the two modes,  $\varphi(t)$  and  $\bar{\varphi}(t)$ , it is convenient to consider the equations for both variables.)

To analyze parametric amplification in the linear regime, consider now an oscillator driven by an external signal of frequency  $\Omega$ :  $\Phi(t) = \Phi_s e^{-i\Omega t}$ . The solution can be sought in the form

$$\begin{aligned} \varphi(t) &= A_s e^{-i\Omega t} + \bar{A}_i e^{-i\omega_p t + i\Omega t} , \\ \bar{\varphi}(t) &= \bar{A}_s e^{i\Omega t} + A_i e^{i\omega_p - i\Omega t} . \end{aligned} \quad (\text{II.1.7})$$

The contribution proportional to  $A_s$  represents the response at the signal frequency  $\Omega$ . The other term ( $\propto A_i$ ) represents a parasitic product of parametric mixing at the mirror-symmetric frequency  $\Omega' = \omega_p - \Omega$ . This contribution is also known as *the idler* e.g. in the context of optical parametric amplification. We

can substitute the ansatz (II.1.7) into the equations (II.1.6), and retain only the resonant harmonics. This yields a system of two equations for the amplitudes  $A_s$  and  $A_i$  of the signal and idler components:

$$\begin{aligned} (\Omega - \Omega_0 + i\Gamma)A_s - \frac{1}{2}\epsilon_p\Omega_0 A_i &= \Phi_s , \\ (\omega_p - \Omega - \Omega_0 - i\Gamma)A_i - \frac{1}{2}\bar{\epsilon}_p\Omega_0 A_s &= 0 . \end{aligned} \quad (\text{II.1.8})$$

We can now eliminate the idler amplitude via

$$A_i = \frac{\Omega_0\bar{\epsilon}_p}{2(\omega_p - \Omega - \Omega_0 - i\Gamma)}A_s , \quad (\text{II.1.9})$$

and write the equation for  $A_s$ :

$$\left[ \Omega - \Omega_0 + i\Gamma - \frac{|\epsilon_p|^2\Omega_0^2}{4(\omega_p - \Omega - \Omega_0 - i\Gamma)} \right] A_s = \Phi_s . \quad (\text{II.1.10})$$

The relation is inverted trivially, yielding a somewhat lengthy result for  $A(\Omega, \omega_p)$  which we do not give here in full. Instead, we first consider it at the resonant pumping conditions,  $\Omega = \Omega_0$ ,  $\omega_p = 2\Omega_0$ . The relation above simplifies to

$$A_{s,\text{res}} = \frac{\Phi_s}{i\Gamma + \frac{|\epsilon_p|^2\Omega_0^2}{4i\Gamma}} . \quad (\text{II.1.11})$$

By singling out the non-pumped response  $\Phi_s/i\Gamma$ , we rewrite the relations in terms of the pumping strength  $\epsilon_p$  and the parameter  $\epsilon^*$ :

$$A_s = \frac{\Phi_s}{i\Gamma} \frac{1}{1 - \left| \frac{\epsilon_p}{\epsilon^*} \right|^2} , \quad A_i = \frac{i\bar{\epsilon}_p}{\epsilon^*} , \quad \epsilon^* \equiv \frac{2\Gamma}{\Omega_0} . \quad (\text{II.1.12})$$

We see that, owing to the pumping, the response of the oscillator is enhanced by the factor

$$G_{\text{max}} = \frac{1}{1 - \left| \frac{\epsilon_p}{\epsilon^*} \right|^2} , \quad (\text{II.1.13})$$

which can be identified with the parametric gain. The gain increases with the pumping strength  $|\epsilon_p|$  and diverges at the critical value  $\epsilon^*$ . At this point, the pump modulates the resonant frequency  $\Omega_0$  by twice the oscillator linewidth:  $\Omega_0(t)$  is pumped between  $\Omega_0 \pm 2\Gamma$ . The critical pumping strength  $|\epsilon_p| = \epsilon^*$  can be identified with the threshold for parametric instability, at which the energy supplied by the pump in one cycle exceeds the energy damped. At  $|\epsilon_p| > \epsilon^*$ , the amplifier becomes unstable and in fact becomes a parametric generator. In this regime, the output signal becomes insensitive to the input, and is instead limited by the nonlinearities.

Let us also consider the behaviour of the idler component near the parametric excitation threshold. Setting  $\Omega = \Omega_0$  and  $\omega_p = 2\Omega_0$  in Eq.(II.1.9), one finds

$$A_i \approx i \frac{\Omega_0\bar{\epsilon}_p}{2\Gamma} A_s = \frac{i\bar{\epsilon}_p}{\epsilon_*} A_s \approx i A_s e^{-i \arg \epsilon_p} . \quad (\text{II.1.14})$$

We see that the idler amplitude  $|A_i|$  of the idler is close to the amplitude  $|A_s|$  of the amplified signal. However, the phase of  $A_i$  depends upon the phase of the pumping strength  $\epsilon_p$ . In particular, if the phase of the pumping is reversed, the phase of the idler is also reversed. For clarity, let us write an approximate expression for the resulting  $\varphi(t)$ :

$$\varphi(t) = A_s e^{-i\Omega t} + \bar{A}_i e^{-i\omega_p t + i\Omega t} \approx A_s e^{-i\Omega t} - i \frac{|\epsilon_p|}{\epsilon^*} \bar{A}_s e^{i\Omega t - i\omega_p t + i \arg \epsilon_p}. \quad (\text{II.1.15})$$

We see that the phase of the idler varies oppositely to that of the signal. One may write for the total amplitude at the resonance:

$$A = A_s + \bar{A}_i = A_s \left[ 1 + \frac{|\epsilon_p|}{\epsilon^*} \exp\left(-\frac{i\pi}{2} + i \arg \epsilon_p - 2i \arg \Phi_s\right) \right]. \quad (\text{II.1.16})$$

The output is at the strongest when the phases are matched:  $\arg \Phi_s - \frac{1}{2} \arg \epsilon_p = \pi/4$ . It is periodic in the phase of the pumping with  $360^\circ$  period, and in the phase of the signal with  $180^\circ$  period. If the phase relation is reversed (by changing the phase of the pump by  $180^\circ$  or the phase of the signal by  $90^\circ$ ), the signal and the idler nearly cancel each other:  $A \sim (1 - |\epsilon_p|/\epsilon^*)$ . This is true, however, only for signal and pump tuned perfectly:  $\omega_p = 2\Omega$ . A weak detuning can be seen as smooth change of their relative phase, so that the output exhibits beating between the maximal and minimal values.

To determine the useful amplifier bandwidth, let us now consider the input slightly detuned from the resonant frequency:  $\Omega = \Omega_0 + \delta\Omega$ . We assume that  $\delta\Omega \ll \Gamma$ . Eq. (II.1.10) takes the form

$$\left[ i\Gamma \left( 1 - \frac{|\epsilon_p|^2}{\epsilon_*^2} \right) + \delta\Omega \left( 1 + \frac{|\epsilon_p|^2}{\epsilon_*^2} \right) \right] A_s(\delta\Omega) = \Phi_s. \quad (\text{II.1.17})$$

If we consider the regime of strong amplification, i.e. when  $\epsilon_p \lesssim \epsilon_*$ , we can write

$$A_s = A_{\text{res}} \frac{1}{1 - \frac{2i\delta\Omega}{\Gamma} G_{\text{max}}}. \quad (\text{II.1.18})$$

This indicates that the parametric amplification is efficient in a rather narrow passband: the gain is decreased by  $1/\sqrt{2}$  at

$$\delta\Omega_{\text{bw}} = \pm \frac{\Gamma}{2G_{\text{max}}} \approx \pm \Gamma \left( 1 - \frac{|\epsilon_p|}{\epsilon_*} \right).$$

(II.1.19)

This can be explained by noticing that amplification is due to coherent buildup occurring over  $\approx G_{\text{max}}$  pumping cycles. Detuning the input (or the pump) destroys coherence between the cycles and therefore suppresses amplification outside the shrunked bandwidth.

## II.2 A linear chiral parametric resonator

One may consider a resonant mode that is being parametrically pumped. If the pumping is below the parametric generation threshold, the system will resonantly

pick up the incoming propagating modes from the channels, amplify these parametrically, and reemit the signal into the channels. To describe this, we consider the case of perfectly chiral resonator for simplicity, so that the left-going mode can be ignored. The system is described by the equations

$$i\dot{\varphi} = (\Omega_0 - i\Gamma_0)\varphi + \epsilon\bar{\varphi} + \bar{\Delta}\psi(t, 0) , \quad i\dot{\psi} - v\partial_x\psi = \Delta\varphi(t)\delta(x) . \quad (\text{II.2.1})$$

As before, one can solve for the propagating mode,

$$\psi(t) = I(t - x/v) - \frac{i\Delta}{v}\theta(x)\varphi(t - x/v) , \quad (\text{II.2.2})$$

so that the local mode is again described by a driven parametric oscillator:

$$i\dot{\varphi} = (\Omega_0 - i\Gamma_{\text{tot}}) + \epsilon(t)\bar{\varphi}(t) + \bar{\Delta}I(t) , \quad (\text{II.2.3})$$

with  $\Phi(t) = \bar{\Delta}I(t)$  and the total resonant width  $\Gamma_{\text{tot}} = \Gamma_0 + \Gamma_R$ . Here  $\Gamma_R = |\Delta|^2/(2v)$  is the radiative contribution to the linewidth, as in Sec. I.3. When the incident wave is monochromatic at frequency  $\Omega$ ,  $I(t) = I_s \exp(-i\Omega t)$  the response of the mode includes both the signal and idler components. If the input detuning  $\Omega - \Omega_0$  falls within the shrunked bandwidth (II.1.19)  $\Gamma(1 - |\epsilon_p|/\epsilon^*)$ , the two components are again given by

$$A_s = \frac{\Delta^* I_s}{i\Gamma_{\text{tot}}} G , \quad A_i = \frac{i\bar{\epsilon}_p}{\epsilon^*} A_s . \quad (\text{II.2.4})$$

where

$$G = \frac{1}{1 - \left|\frac{\epsilon_p}{\epsilon^*}\right|^2} \quad (\text{II.2.5})$$

is the gain (II.1.13) of the amplifier at resonance. Note that the threshold  $\epsilon^*$  must be defined with the radiative linewidth included:

$$\epsilon^* = \frac{2\Gamma_{\text{tot}}}{\Omega_0} . \quad (\text{II.2.6})$$

The wave  $-i\Delta\varphi/v$  induced in the outgoing channel can be described by the two transmission coefficients  $T_s$  and  $T_i$ , for the signal and for the idler:

$$\psi(x > 0) = T_s I_0 e^{-i\Omega t} + \bar{T}_i \bar{I}_0 e^{i(\Omega - \omega_p)t} . \quad (\text{II.2.7})$$

Adding together the incident and reemitted wave, one finds

$$T_s = 1 - \frac{2\Gamma_R}{\Gamma_{\text{tot}}} G , \quad T_i = -\frac{2\Gamma_R}{\Gamma_{\text{tot}}} G \frac{i\bar{\epsilon}_p}{\epsilon^*} .$$

(II.2.8)

In the strong amplification regime,  $|\epsilon_p| \lesssim \epsilon^*$ , the amplified wave is stronger than the incoming wave, so that the latter can be neglected for simplicity. This brings the gain of the pumped resonator to the following form:

$$G_{\text{res}} \approx \frac{2\Gamma_R}{\Gamma_{\text{tot}}} G \approx \frac{\Gamma_R}{\Gamma_{\text{tot}}} \frac{1}{1 - \left|\frac{\epsilon_p}{\epsilon^*}\right|} .$$

(II.2.9)

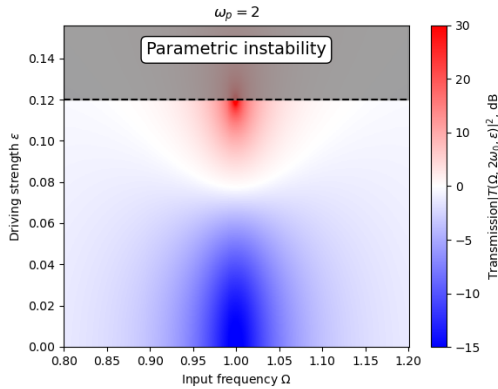


Figure II.1: Transmission coefficient for a parametrically pumped resonator as a function of the signal frequency  $\Omega$  and pump amplitude  $\epsilon_p$ . The colour scheme is chosen in such a way that blue represents attenuation, and red amplification. One can see that amplification occurs in a narrow frequency region close to the instability threshold (shaded gray).

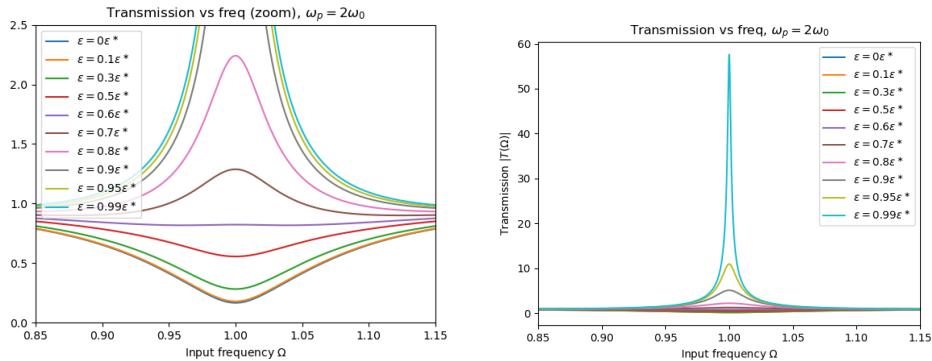


Figure II.2: Transmission through a parametrically pumped resonator. Left panel: crossover between attenuator and amplifier. Right panel: parametric amplification peak.

Such an approximate expression is convenient for quick estimates. Again,  $T_i \approx T_s$  under these conditions.

The bandwidth of such an amplifier is again given by  $\Gamma_{\text{tot}}(1 - |\epsilon_p|/\epsilon^*)$ . The resulting behaviour is illustrated in Figs. II.1 and II.2. At weak driving, the resonator exhibits a broad absorption peak. As the pumping is increased, a narrow peak emerges, which represents parametric amplification.

When the resonator is not chiral, and the wave can be scattered into both channels, the theory presented in this section requires only very minimal changes. Scattering can be still described via a parametrically pumped oscillator, but its damping must now include the contribution of both channels:  $\Gamma_{\text{tot}} = \Gamma_0 + \Gamma_R + \Gamma_L$ , which affects the critical value  $\epsilon^*$ . After that, the expression for the transmitted wave preserves its form: indeed, the backward-going channel can be considered as an extra loss when only forward-going waves are of interest. The reflected wave is again characterised by two different reflection coefficients: for the signal and for the idler:

$$O_L(t) = R_s I_0 e^{-i\Omega t} + \bar{R}_i \bar{I}_0 e^{i\omega - \omega_p t}. \quad (\text{II.2.10})$$

These are given by

$$R_s = -\frac{\Delta_L \bar{\Delta}_R}{i\sqrt{v_R v_L}} G, \quad R_i = \frac{i\bar{\epsilon}_p}{\epsilon^*} R_s. \quad (\text{II.2.11})$$

## II.3 A parametrically pumped Kittel dipole

In this section, we show how the equation for a parametric oscillator can be derived from the LLG equations for a Kittel dipole described in Sec. I.2. Let the frequencies  $\Omega_x$  and  $\Omega_z$  be time-varied by  $\delta\Omega_x(t)$  and  $\delta\Omega_z(t)$ . This could be due to modulating either the demagnetisation factors  $N_{x,z}$  geometrically, by controlling magnetic anisotropy, or by altering the bias field. One may write the extra contributions to Eqs.(I.2.1) and (I.2.2) as

$$\dot{m}_x = \dots + \delta\Omega_z(t)m_z, \quad \dot{m}_z = \dots - \delta\Omega_x(t)m_x. \quad (\text{II.3.1})$$

The variable  $\varphi(t)$  is defined by Eq. (I.2.8) with background values  $\Omega_x$  and  $\Omega_z$ . By computing  $\dot{\varphi}$ , one finds

$$i\dot{\varphi} = iC \left[ \sqrt{\Omega_x} \dot{m}_x + i\sqrt{\Omega_z} \dot{m}_z \right] = \dots + C \left[ i\sqrt{\Omega_x} \delta\Omega_z(t)m_z + \sqrt{\Omega_z} \delta\Omega_x(t)m_x \right]. \quad (\text{II.3.2})$$

(Here  $C$  is the normalisation coefficient which is not important for what follows.) Expressing  $m_x$  and  $m_z$  via  $\varphi$  and  $\bar{\varphi}$  as per Eq. I.2.8,

$$m_x = \frac{1}{2C\sqrt{\Omega_x}} (\varphi + \bar{\varphi}), \quad m_z = \frac{1}{2iC\sqrt{\Omega_x}} (\varphi - \bar{\varphi}), \quad (\text{II.3.3})$$

one can bring the parametric contribution to the form

$$i\dot{\varphi} = \dots + \frac{\sqrt{\Omega_x \Omega_z}}{2} \left\{ \varphi \left[ \frac{\delta\Omega_z(t)}{\Omega_z} + \frac{\delta\Omega_x(t)}{\Omega_x} \right] + \bar{\varphi} \left[ \frac{\delta\Omega_x(t)}{\Omega_x} - \frac{\delta\Omega_z(t)}{\Omega_z} \right] \right\}. \quad (\text{II.3.4})$$

Since the resonant frequency is given by  $\Omega_0 = \sqrt{\Omega_x \Omega_z}$ , the first term here can be associated with the change in frequency:

$$\delta\Omega_0(t) = \frac{\Omega_0}{2} \left[ \frac{\delta\Omega_x(t)}{\Omega_x} + \frac{\delta\Omega_z(t)}{\Omega_z} \right]. \quad (\text{II.3.5})$$

However, this term is proportional to  $\varphi(t)$  itself and does not result in resonant pumping, as was discussed in Sec II.1). As to the more important second term [ $\propto \bar{\varphi}$ ], one may notice that the modulations  $\delta\Omega_x(t)$  and  $\delta\Omega_z(t)$  enter with opposite signs. Hence, the  $\bar{\varphi}$  term cannot be interpreted in terms of the change in frequency. Instead, one may relate it to the change in ellipticity  $e_{xz} = \sqrt{\Omega_x/\Omega_z}$ . Indeed,

$$\delta e_{xz}(t) = \frac{1}{2} \left[ \frac{\delta\Omega_x(t)}{\sqrt{\Omega_x \Omega_z}} - \delta\Omega_z(t) \sqrt{\frac{\Omega_x}{\Omega_z^3}} \right] = e_{xz} \left[ \frac{\delta\Omega_x(t)}{\Omega_x} - \frac{\delta\Omega_z(t)}{\Omega_z} \right]. \quad (\text{II.3.6})$$

Thus, we obtain the equation for a pumped Kittel mode

$$i\dot{\varphi} = (\Omega_0 - i\Gamma_0)\varphi + \delta\Omega_0(t)\varphi + \Omega_0\epsilon(t)\bar{\varphi}(t), \quad (\text{II.3.7})$$

with the pumping term

$$\boxed{\epsilon(t) \equiv \frac{1}{2} \left[ \frac{\delta\Omega_x(t)}{\Omega_x} - \frac{\delta\Omega_z(t)}{\Omega_z} \right] = \frac{\delta e_{xz}(t)}{e_{xz}}.} \quad (\text{II.3.8})$$

In simple cases, when only one of the two frequencies are modulated, the pumping can be related to the change in frequency. One may write

$$\epsilon(t) = \frac{\delta\Omega_0(t)}{\Omega_0}, \quad (\text{II.3.9})$$

if  $\delta\Omega_z(t) = 0$  so that only  $\Omega_x$  is modulated. Similarly,

$$\epsilon(t) = -\frac{\delta\Omega_0(t)}{\Omega_0}, \quad (\text{II.3.10})$$

when only  $\Omega_z$  is modulated,  $\delta\Omega_x(t) = 0$ . In general, however, there is no direct relation between the pumping strength and modulation of the resonant frequency. When both frequencies are modulated by the same fractional amount, in phase, i.e. when  $\delta\Omega_x(t)/\Omega_x = \delta\Omega_z(t)/\Omega_z$ , the carrier frequency is modulated without resonant pumping:  $\epsilon(t) = 0$ . When their relative phase is reversed,  $\delta\Omega_x(t)/\Omega_x = -\delta\Omega_z(t)/\Omega_z$ , the pumping is not accompanied by a change in resonant frequency:  $\delta\Omega_0(t) = 0$ ,  $\epsilon(t) \neq 0$ . Thus, one should treat the amplitudes of  $\delta\Omega_0(t)$  and  $\epsilon(t)$  as independent quantities.

# Chapter III

## Nonlinear scattering by chiral resonators

We now discuss scattering of a propagating mode by a weakly nonlinear resonator. In the MANNGA project, we expect that the nonlinear effects will be mostly manifested in the dynamics of resonant modes that concentrate the energy. We also expect the signal processing to occur near the respective resonant frequency, ignoring third harmonics and rectification. We shall discuss nonlinearities that may occur in the dynamics of a generic linear oscillator. We then derive the respective frequency shift for a quasi-uniform Kittel mode. To study the manifestations of the nonlinearity, we consider a nonlinear resonator coupled to a one-dimensional medium. We show that the well-known foldover effect can be observed in the transmissivity of such a setup as a bistability and hysteresis.

### III.1 Cubic nonlinearities and frequency shifts

To describe nonlinear local LLG modes, one may introduce a nonlinear oscillator model. However, non-linear terms can be introduced into the dynamics of a local oscillator in several ways. For simplicity, we restrict the analysis only to energy-conserving nonlinearities in what follows. Consider a non-damped simple harmonic oscillator. In general, one may extend its linear equation of motion  $\ddot{x} + \Omega_0^2 x = 0$  with two energy-conserving cubic terms:

$$\ddot{x} + \Omega_0^2 x + \lambda x^3 + \tilde{\lambda} \dot{x}^2 = 0 . \quad (\text{III.1.1})$$

Here the parameters  $\lambda$  and  $\tilde{\lambda}$  characterise the strength of the nonlinear effects and thus introduce the characteristic scale for the variable  $x(t)$  of the oscillator. Similarly, one may also consider an oscillator with two quadratic nonlinearities:

$$\ddot{x} + \Omega_0^2 x + \alpha x^2 + \tilde{\alpha} \dot{x}^2 = 0 . \quad (\text{III.1.2})$$

It turns out that nonlinearities of different functional form manifest themselves very similarly if the oscillator is probed near its fundamental harmonic: the response exhibits the resonance at a frequency that depends upon the driving amplitude. E.g. the two cubic terms stated above result in the shift of the resonant frequency

$$\delta\Omega_0 = \frac{3\lambda + \Omega_0^2 \tilde{\lambda}}{8\Omega_0} |A|^2 , \quad (\text{III.1.3})$$

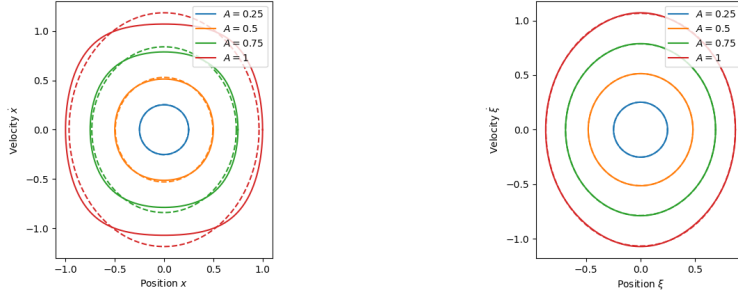


Figure III.1: Left panel: phase-space trajectory of a nonlinear oscillator ( $\Omega_0 = 1$ ,  $\lambda = 1$ ,  $\tilde{\lambda} = -1/2$  in arbitrary units) deviates from a perfect circle; the larger is the amplitude  $A$ , the more noticeable is the deviation. The fundamental harmonic (dashed lines) circumscribes an ellipse. Right: the transformation  $x = \xi \exp(\beta \xi^2)$  with  $\beta = 3/16$  suppresses the third harmonic and thus brings the phase-space trajectories closer to perfect ellipses even for  $A \sim 1$ .

for an oscillation of amplitude  $A$ . Hence the response at the fundamental frequency is only sensitive to a certain combination of the two coefficients  $\lambda$  and  $\tilde{\lambda}$ , and thus one cannot distinguish between the two nonlinearities from the measured response. This can be understood by considering a nonlinear change of the oscillator variable:

$$x(t) = \xi(t) \exp[\beta \xi^2(t)] . \quad (\text{III.1.4})$$

where  $\beta$  is an arbitrary parameter characterising the transformation, and  $\xi(t)$  is the new variable. One readily finds

$$\dot{x} = \dot{\xi}(1 + 2\beta\xi^2)e^{\beta\xi^2} , \quad \ddot{x} = [\ddot{\xi}(1 + 2\beta\xi^2) + 6\beta\xi^2\dot{\xi}]e^{\beta\xi^2} . \quad (\text{III.1.5})$$

Substituting this into the equation for the oscillator and approximating the factor  $(1 + 2\beta\xi^2)^{-1} \approx 1 - 2\beta\xi^2$  to the lowest order in  $\beta$ , one arrives at the equation of the same form as Eq.(III.1.1),

$$\ddot{\xi} + \Omega_0^2\xi + \lambda_\xi\xi^3 + \tilde{\lambda}_\xi\dot{\xi}^2\xi + O(\xi^5) = 0 , \quad (\text{III.1.6})$$

with new nonlinear parameters:

$$\lambda_\xi = \lambda - 2\beta\Omega_0^2 , \quad \tilde{\lambda}_\xi = \tilde{\lambda} + 6\beta . \quad (\text{III.1.7})$$

Note that the transformation  $x \rightarrow \xi$  leaves the non-linear frequency shift (III.1.3) unchanged: the frequency is independent of the choice of the variables.

This observation can be explained as follows. A free linear oscillator without damping moves along a contour of constant energy  $\frac{1}{2}[\dot{x}^2 + \Omega_0^2x^2]$  sweeping an ellipse in the phase plane  $(x, \dot{x})$ , with area proportional to the energy. For the nonlinear system, the conserved energy has a different form:

$$H(x, \dot{x}) = e^{\tilde{\lambda}x^2} \left[ \frac{\dot{x}^2}{2} + \frac{\Omega_0^2}{2\tilde{\lambda}} + \frac{\lambda}{2\tilde{\lambda}^2} (\tilde{\lambda}x^2 - 1) \right] , \quad (\text{III.1.8})$$

and contours of constant energy are deformed loops such as those shown as solid lines in the left panel of Fig. III.1. The corresponding time dependence of  $x(t)$  and  $\dot{x}(t)$  on these contours is no longer monochromatic. The larger the amplitude,

the more noticeable is the difference between the respective contour and the circle. Yet the energy-conserving dynamics is still time-periodic, and its Fourier spectrum is a set of discrete peaks which can be easily separated. When all harmonics except the fundamental are filtered out, one is still left with a simple harmonic motion,  $x = A \sin(\Omega t + \theta_0)$ ,  $\dot{x} = \Omega A \cos(\Omega t + \theta_0)$ . The filtered trajectory would also sweeps an ellipse in the phase plane, with perhaps a different aspect ratio set by the new frequency  $\Omega$ . This is shown as dashed lines in the left panel of Fig. III.1. The nonlinear change of variables discussed above deforms phase space contours without changing the circle that is swept by the fundamental harmonic. Moreover, by choosing an appropriate value of  $\beta$ , one may transform the constant energy contour to minimise its deviations from a perfect circle as shown in the right panel of Fig. III.1. This can be seen if one looks into the expression for the third-harmonic generated due to the nonlinearity:

$$x(t) = A \cos \Omega t + \frac{\lambda - \tilde{\lambda} \Omega_0^2}{8\Omega_0^2} A^3 \cos 3\Omega t . \quad (\text{III.1.9})$$

If one chooses  $\beta$  to make  $\lambda_\xi = \Omega_0^2 \tilde{\lambda}_\xi$ , the third harmonic in  $\xi$  is not generated, which means the precession is close to a perfect circle, as can be seen in the right panel of Fig. III.1. We also note that such a transformation affects damping and coupling to propagating media only in the higher orders. Therefore, such effects could be neglected if one considers free motion of the oscillators as the strongest effect in dynamics, and everything else (damping, nonlinearity, pumping, coupling to external sources) as weaker contributions to the dynamics.

A quadratic nonlinearity can be considered similarly. The most prominent manifestations of this nonlinearity that occur in the lowest order are the rectification and second-harmonic generation, which are not seen near the fundamental frequency. In the second order, these harmonics are intermixed with the fundamental, and again result in frequency shift:

$$\delta\Omega = -\frac{1}{12} \frac{5\alpha^2 + 5\alpha\tilde{\alpha}\Omega_0^2 + 2\tilde{\alpha}^2\Omega_0^4}{\Omega_0^3} |A|^2 . \quad (\text{III.1.10})$$

Thus, even though the nonlinearity has a different form, its effect on the fundamental harmonic is rather similar: the frequency is shifted, by an amount quadratic in amplitude. Interestingly, a quadratic nonlinearity always yields a shift that is negative.

Thus, we see that the choice of the form of the nonlinear term may be the matter of convenience: one may completely eliminate either the term with  $\lambda$ , or the one with  $\tilde{\lambda}$ . To distinguish between different nonlinear contributions, one has to analyse other effects, such as third-harmonic generation, or rectification. For our purpose, it is in fact convenient to set  $\tilde{\lambda}\Omega_0^2 = \lambda$ , as this suppresses the third harmonic and thus simplifies the equation for the mode  $\varphi$ . Indeed, let us rewrite the equation for  $\dot{\varphi}$  as before. The nonlinear contribution becomes

$$i\dot{\varphi} = \dots + \frac{\lambda}{\Omega_0} \left( \frac{\varphi + \bar{\varphi}}{2} \right)^3 + \frac{\tilde{\lambda}}{\Omega_0} \Omega_0^2 \left( \frac{\varphi - \bar{\varphi}}{2i} \right)^2 \left( \frac{\varphi + \bar{\varphi}}{2} \right) . \quad (\text{III.1.11})$$

Expanding this expression yields a number of terms. However, most of them are non-resonant: those proportional to  $\varphi^3$ ,  $\bar{\varphi}^3$ , or  $\bar{\varphi}^2\varphi$ . The only resonant contributions that are present on the r.h.s. are those proportional to  $|\varphi|^2\varphi = \varphi^2\bar{\varphi}$ .

Collecting such terms, one finds

$$i\dot{\varphi} = (\Omega_0 - i\Gamma_0)\varphi + \left[ \frac{3\lambda}{8\Omega_0} + \frac{\tilde{\lambda}\Omega_0}{8} \right] |\varphi|^2 \varphi + [\text{non-resonant}] . \quad (\text{III.1.12})$$

Thus, if only the resonant terms are retained, the mode  $\varphi$  obeys an equation with a nonlinear contribution  $|\varphi|^2\varphi$ , identical to the one in the nonlinear Schrödinger equation. (The respective equation is also known as the Gross-Pitaevsky equation.) This term can be identified with the nonlinear shift of the resonant frequency. The constant of nonlinearity has the form

$$\lambda_\varphi = \frac{3\lambda + \Omega_0^2 \tilde{\lambda}}{8\Omega_0} . \quad (\text{III.1.13})$$

It is obvious that the nonlinear equation with non-resonant terms dropped admits a time-periodic solution  $\varphi(t) = \varphi_0 \exp(-i\Omega t)$ , with shifted frequency

$$\Omega = \Omega_0 + \lambda_\varphi |\varphi_0|^2 . \quad (\text{III.1.14})$$

The frequency shift can be positive or negative, depending upon the sign of  $\lambda_\varphi$ .

## III.2 Nonlinear Kittel modes

One may also derive the actual nonlinearity for a uniform Kittel mode. In this case, the only source of the nonlinearity is the reduction in the magnetisation component  $M_y$ , see Eq. (I.2.7.) This yields the LLG equations in the form

$$\dot{m}_x = \omega_z m_z - \Lambda_z(m_x^2 + m_z^2)m_z , \quad \dot{m}_z = -\omega_x m_x + \Lambda_x(m_x^2 + m_z^2)m_x , \quad (\text{III.2.1})$$

with

$$\Lambda_{x,z} \equiv \frac{\gamma_s \mu_0}{2M_s} N_{x,z} . \quad (\text{III.2.2})$$

Since for Kittel precession  $m_z \propto \dot{m}_x$ , we see that both terms  $m_x^3$  and  $\dot{m}_x^2 m_x$  will be present in the equation for  $m_x$ ; the same is of course true of  $m_z$ . To derive the nonlinearity, one may write the equation for the variable  $\varphi$  with the help of Eq.(I.2.8):

$$i\dot{\varphi} = \dots - \frac{1}{2} \left[ \Lambda_z \sqrt{\frac{\Omega_x}{\Omega_z}} (\varphi - \bar{\varphi}) + \Lambda_x \sqrt{\frac{\Omega_z}{\Omega_x}} (\varphi + \bar{\varphi}) \right] (m_x^2 + m_z^2) , \quad (\text{III.2.3})$$

with

$$\begin{aligned} m_x^2 + m_z^2 &= \frac{(\varphi + \bar{\varphi})^2}{4C^2\Omega_x} - \frac{(\varphi - \bar{\varphi})^2}{4C^2\Omega_z} \\ &= \frac{\varphi^2 + \bar{\varphi}^2}{4C^2} \left( \frac{1}{\Omega_x} - \frac{1}{\Omega_z} \right) + \frac{|\varphi|^2}{2C^2} \left( \frac{1}{\Omega_x} + \frac{1}{\Omega_z} \right) . \end{aligned} \quad (\text{III.2.4})$$

The right-hand side contains several terms, but we are only interested in the resonant contributions  $\propto |\varphi|^2\varphi = \bar{\varphi}\varphi^2$ . To this end, we first rewrite the equation in the form

$$i\dot{\varphi} = \dots - \frac{1}{2\Omega_0} [(\Omega_x \Lambda_z + \Omega_z \Lambda_x)\varphi + (\Lambda_x \Omega_z - \Lambda_z \Omega_x)\bar{\varphi}] (m_x^2 + m_z^2) , \quad (\text{III.2.5})$$

and then multiply it by  $m_x^2 + m_z^2$  given above. Collecting the relevant terms, one finds

$$i\dot{\varphi} = \dots - \frac{3\Lambda_x\Omega_z^2 + 3\Lambda_z\Omega_x^2 + \Omega_x\Omega_z(\Lambda_x + \Lambda_z)}{8C^2\Omega_0^3} |\varphi|^2 \varphi + [\propto \varphi^3] + [\propto \bar{\varphi}^3] + [\propto \bar{\varphi}^2\varphi]. \quad (\text{III.2.6})$$

This, we find the nonlinearity parameter

$$\lambda_\varphi = -\frac{\mu_0\gamma_s^2}{8V\Omega_0^2} [3N_z\Omega_x^2 + 3N_x\Omega_z^2 + \Omega_x\Omega_z(N_x + N_z)]. \quad (\text{III.2.7})$$

The resulting shift  $\lambda_\varphi|\varphi|^2$  of the fundamental frequency is negative. Indeed, the nonlinearity results from shortening of  $M_y$  due to precession, which can be simulated by reduction in saturation magnetisation  $M_s$ . In the linear theory such shortening would lower the resonant frequency.

The nonlinear frequency shift  $\lambda_\varphi|\varphi|^2$  can be also expressed in terms of amplitudes  $A_x$  of the magnetisation component  $m_x$ :

$$\delta\Omega_0 = \lambda_\varphi|\varphi|^2 = -\frac{\mu_0\gamma_s^2\Omega_x A_x^2}{16M_s\Omega_0^3} [3N_z\Omega_x^2 + 3N_x\Omega_z^2 + \Omega_x\Omega_z(N_x + N_z)], \quad (\text{III.2.8})$$

which may be more convenient for practical purposes. Alternatively, one may express the same shift in terms of the other component, this amounts to replacing  $\Omega_x A_x^2$  with  $\Omega_z A_z^2$ .

One can also derive an equation for  $m_x$  or  $m_z$ , eliminating one of the two magnetisation components, retaining only the lowest terms and replacing  $m_z$  with  $-\dot{m}_x/\Omega_z$ . We give the relevant equation without an explicit derivation:

$$\ddot{m}_x + 2\Gamma\dot{m}_x + \Omega_0^2 m_x + \lambda_x m_x^3 + \tilde{\lambda}_x \dot{m}_x^2 m_x = 0, \quad (\text{III.2.9})$$

with

$$\lambda_x = -\Lambda_x\Omega_z - \Lambda_z\Omega_x, \quad \tilde{\lambda}_x = \frac{2\Lambda_z\Omega_z - 3\Lambda_z\Omega_x - \Lambda_x\Omega_z}{\Omega_z^2}. \quad (\text{III.2.10})$$

The other component  $m_z$  obeys a similar equation, in which the  $x$  and  $z$  indices in the expressions for the nonlinear coefficients are interchanged.

### III.3 Nonlinearities in resonant scattering

We can now consider transmission through a nonlinear resonator. This is specified by the following model:

$$i\dot{\varphi} = (\Omega_0 - i\Gamma_0)\varphi - \lambda|\varphi|^2\varphi + \Delta^*\psi(t, 0), \\ i\dot{\psi} - i\partial_x\psi = \Delta\varphi(t)\delta(x). \quad (\text{III.3.1})$$

Here we included a nonlinear frequency shift  $-\lambda|\varphi|^2$  into the dynamics of the resonator. We have chosen negative sign of the frequency shift, as this is what one normally expects for magnonic modes. The propagating channel  $\psi(t, x)$  is assumed to be linear. For simplicity, we again consider only one channel, as we

focus on the transmission near the fundamental frequency. One can eliminate the variable  $\psi(t, x)$  as before, reducing the problem to that of a driven nonlinear oscillator:

$$i\dot{\varphi} = (\Omega_0 - i\Gamma_{\text{tot}})\varphi - \lambda|\varphi|^2\varphi + \bar{\Delta}I(t) , \quad (\text{III.3.2})$$

where  $I(t)$  is the incoming wave, and  $\Gamma_{\text{tot}}$  includes the radiative damping. The outgoing wave is then found as before:

$$O(t) = I(t) - \frac{i\Delta}{v}\varphi(t) . \quad (\text{III.3.3})$$

The key feature in the response of a driven non-linear oscillator is the foldover effect and the resulting hysteretic behaviour. Indeed, when a nonlinear oscillator is excited away from resonance, it may tune itself into resonance by shifting the nonlinear resonant frequency towards the driving frequency. Obviously, this can only occur if the input is detuned above the nominal resonant frequency: if the frequency shift is negative, one should drive the system below the resonance. When the driving is increased in strength while slowly chirping downwards, the resonant response will remain strong.

To describe this within our framework, consider a monochromatic input of frequency  $\omega$ ,  $I(t) = I_0 \exp(-i\omega t)$ . Seeking a solution in the same form,  $\varphi(t) = \varphi_0 \exp(-i\omega t)$ , we write

$$\boxed{[\omega - \Omega_0 + i\Gamma_{\text{tot}} + \lambda|\varphi_0|^2]\varphi_0 = \bar{\Delta}I_0} . \quad (\text{III.3.4})$$

We see that the amplitude of the oscillations is given by a non-linear equation in complex variables. An equation for  $|\varphi_0|$  is readily obtained by squaring this relation:

$$\boxed{[(\omega - \Omega_0 + \lambda|\varphi_0|^2)^2 + \Gamma_{\text{tot}}^2]|\varphi_0|^2 = |\Delta|^2|I_0|^2} . \quad (\text{III.3.5})$$

The left-hand side is a cubic polynomial  $P(x)$  in  $|\varphi_0|^2$ , and its behaviour depends upon the detuning from the fundamental frequency. For example, for positive detunings the polynomial is always monotonic, and thus the equation has a unique solution. For sufficiently strong negative detunings, however, it becomes non-monotonic, and the respective equation in  $|\varphi_0|^2$  has three roots. The foldover threshold can be identified by seeking for conditions at which  $P'(x_*) = P''(x_*) = 0$ . This yields

$$\boxed{\omega^* = \Omega_0 - \Gamma_{\text{tot}}\sqrt{3} , \quad |\Delta I_0^*| = \sqrt{\frac{8\Gamma_{\text{tot}}}{3\sqrt{3}\lambda}} , \quad |\varphi_0^*| = \frac{2\Gamma_{\text{tot}}}{\sqrt{3}\lambda}} . \quad (\text{III.3.6})$$

Thus, the solution to (III.3.5) ceases to be unique for  $\omega < \omega^*$ . Out of the three resulting branches, one is unstable, and the other two remain stable.

Thus, the transmission problem can be solved as follows. For the given incident amplitude  $I_0$ , one has to obtain the amplitude of nonlinear oscillations  $|\varphi_0|$  by solving Eq. (III.3.5), and thus obtain the frequency shift  $-\lambda|\varphi_0|^2$ . The transmission coefficient is then given by the same formula as before, with shifted resonant frequency:

$$T(\omega, |I_0|) = 1 - \frac{2\Gamma_R}{\omega - \Omega_0 + \lambda|\varphi_0|^2 + i\Gamma_{\text{tot}}} . \quad (\text{III.3.7})$$

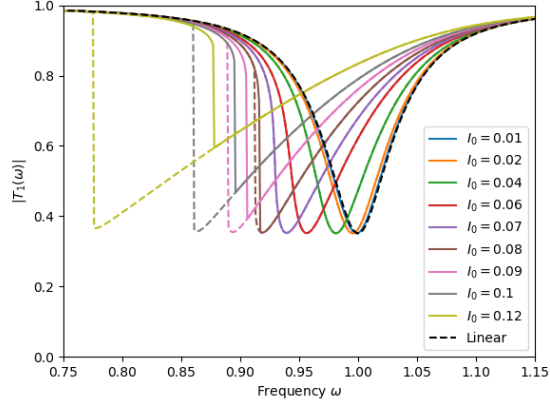


Figure III.2: Transmission through a nonlinear resonator attached to a waveguide as a function of frequency. As the driving signal increases in the amplitude, the curve becomes more symmetric, and eventually a hysteretic behaviour develops. Solid lines correspond to the excitation frequency swept upwards, dashed lines represent downward-going sweep.

As the amplitude is increased, the resonant dip in transmission becomes asymmetric in frequency, with its lower-frequency slope becoming much steeper. Eventually the foldover point is reached,  $|I_0| = |I_0|^*$ , when the lower-frequency slope is vertical. After that, transmission below  $\omega_*$  becomes hysteretic: by chirping to these frequencies from the above and from the below, one may end up on either of the two stable branches. This is shown in Fig. III.2.

# Chapter IV

## Multidimensional linear scattering: general framework

Within the MANNGA project, we are interested in resonant scattering of spin waves by local resonant modes embedded into two-dimensional medium (a film). In this section, we describe the key concepts that are necessary for this, without paying attention to the specifics of magnonic systems. (Applications to magnonics will be discussed in the following sections.) We state the resonant-level model in the multidimensional case that extends the one-dimensional model of Sec. I.3. Then, we introduce various characteristics of the dispersion of the medium and give an expression for the scattered wave emitted by a known source. We then show how one can eliminate the effect of scattering from the dynamics of the local oscillator by introducing its self-energy due to hybridisation with the bulk modes. We then express the solution of the scattering problem in terms of the self-energy and hybridisation strength.

### IV.1 The model

To describe resonant scattering in more than one dimension, we introduce propagating modes  $\psi_{\mathbf{k}}$  obeying the dispersion  $\omega_{\mathbf{k}}$  and decaying at the rate  $\gamma_{\mathbf{k}}$ , which we shall mostly treat as a negligible quantity. Here  $\mathbf{k}$  is the wavevector enumerating the modes in the medium. The modes  $\psi_{\mathbf{k}}$  couple to a localised mode  $\varphi$ , which is described by the hybridisation coefficients  $\Delta_{\mathbf{k}}$ . (This resembles the  $s - d$  model from the theory of magnetic impurities.) The relevant expression for the energy takes the form

$$H[\psi_{\mathbf{k}}, \varphi] = \sum_{\mathbf{k}} \omega_{\mathbf{k}} |\psi_{\mathbf{k}}|^2 + \Omega_0 |\varphi|^2 + \sum_{\mathbf{k}} \Delta_{\mathbf{k}} \varphi \bar{\psi}_{\mathbf{k}} + \text{c.c.} \quad (\text{IV.1.1})$$

Here and in what follows the sums over  $\mathbf{k}$  are understood as sums over all the modes. We shall implicitly assume unit normalisation volume (length, area):

$$\sum_{\mathbf{k}} (\dots) = \int_{-\infty}^{\infty} \frac{d^D \mathbf{k}}{2\pi} (\dots) . \quad (\text{IV.1.2})$$

In one dimension, this is reduced to summation over left- and right modes and integrating over the magnitude  $|k|$ :

$$\sum_{\mathbf{k}} (\dots) = \sum_{R,L} \int_0^{\infty} \frac{d|k|}{2\pi} (\dots) . \quad (\text{IV.1.3})$$

In two dimensions, one may write the sum over modes by introducing polar coordinates  $(k, \theta)$ :

$$\sum_{\mathbf{k}} (\dots) = \int \frac{d^2\mathbf{k}}{(2\pi)^2} (\dots) = \int_0^{\infty} \frac{k dk}{2\pi} \oint \frac{d\theta}{2\pi} (\dots) . \quad (\text{IV.1.4})$$

The modes  $\psi_{\mathbf{k}}$  obey the Poisson brackets similar to those for local modes  $\varphi$ :

$$\left\{ \psi_{\mathbf{k}}, \bar{\psi}_{\mathbf{k}'} \right\} = i\delta_{\mathbf{k},\mathbf{k}'} , \quad (\text{IV.1.5})$$

where  $\delta_{\mathbf{k},\mathbf{k}'}$  is a delta function in the  $\mathbf{k}$ -space. Again, we assume that the number of quanta in the localised mode is  $|\varphi|^2$ , and the number of quanta in a given propagating mode is  $\propto |\psi_{\mathbf{k}}|^2$ .

The equations that follow from the Hamiltonian above are of the form

$$i\dot{\psi}_{\mathbf{k}} = (\omega_{\mathbf{k}} - i\gamma_{\mathbf{k}})\psi_{\mathbf{k}} + \Delta_{\mathbf{k}}\varphi + S_{\mathbf{k}} , \quad (\text{IV.1.6})$$

$$i\dot{\varphi} = (\Omega_0 - i\Gamma_0)\varphi + \sum_{\mathbf{k}} \bar{\Delta}_{\mathbf{k}}\psi_{\mathbf{k}} . \quad (\text{IV.1.7})$$

Here we also introduced a far-away source  $S_{\mathbf{k}}$  that describes emission of the incident waves.

We note in passing that the Hamiltonian considered here is not the most generic one. In general, a coupling between a propagating wave and a Kittel mode may also include non-resonant terms:

$$H = [\dots] + \sum_{\mathbf{k}} \Delta'_{\mathbf{k}}\psi_{\mathbf{k}}\varphi + \text{c.c.} \quad (\text{IV.1.8})$$

Time dependence in such terms is  $\exp(-i\Omega_0 t - i\omega_{\mathbf{k}} t)$ . For  $\Omega_0 > 0$  and  $\omega_{\mathbf{k}} > 0$ , the effect of these terms does not accumulate with time, and their effect upon dynamics is less significant. Nevertheless, they may become important for strongly-coupled overlapping resonances, see Sec. VI.4.

## IV.2 Free propagation and Green's function

Before solving the model, we discuss propagation of the waves  $\psi_{\mathbf{k}}(t)$  in the medium. It can be understood in terms of Green's function  $G_{\mathbf{k}}(\omega)$ , which takes a simple form in free space:

$$G_{\mathbf{k}}(\omega) = \frac{1}{\omega - \omega_{\mathbf{k}} + i\gamma_{\mathbf{k}}} .$$

(IV.2.1)

A wave produced by a source  $S_{\mathbf{k}}$  takes the form

$$\psi_{\mathbf{k}} = G_{\mathbf{k}}(\omega)S_{\mathbf{k}} . \quad (\text{IV.2.2})$$

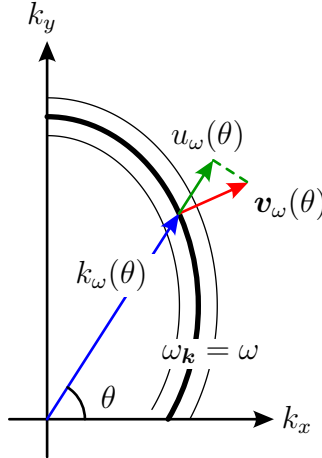


Figure IV.1: Wavenumber  $k_\omega(\theta)$ , the group velocity  $\mathbf{v}_\omega(\theta)$  and its radial component  $u_\omega(\theta)$ .

Let us obtain an expression for  $G(\omega, \mathbf{r})$  in the real space. To this end, we introduce some quantities describing the propagation. Green's function is peaked at the medium dispersion  $\omega = \omega_{\mathbf{k}}$ . For a given frequency, this specifies a surface (or perhaps a set of disconnected surfaces) in the  $\mathbf{k}$ -space. We are mostly interested in the case of two dimensions. The constant-frequency contour can be characterised in polar coordinates  $(k, \theta)$  as  $\mathbf{k} = k_\omega(\theta)(\cos \theta, \sin \theta)$ , where  $k_\omega(\theta)$  is the wavenumber for the wave with frequency  $\omega$  and a given orientation of the wave vector, see Fig. IV.1. For a generic dispersion, the wave does not necessarily propagate along the radial direction  $\hat{\mathbf{k}}$ . Instead, its group velocity can be written in the form

$$\boxed{\mathbf{v}_\omega(\theta) = u_\omega(\theta) \left[ \hat{\mathbf{k}} - \frac{k'_\omega}{k_\omega} \hat{\boldsymbol{\theta}} \right], \quad u_\omega(\theta) \equiv \frac{\partial \omega_{\mathbf{k}}}{\partial |\mathbf{k}|}.} \quad (\text{IV.2.3})$$

where  $\hat{\boldsymbol{\theta}}$  is the angular direction, and  $k'_\omega(\theta) \equiv dk_\omega/d\theta$ . In what follows, however, it will be convenient to express some quantities in terms of the “naive” group velocity  $u_\omega(\theta)$ . One may notice that  $u_\omega(\theta)$  is the radial projection of  $\mathbf{v}_\omega(\theta)$ :

$$u_\omega(\theta) = \mathbf{v}_\omega(\theta) \cdot \hat{\mathbf{k}}, \quad (\text{IV.2.4})$$

which implies  $|u_\omega(\theta)| < |\mathbf{v}_\omega(\theta)|$ .

Transforming the waves from the  $\mathbf{k}$ -space to the real space involves integrating over the former, which can be achieved by several methods. An obvious choice is to employ the polar coordinates:

$$\int [\dots] d^2\mathbf{k} = \int_0^\infty \oint \int [\dots] k dk d\theta \quad (\text{IV.2.5})$$

Alternatively, one may cover the  $\mathbf{k}$ -space with constant frequency contours, and integrate along and across the contours. The perpendicular distance between two contours with frequencies differing by  $d\omega$  is  $d\omega/|\mathbf{v}_\omega|$ . This yields a different form of the integral:

$$\int [\dots] d^2\mathbf{k} = \int [\dots] \frac{d\omega dk_\parallel}{|\mathbf{v}_\omega|} \quad (\text{IV.2.6})$$

where  $dk_{\parallel}$  is the length segment along the contour. But  $dk_{\parallel}$  can also be written in terms of  $d\theta$ , by noticing that the arc  $kd\theta$  is the projection of  $dk_{\parallel}$ , so that  $kd\theta = dk_{\parallel}|u_{\omega}|/|\mathbf{v}_{\omega}|$ . This yields another representation:

$$\int [\dots] d^2\mathbf{k} = \int [\dots] \frac{d\omega k_{\omega}(\theta) d\theta}{|u_{\omega}(\theta)|} . \quad (\text{IV.2.7})$$

Thus, both the full group velocity  $\mathbf{v}_g(\theta)$  and its radial component  $u_{\omega}(\theta)$  can be helpful in integrating over the  $\mathbf{k}$ -space.

Let us now rewrite Green's function at large distances  $r \gg k_{\omega}^{-1}$  in terms of the properties of the dispersion law. We assume the decay  $\gamma_{\mathbf{k}}$  in the medium to be negligible, but positive:  $\gamma_{\mathbf{k}} \rightarrow +0$ . The real-space function is obtained as an integral over the  $\mathbf{k}$ -space:

$$G(\omega, \mathbf{r}) = \int \frac{d^2\mathbf{k}}{(2\pi)^2} \frac{1}{\omega - \omega_{\mathbf{k}} + i0} e^{i\mathbf{k}\cdot\mathbf{r}} , \quad (\text{IV.2.8})$$

with the help of the quantities introduced above. For a given direction  $\theta$ , the integrand has a pole at  $k = k_{\omega}(\theta)$ . In its vicinity,  $G(\omega, \mathbf{k})$  behaves as

$$G_{\mathbf{k}}(\omega) \approx \frac{1}{-u_{\omega}(\theta)[k - k_{\omega}(\theta)] + i0} . \quad (\text{IV.2.9})$$

Hence, the integral over  $|\mathbf{k}|$  can be computed via the method of residues. Due to the  $i0$  contribution, the pole lies in the upper half-plane for  $u_{\omega} > 0$ , and in the lower half-plane otherwise. On the other hand, the contour can be closed in the upper half-plane if  $\hat{\theta} \cdot \hat{\mathbf{r}}$  is positive, and in the lower half-plane otherwise. Thus we see that the pole is caught by the integration contour if  $u_{\omega}(\theta)$  and  $\hat{\theta} \cdot \hat{\mathbf{r}}$  are of the same sign. If the contour is closed in the upper half-plane, the residue is taken with the factor of  $2\pi i$ , otherwise, it is taken with the factor of  $-2\pi i$ . This can be summarised as

$$G(\omega, \mathbf{r}) = -i \oint \frac{k_{\omega}(\theta) d\theta}{2\pi |u_{\omega}(\theta)|} e^{ik_{\omega}(\theta)r \cos(\theta - \alpha)} \Theta[u_{\omega}(\theta) \cos(\theta - \alpha)] , \quad (\text{IV.2.10})$$

where  $\Theta(x)$  is the Heaviside function, and  $\alpha$  is the direction of  $\mathbf{r}$ . The resulting integral over angle  $\theta$ , in general, involves an oscillating function of  $\theta$ . In the far field,  $k_{\omega}(\theta)r \gg 1$ , the oscillations become fast, and the integral can be computed by the saddle-point method. The primary contribution comes from the vicinity of the point  $\theta^*$  where the phase of the oscillations is stationary:

$$\left. \frac{\partial}{\partial \theta} k_{\omega}(\theta) \cos(\theta - \alpha) \right|_{\theta=\theta^*} = 0 . \quad (\text{IV.2.11})$$

This yields an equation for  $\theta^*(\alpha)$ :

$$k'_{\omega}(\theta^*) \cos(\theta^* - \alpha) = k_{\omega}(\theta^*) \sin(\theta^* - \alpha) . \quad (\text{IV.2.12})$$

This can be paraphrased as follows: at the point  $\theta = \theta^*(\alpha)$ , the unit normal to the contour  $k = k_{\omega}(\theta)$  is parallel to  $\hat{\mathbf{r}}$ , i. e.  $\mathbf{v}_g(\theta^*) \parallel \hat{\mathbf{r}}$ , as shown in Fig. IV.2. To see this, one may compute the cross-product

$$\mathbf{v}_{\omega}(\theta^*) \times \hat{\mathbf{r}} = \frac{u_{\omega}(\theta^*)}{k_{\omega}(\theta^*)} [k_{\omega}(\theta^*) \sin(\theta^* - \alpha) - k'_{\omega}(\theta^*) \cos(\theta^* - \alpha)] = 0 , \quad (\text{IV.2.13})$$

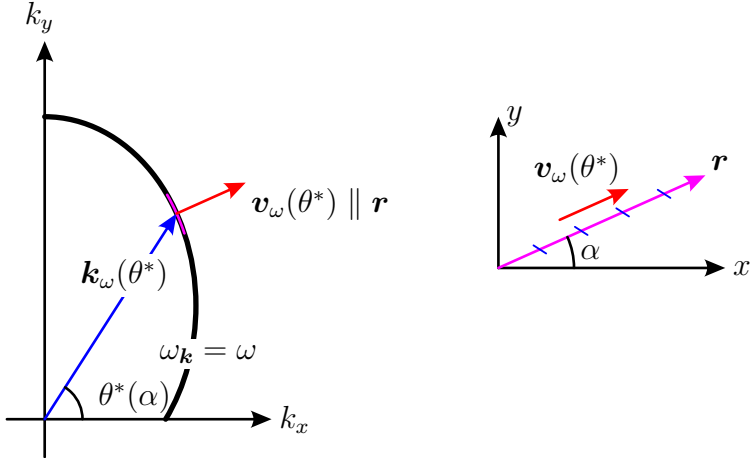


Figure IV.2: For a given propagation direction  $\alpha = \arg \mathbf{r}$  in the real space, the outgoing wave is formed by the segment of the constant energy surface at which the group velocity is directed parallel to  $\mathbf{r}$ .

which vanishes by virtue of Eq. (IV.2.12). There are at least two such points on a smooth closed constant-frequency contour, and one should consider only those for which  $u_\omega(\theta^*) \cos(\theta^* - \alpha) > 0$ .

In the vicinity of each allowed  $\theta^*(\alpha)$ , the integral takes the form

$$G(\omega, \mathbf{r}) = -\frac{ik_\omega(\theta^*)}{2\pi u_\omega(\theta^*)} e^{i\mathbf{k}_\omega(\theta^*) \cdot \mathbf{r}} \int_{-\infty}^{\infty} d\xi e^{iQ\xi^2/2}, \quad (\text{IV.2.14})$$

where  $\xi = \theta - \theta^*$ . [The integral is determined by a narrow vicinity  $\theta - \theta^* \sim (k_\omega r)^{-1/2}$ , hence the integration limits can be extended to infinity.] The coefficient  $Q$  of the quadratic part is given by

$$Q \equiv \left. \frac{\partial^2}{\partial \theta^2} k_\omega(\theta) \cos(\theta - \alpha) \right|_{\theta=\theta^*}. \quad (\text{IV.2.15})$$

The standard Gaussian integration then yields

$$G(\omega, \mathbf{r}) = \sum_{\theta^*(\alpha)} \frac{k_\omega(\theta^*)}{|u_\omega(\theta^*)|} e^{i\mathbf{k}_\omega(\theta^*) \cdot \mathbf{r}} \sqrt{\frac{2\pi}{-iQ|\mathbf{r}|}}, \quad (\text{IV.2.16})$$

where the summation is performed over all points  $\theta^*$  that contribute to the outgoing wave. To clarify the meaning of the quantity  $Q$ , one may vary the propagation angle  $\alpha$  by  $d\alpha$  and compute the respective change  $d\theta^*$ . Since Eq. (IV.2.12) holds on the curve  $\theta = \theta^*(\alpha)$ , one may differentiate this relation with respect to  $\theta$  and  $\alpha$ . This way, one finds

$$Qd\theta^* = [-k'_\omega(\theta^*) \sin(\theta^* - \alpha) - k_\omega(\theta^*) \cos(\theta^* - \alpha)] d\alpha. \quad (\text{IV.2.17})$$

Eliminating  $k'_\omega(\theta)$  from Eq. (IV.2.12), we write

$$Qd\theta^* = -\frac{k_\omega(\theta^*)}{\cos(\theta^* - \alpha)} d\alpha = -\frac{k_\omega(\theta^*) v_\omega(\theta^*)}{u_\omega(\theta^*)} d\alpha. \quad (\text{IV.2.18})$$

Eventually, we find

$$G(\omega, \mathbf{r} \gg k_\omega^{-1}) = \sum_{\theta^*(\alpha)} \left[ \frac{k_\omega(\theta^*)}{2\pi i u_\omega(\theta^*) v_\omega(\theta^*)} \frac{d\theta^*}{d\alpha} \right]^{1/2} \cdot \frac{1}{\sqrt{|\mathbf{r}|}} \exp(i\mathbf{k}_\omega(\theta^*) \cdot \mathbf{r}) . \quad (\text{IV.2.19})$$

All the quantities here are to be evaluated at points  $\mathbf{k}^*$  on the contour of constant frequency  $\omega$  such that  $\mathbf{v}_\omega^* \parallel \hat{\mathbf{r}}$ . Thus, we obtained a diverging cylindrical wave. For an isotropic dispersion,  $k_\omega(\theta) = \text{const}$ ,  $u_\omega(\theta) = v_\omega(\theta) = \text{const}$ ,  $\theta^* = \alpha$ , one can derive an exact result;  $G(\omega, r) = k_\omega / u_\omega H_0^{(1)}(k_\omega r)$ , which reproduces Eq. (IV.2.19) at  $k_\omega r \gg 1$ . A similar analysis in three dimensions would yield a diverging spherical wave,  $\exp(i\mathbf{k}_\omega^* \cdot \mathbf{r})/|\mathbf{r}|$ .

One may also notice that the resulting expression is singular if the propagation angle  $\alpha$  is stationary (e.g. maximal or minimal), as the derivative  $d\theta^*/d\alpha$  is diverging. This condition corresponds to rainbow-like caustics and requires a separate analysis: one has to expand the phase  $r k_\omega(\theta) \cos(\theta - \alpha)$  to the third order in  $\theta - \theta_c$ . Integration over  $\theta$  then yields Green's function in the form

$$G_c(\omega, r) \propto \frac{1}{r^{1/3}} \text{Ai}(\kappa(\alpha - \alpha_c)r^{2/3}) e^{i\mathbf{k}_c \cdot \mathbf{r}} , \quad (\text{IV.2.20})$$

where  $\alpha_c$  is the angle of the caustic,  $\text{Ai}$  is the Airy function, and  $\kappa$  is a constant. At sufficiently large distances,  $k_\omega r \gg |\alpha - \alpha_c|^{3/2}$ , one recovers asymptotic behaviour of the Airy function, which results in the square-root singularity near the caustic.

One can then find the flux of quanta emitted in a given direction by a source  $S(\mathbf{k})$ . Writing  $\psi(\mathbf{r}) = S(\mathbf{k}^*) G(\omega, \mathbf{r})$ , one finds the flux as

$$J(\mathbf{r}) = v_\omega(\theta^*) |\psi(\mathbf{r})|^2 = \sum_{\theta^*} \frac{|S(\mathbf{k}^*)|^2}{2\pi |\mathbf{r}|} \frac{k_\omega^*}{u_\omega^*} \left| \frac{d\theta^*}{d\alpha} \right| . \quad (\text{IV.2.21})$$

(When several points contribute, we neglect the interference between fastly oscillating terms.) The net flux emitted by a source  $S(\mathbf{k})$  into an infinitesimal sector of angular width  $d\alpha$  is therefore

$$J(\mathbf{r}) |\mathbf{r}| d\alpha = \frac{|S(\mathbf{k}^*)|^2}{2\pi} \frac{k_\omega^* d\theta^*}{u_\omega^*} d\theta^* . \quad (\text{IV.2.22})$$

This simplifies computation of the scattering cross-section and gives a proper normalisation of the scattering amplitude.

Another quantity that can be related to Green's function is the density of states  $g(\omega)$  defined as

$$g(\omega) = -\frac{1}{\pi} \text{Im} G(\omega, \mathbf{r} = 0) . \quad (\text{IV.2.23})$$

The imaginary part is proportional to the Lorentzian that can be approximated with a delta function,

$$g(\omega) = \frac{1}{\pi} \int \frac{d^2 \mathbf{k}}{(2\pi)^2} \frac{\gamma_{\mathbf{k}}}{(\omega - \omega_{\mathbf{k}})^2 + \gamma_{\mathbf{k}}} \approx \int \frac{d^2 \mathbf{k}}{(2\pi)^2} \delta(\omega - \omega_{\mathbf{k}}) . \quad (\text{IV.2.24})$$

Thus, one may express the density of states as an integral over the constant-frequency contour:

$$g(\omega) = \frac{1}{2\pi} \oint \frac{d\theta}{2\pi} \frac{k_\omega(\theta)}{u_\omega(\theta)} = \frac{1}{4\pi^2} \oint \frac{dl_\omega}{v_\omega(\theta)} . \quad (\text{IV.2.25})$$

### IV.3 Propagation in the time domain

In the previous section, we analysed the response of a medium at a particular frequency. To analyse propagation of time-modulated signals, one may need the respective quantities in the time-domain. Consider a source of the form  $S(\mathbf{k})F(t)$ , where the Fourier spectrum  $F_\omega$  of  $F(t)$  has a narrow peak near a given carrier frequency  $\omega_0$ . At large distances, the outgoing wave is given by

$$\psi(t, \mathbf{r}) = \int \frac{d\omega}{2\pi} F_\omega e^{-i\omega t} G(\omega, \mathbf{r}) S(\mathbf{k}_\omega(\mathbf{r})) \quad (\text{IV.3.1})$$

with  $G(\omega, \mathbf{r})$  given by Eq. (IV.2.19). The Fourier image  $F_\omega$ , in turn, can be written as

$$F_\omega = \int_{-\infty}^{\infty} dt' F(t') e^{i\omega t'} , \quad (\text{IV.3.2})$$

and one obtains a retarded wave of the form

$$\psi(t, \mathbf{r}) = \int_{-\infty}^{\infty} \frac{d\omega}{2\pi} \int_{-\infty}^{\infty} dt' F(t') e^{-i\omega(t-t')} G(\omega, \mathbf{r}) S(\mathbf{k}_\omega(\mathbf{r})) \quad (\text{IV.3.3})$$

In the frequency integral, preexponential factors  $F_\omega$ ,  $k_\omega$ ,  $u_\omega$ , etc are relatively smooth functions of  $\omega$ . In the exponential factor, though, one encounters a rapid dependence on  $\omega$  from  $-i\omega(t-t') + i\mathbf{k}_\omega^* \cdot \mathbf{r}$  with large  $t-t'$  and  $\mathbf{r}$ . This would result in a rapid oscillation and suppresses the integral, unless the phase is stationary with respect to changing  $\omega$ . This is achieved if

$$-t + t' + \frac{\partial \mathbf{k}_\omega^*}{\partial \omega} \cdot \mathbf{r} = 0 . \quad (\text{IV.3.4})$$

Since  $\mathbf{k}_\omega^*$  is chosen in such a way as to make the group velocity parallel to  $\hat{\mathbf{r}}$ , the above condition amounts to retarded time  $t'$  defined by

$$t' = t - \frac{|\mathbf{r}|}{|\mathbf{v}_\omega|} , \quad (\text{IV.3.5})$$

with group velocity  $\mathbf{v}_\omega(\theta^*)$  at the relevant point of the constant-frequency contour. Recalling that

$$\delta(t) = \int_{-\infty}^{\infty} \frac{d\omega}{2\pi} e^{-i\omega t} , \quad (\text{IV.3.6})$$

one may recast the outgoing wave as

$$\psi(t, \mathbf{r}) = G(\omega_0, \mathbf{r}) S(\mathbf{k}^*(\mathbf{r})) F\left(t - \frac{|\mathbf{r}|}{|\mathbf{v}_\omega(\theta^*)|}\right) , \quad (\text{IV.3.7})$$

with all the quantities in Eq. IV.3.7 evaluated at the carrier frequency  $\omega_0$ . Thus, the outgoing wave is delayed by  $|\mathbf{r}|/|\mathbf{v}_\omega|$ , as one might expect. (When several values of  $\mathbf{k}^*$  correspond to a given direction  $\hat{\mathbf{r}}$ , one has to sum up the contributions of all the branches.)

Let us also consider the case of a near field,  $k_\omega r \ll 1$ . The response can be written as a sum over all wavevectors:

$$\psi(t, \mathbf{r}) = \sum_{\mathbf{k}} \int_{-\infty}^{\infty} \frac{d\omega}{2\pi} \int_{-\infty}^{\infty} dt' \frac{S_{\mathbf{k}} F(t')}{\omega - \omega_{\mathbf{k}} + i\gamma_{\mathbf{k}}} e^{i\mathbf{k}\cdot\mathbf{r}} e^{-i\omega(t-t')} . \quad (\text{IV.3.8})$$

The sum over  $\mathbf{k}$  is determined by wavevectors such that  $\mathbf{k} \cdot \mathbf{r} \lesssim 1$ . For most of this integration domain,  $\omega_{\mathbf{k}} \gg \omega$ , and one can expand the result to the two lowest orders in  $\omega$ :

$$\psi(t, \mathbf{r}) = \sum_{\mathbf{k}} \int_{-\infty}^{\infty} \frac{d\omega}{2\pi} \int_{-\infty}^{\infty} dt' S_{\mathbf{k}} F(t') \left[ -\frac{1}{\omega_{\mathbf{k}}} - \frac{\omega}{\omega_{\mathbf{k}}^2} \right] e^{i\mathbf{k}\cdot\mathbf{r}} e^{-i\omega(t-t')} . \quad (\text{IV.3.9})$$

Integration over  $\omega$  yields

$$\psi(t, \mathbf{r}) = \Psi_0(\mathbf{r}) F(t) + \Psi_1(\mathbf{r}) \frac{dF}{dt} , \quad (\text{IV.3.10})$$

where

$$\Psi_0(\mathbf{r}) \equiv - \sum_{\mathbf{k}} \frac{S_{\mathbf{k}}}{\omega_{\mathbf{k}}} e^{i\mathbf{k}\cdot\mathbf{r}} , \quad \Psi_1(\mathbf{r}) \equiv -i \sum_{\mathbf{k}} \frac{S_{\mathbf{k}}}{\omega_{\mathbf{k}}^2} e^{i\mathbf{k}\cdot\mathbf{r}} . \quad (\text{IV.3.11})$$

We see that in the near-field limit the dominant contribution  $\propto F(t)$  is not retarded: the outgoing wave is generated instantaneously. Weak retardation is accounted for by the second term  $\propto dF/dt$ . Note that the near field is mediated by all wavevectors, and the constant-frequency contour  $k_\omega(\theta)$  does not play a role here. The resulting sums over  $\mathbf{k}$  usually diverge at  $\mathbf{r} = 0$ , which results in quantities algebraically singular in  $|\mathbf{r}|$ :  $\Psi_{0,1}(\mathbf{r}) \propto |\mathbf{r}|^{-a}$ , with  $a > 0$ , or perhaps  $\Psi_{0,1}(\mathbf{r}) \propto \log |\mathbf{r}|$ .

## IV.4 Dynamics of the resonator and its self-energy

Let us now discuss the dynamics of the resonator coupled to the medium. The equations (IV.1.7) and (IV.1.6) can be readily solved by eliminating the bulk variables  $\psi_{\mathbf{k}}$  and deriving the effective dynamics of the local mode. One may write

$$\psi_{\mathbf{k}} = \psi_{\mathbf{k}}^{(\text{inc})} + \frac{\Delta_{\mathbf{k}} \varphi}{\omega - \omega_{\mathbf{k}} + i\gamma_{\mathbf{k}}} , \quad (\text{IV.4.1})$$

with the incident wave

$$\psi_{\mathbf{k}}^{(\text{inc})} \equiv \frac{S_{\mathbf{k}}}{\omega - \omega_{\mathbf{k}} + i\gamma_{\mathbf{k}}} . \quad (\text{IV.4.2})$$

Thus, the scattered wave  $\psi_{\mathbf{k}}^{(\text{scat})}$  is determined by the local mode:

$$\psi_{\mathbf{k}}^{(\text{scat})} = \frac{\Delta_{\mathbf{k}} \varphi}{\omega - \omega_{\mathbf{k}} + i\gamma_{\mathbf{k}}} . \quad (\text{IV.4.3})$$

Substituting the above expression for  $\psi_{\mathbf{k}}$  into the equation for the local mode, one finds:

$[\omega - \Omega_0 + i\Gamma_0 - \Sigma(\omega)] \varphi = \sum_{\mathbf{k}} \bar{\Delta}_{\mathbf{k}} \psi_{\mathbf{k}}^{(\text{inc})} .$

(IV.4.4)

Here  $\Sigma(\omega)$  is *the self-energy* of the resonant mode due to its coupling with the medium:

$$\boxed{\Sigma(\omega) \equiv \sum_{\mathbf{k}} \frac{|\Delta_{\mathbf{k}}|^2}{\omega - \omega_{\mathbf{k}} + i\gamma_{\mathbf{k}}}} . \quad (\text{IV.4.5})$$

Eq. (IV.4.4) describes a linear system driven by an incident wave. The respective response is maximal at the resonant pole determined by the condition

$$\omega = \Omega_0 - i\Gamma_0 + \Sigma(\omega) . \quad (\text{IV.4.6})$$

The real part of  $\Sigma(\omega)$  therefore contributes to renormalisation of the resonant frequency, and the imaginary part takes care of radiative broadening. Writing the pole position as  $\Omega_{\text{res}} - i\Gamma_{\text{res}}$ , one may write, for a well-resolved resonance:

$$\Omega_{\text{res}} = \Omega_0 + \sum_{\mathbf{k}} \frac{|\Delta_{\mathbf{k}}|^2 (\Omega_{\text{res}} - \omega_{\mathbf{k}})}{(\Omega_{\text{res}} - \omega_{\mathbf{k}})^2 + \gamma_{\mathbf{k}}^2} , \quad (\text{IV.4.7})$$

$$\Gamma_{\text{res}}(\omega) = \Gamma_0 + \Gamma_{\text{rad}}(\Omega_{\text{res}}) \quad (\text{IV.4.8})$$

with the radiative contribution to the linewidth

$$\boxed{\Gamma_{\text{rad}}(\omega) = \sum_{\mathbf{k}} \frac{\gamma_{\mathbf{k}}}{(\omega - \omega_{\mathbf{k}})^2 + \gamma_{\mathbf{k}}^2} |\Delta_{\mathbf{k}}|^2} . \quad (\text{IV.4.9})$$

(For a single mode, the resonance can be considered well-resolved when  $\Gamma_{\text{res}}(\omega) \ll \Omega_{\text{res}}$ . When several resonant modes are present, one should compare the width with the spacing between the modes, see Sec. VI.4 for further discussion.)

While for well-resolved resonances we only need the value of  $\Gamma_{\text{res}}(\Omega_{\text{res}})$ , we nevertheless retain the frequency dependence in multidimensional case. The reason for this is that in multi-dimensional case the radiative rate is likely to vary as a function of frequency: for higher frequencies, there are more available final states for radiation. An example of this is radiative friction of an oscillating charge in three dimensions, which is often described via the term proportional to  $\ddot{\mathbf{r}}$ , and which corresponds to  $\Gamma_{\text{res}}(\omega) \sim \omega^3$ . Such frequency dependence can be significant across a broad resonance, and may result in an asymmetry of the respective Lorentzian. Near the resonant pole, one may write

$$\frac{1}{\omega - \Omega_0 + i\Gamma_0 - \Sigma(\omega)} \approx \frac{Z_{\text{res}}}{\omega - \Omega_{\text{res}} + iZ_{\text{res}}\Gamma_{\text{res}}(\omega)} , \quad (\text{IV.4.10})$$

with the factor

$$\frac{1}{Z_{\text{res}}} \equiv 1 - \left. \frac{\partial \text{Re } \Sigma}{\partial \omega} \right|_{\omega=\Omega_{\text{res}}} \quad (\text{IV.4.11})$$

giving the residue at the pole. (In quantum-field theory contexts it is sometimes known as the wavefunction renormalisation, in many-body theory it is known as the quasiparticle residue.) The factor  $Z_{\text{res}}$  can be eliminated from the equations if the field  $\varphi$  is redefined as  $\varphi \rightarrow \varphi\sqrt{Z_{\text{res}}}$ . The partial derivative in Eq. (IV.4.11) is expected to be of the order of  $\Gamma_{\text{rad}}/\Omega_0$  and is therefore not as important as the renormalisation of the resonant frequency or the resonant width. Hence one may often approximate  $Z_{\text{res}} \approx 1$  for simplicity. When this assumption becomes invalid,

though, one should bear in mind that the resonant linewidth is given by  $Z_{\text{res}}\Gamma_{\text{res}}$ , rather than just  $\Gamma_{\text{res}}$ . We see that increasing the coupling  $\Delta_k$  affects the linewidth in two ways: it is increased because of increase in  $\Gamma_{\text{res}}$ , but at large  $\Delta_k$  this growth may be in fact suppressed by the  $Z$  factor, so that the linewidth would not exceed the resonant frequency.

The two expressions (IV.4.7) and (IV.4.8) behave rather differently. The modes in the close proximity of the resonant frequency,  $|\Omega_{\text{res}} - \omega_k| \lesssim \gamma_k$ , do not contribute to the renormalisation of the resonant frequency, as the integrand of Eq. (IV.4.7) is odd in this domain. However, vanishing of this “on-shell” contribution does not indicate the renormalisation vanishes: in fact, in many important cases the relevant integral over the  $\mathbf{k}$ -space may diverge at large wavevectors, which yields a short-range (near-field, “off-shell”, or reactive) contribution to  $\Omega_{\text{res}}$ . Such a contribution can be extracted either from numerical simulations, or experimental measurements. The divergence can be also transformed by noticing that the behaviour at large wave vectors essentially represents the near-field physics in which the retardation is not important and which therefore can be evaluated assuming zero frequency. (See Sec. VI.3 for a more detailed discussion.) As we will show in the next chapter, it may be natural to repeat this procedure. Thus, one may represent the self-energy singling out the two lowest orders:

$$\text{Re } \Sigma(\omega) = \Sigma_{\text{nrf}} + \Sigma'_{\text{nrf}}\omega + \sum_k \frac{|\Delta_k|^2 \omega^2}{\omega_k^2 (\omega - \omega_k)} \quad (\text{IV.4.12})$$

with the instantaneous, near-field contribution

$$\Sigma_{\text{nrf}} = \Sigma(\omega = 0) = - \sum_k \frac{|\Delta_k|^2}{\omega_k} , \quad \Sigma'_{\text{nrf}} = - \sum_k \frac{|\Delta_k|^2}{\omega_k^2} . \quad (\text{IV.4.13})$$

The first two terms in Eq. (IV.4.12) can be found by solving for the resonant modes numerically, in the near-field approximation described in Sec. VI.3. Then, the remaining term in Eq. (IV.4.12) quickly decays as  $\omega_k^3$  and the converging integral can be obtained by integrating over the continuous spectrum of an infinite medium.

In contrast to  $\text{Re } \Sigma(\omega)$ , the resonant linewidth  $\Gamma_{\text{res}}(\omega)$ , is determined by the “on-shell” (i.e., far-field, active) effects involving emission of a runaway excitation. For  $\gamma_k \rightarrow +0$ , the narrow Lorentzian in the expression for  $\Gamma_{\text{res}}$  can be replaced with a delta function:

$$\Gamma_{\text{rad}}(\omega) = \pi \sum_k |\Delta_k|^2 \delta(\omega - \omega_k) . \quad (\text{IV.4.14})$$

This relation resembles Fermi’s golden rule, in which the rate of emission is given by the square of the relevant hybridisation matrix element  $\Delta_k$  and the density of final states. In fact, the delta-function in Eq. (IV.4.14) represents the relevant density of states. In one dimension, integration over  $k$  yields the density of states  $1/(2\pi v)$ , and the contribution to  $\Gamma_{\text{res}}(\omega)$  acquires the familiar form,  $|\Delta|^2/(2v)$ . In an arbitrary dimension, one may integrate over the magnitude of  $\mathbf{k}$ , by writing the delta function in the form (cf the calculation of the density of states):

$$\delta(\omega - \omega_k) = \frac{1}{|u_\omega(\theta)|} \delta(k - k_\omega) . \quad (\text{IV.4.15})$$

The quantity  $k_\omega(\theta)$  is the root of the dispersion relation in a given direction, and  $u_\omega(\theta) \equiv d\omega/d|\mathbf{k}|$  is the group velocity in the radial direction introduced in Sec.IV.2. In two dimensions, e.g., one may rewrite the relation for the linewidth in the form of an integral over the surface of constant frequency parametrised by the polar angle  $\theta$ :

$$\boxed{\Gamma_{\text{rad}}(\omega) = \frac{1}{2} \oint \frac{d\theta}{2\pi} \frac{k_\omega(\theta)}{u_\omega(\theta)} |\Delta_\theta|^2 = \frac{1}{4\pi} \oint_{\omega_k=\omega} \frac{dl_\omega |\Delta_\theta|^2}{v_\omega(\theta)} .} \quad (\text{IV.4.16})$$

Here  $\Delta_\theta$  is the hybridisation evaluated at the respective  $\mathbf{k}$ -space point:  $\mathbf{k} = k_\omega(\cos \theta, \sin \theta)$ ,  $v_\omega(\theta)$  is the magnitude of group velocity, and  $dl_\omega$  is the length element on the constant-frequency contour. A similar relation can be also derived in three dimensions.

We also notice that the self-energy part  $\Sigma(\omega)$  considered as a function of complex variable  $\omega$  has no singularities at  $\text{Im } \omega > 0$ , as it represents a retarded function (i.e., its Fourier transform  $\Sigma(t)$  is only non-zero for  $t > 0$ ). Hence it obeys the dispersion relation: its real part can be reconstructed from its imaginary part  $\Gamma_{\text{rad}}(\omega)$ , up to a constant. We write this relation by subtracting the near-field contribution, as in Eq. (IV.4.13)

$$\text{Re } \Sigma(\omega) = \Sigma_{\text{nrf}} + \Sigma'_{\text{nrf}} \omega + \frac{1}{\pi} \int_0^\infty \left( \frac{\omega}{\omega'} \right)^2 \frac{\Gamma_{\text{rad}}(\omega') d\omega'}{(\omega - \omega')} , \quad (\text{IV.4.17})$$

where the singular integral should be understood as the principal value:

$$\int_0^\infty [\dots] d\omega' = \lim_{\epsilon \rightarrow +0} \left\{ \int_0^{\omega-\epsilon} + \int_{\omega+\epsilon}^\infty \right\} [\dots] d\omega' . \quad (\text{IV.4.18})$$

Here we integrated over positive frequencies, as  $\text{Im } \Sigma(\omega)$  is finite only for  $\omega > 0$ , which is an artefact of the resonant approximation. If the non-resonant terms  $\Delta'_k \varphi \psi_k$  are retained, there is also a respective contribution from  $\Gamma_{\text{rad}}(\omega)$  at  $\omega < 0$ . The respective relation for  $\text{Re } \Sigma(\omega)$  can be recast as

$$\text{Re } \Sigma(\omega) = \Sigma_{\text{nrf}} + \omega \Sigma_{\text{nrf}} + \frac{1}{\pi} \int_0^\infty \left( \frac{\omega}{\omega'} \right)^2 \frac{\Gamma_{\text{rad}}(\omega') d\omega'}{(\omega - \omega')} - \sum_k \frac{|\Delta'_k|^2}{(\omega + \omega_k) \omega_k} . \quad (\text{IV.4.19})$$

## IV.5 Solving the resonant-scattering problem

Once  $\Omega_{\text{res}}$  and  $\Gamma_{\text{res}}(\omega)$  have been determined, one may write the solution for the local mode and for the scattered wave. Consider the case of a plane incident wave:

$$\psi_k^{(\text{inc})} = A_{\text{inc}} \delta(\mathbf{k} - \mathbf{k}_{\text{inc}}) . \quad (\text{IV.5.1})$$

Then, near the resonance, one finds

$$\varphi = \frac{A_{\text{inc}} \bar{\Delta}_{\text{inc}} Z_{\text{res}}}{\omega - \omega_{\text{res}} + i Z_{\text{res}} \Gamma_{\text{res}}(\omega)} , \quad (\text{IV.5.2})$$

with  $\Delta_{\text{inc}} \equiv \Delta_{\mathbf{k}}$  at the incident wave vector  $\mathbf{k}_{\text{inc}}$ . This readily yields the scattered wave in the  $\mathbf{k}$ -space:

$$\psi_{\mathbf{k}}^{(\text{scat})} = G_{\mathbf{k}}(\omega) \frac{A_{\text{inc}} \Delta_{\mathbf{k}} \bar{\Delta}_{\text{inc}} Z_{\text{res}}}{\omega - \Omega_{\text{res}} + iZ_{\text{res}} \Gamma_{\text{res}}(\omega)} . \quad (\text{IV.5.3})$$

One may then use Eq.(IV.2.19) to derive the scattered wave in the real space, and then obtain the scattering amplitude by normalising the incoming wave by unit flux:  $A_{\text{inc}} = 1/\sqrt{v_{\text{inc}}}$ . The scattering amplitude in two dimensions takes the form

$$f(\mathbf{k}, \mathbf{k}') = \sqrt{\frac{|\mathbf{k}|}{2\pi|u_{\omega}(\mathbf{k})|v_{\omega}(\mathbf{k}')}} \left| \frac{d\theta(\mathbf{k})}{d\alpha} \right| \frac{\Delta_{\mathbf{k}} \bar{\Delta}'_{\mathbf{k}'} Z_{\text{res}}}{\omega - \Omega_{\text{res}} + iZ_{\text{res}} \Gamma_{\text{res}}} . \quad (\text{IV.5.4})$$

The differential scattering cross-section  $d\sigma$  into angle interval  $d\alpha$  is defined in the usual way:

$$d\sigma = \sum_{\theta^*(\alpha)} |f(\mathbf{k}' \rightarrow \mathbf{k})|^2 d\alpha . \quad (\text{IV.5.5})$$

The total scattering cross-section can be obtained by integrating the result over all the propagation angles  $\alpha_{\mathbf{k}}$ . The result can be recast in terms of the radiative contribution  $\Gamma_{\text{rad}}(\omega)$  to the linewidth, by virtue of Eq. (IV.4.16)

$$\sigma_{\text{tot}}(\mathbf{k}' \rightarrow \text{all}, \omega) = \frac{2}{v(\mathbf{k}')} \frac{\Gamma_{\text{rad}}(\omega) |\Delta_{\mathbf{k}'}|^2 Z_{\text{res}}^2}{(\omega - \Omega_{\text{res}})^2 + Z_{\text{res}}^2 [\Gamma_0 + \Gamma_{\text{rad}}(\omega)]^2} . \quad (\text{IV.5.6})$$

One can also compute the absorption cross-section:

$$\sigma_{\text{abs}}(\omega) = \frac{\Gamma_0}{\Gamma_{\text{rad}}(\omega)} \sigma_{\text{tot}}(\omega) . \quad (\text{IV.5.7})$$

The scattering amplitude (IV.5.4) obeys the optical theorem which links the total cross-section to the imaginary part of the forward-scattering amplitude:

$$\sigma_{\text{tot}}(\omega) + \sigma_{\text{abs}}(\omega) = \sqrt{\frac{8\pi u_{\omega}(\mathbf{k})}{|\mathbf{k}| v_{\omega}(\mathbf{k})}} \left| \frac{d\alpha}{d\theta} \right| \text{Im } f(\mathbf{k} \rightarrow \mathbf{k}) . \quad (\text{IV.5.8})$$

Eq. (IV.5.4) is equivalent to the familiar Breight-Wigner formula: indeed, the hybridisations on the top can be linked to square roots of the relevant contributions to the resonant linewidth. We see that the resonance occurs at the frequency of the local mode, regardless of the incident and scattered wave vector. The angular dependence of scattering mimics that of the hybridisation coupling  $\Delta_{\mathbf{k}}$  evaluated at the contour of constant frequency  $\omega$ .

Let us consider the behaviour of  $\sigma_{\text{tot}}(\omega)$  when the coupling strength  $\Delta_{\theta}$  is increased preserving its angular dependence. For simplicity we assume that  $\Gamma_0$  can be neglected. At weak coupling, away from the resonance, this would result in the respective increase in the scattering cross-section. However, near the resonance, the cross-section in fact is saturated:

$$\sigma_{\text{tot}}(\omega = \Omega_{\text{res}}) = \frac{2}{v_{\text{inc}}} \frac{|\Delta_{\text{inc}}|^2}{\Gamma_{\text{rad}}} \propto \frac{1}{\Gamma_{\text{rad}}(\omega)} \frac{d\Gamma_{\text{rad}}}{d\theta_{\text{inc}}} . \quad (\text{IV.5.9})$$

(The last factor represents the partial radiative linewidth for the incident wave.) Note that the resulting quantity depends only upon the directivity and not upon the overall emission rate. This saturation is related to the fact that the scattered wave is emitted by a single resonant mode. Such saturation is known as *the unitary limit* in the scattering theory: total cross-section in a given partial-wave channel cannot exceed the limit set by the wavelength. For this reason, the scattering cross-section in the strong-coupling regime may exhibit rather broad or flattened resonant peaks deviating from the usual Lorentzian lineshape.

# Chapter V

## Two-dimensional scattering in thin magnetic films

In this chapter, we apply the general formalism of the previous chapter to the case of a thin magnetic film as a propagation medium. The films relevant for the MANNNA project are expected to be of thickness of 20–50 nm. For this reason, we present the analytical theory in the thin-film approximation which assumes small wavenumbers:  $|\mathbf{k}|d \lesssim 1$ . (For the actual calculations, though, this approximation is not necessary: the profile of a mode at a given wave vector can be easily obtained by solving the relevant one-dimensional problem numerically.) We first link the abstract wave  $\psi_{\mathbf{k}}$  to the magnetisation distribution, and then use this to compute the interaction between such a wave and a point-like Kittel dipole. This gives a more microscopic insight into the directivity and chirality of scattered waves, as well as frequency dependence. We give order-of-magnitude estimates for the coupling, and discuss its frequency dependence. We then generalise these results to finite-size resonators with known profiles of the resonant modes, highlighting the role of resonator's geometry.

### V.1 Propagating modes in thin films

The general theory outlined above can be applied to scattering of magnons in thin films by chiral resonators. Here we present a simplified version of this theory,

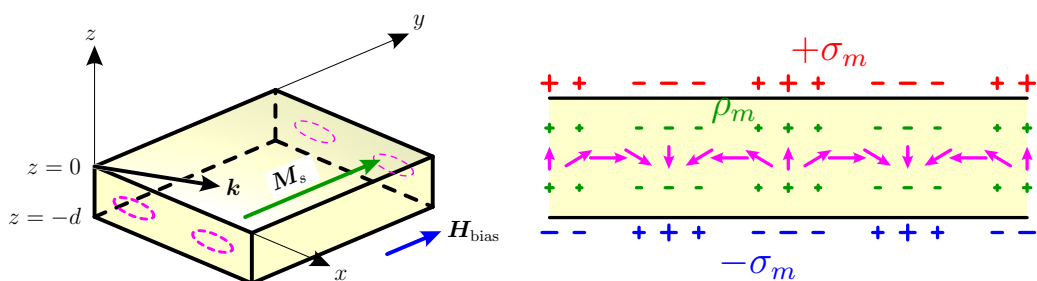


Figure V.1: Left: A thin film is biased and magnetised along the  $y$  axis. The propagating modes are characterised by their in-plane wavevector  $\mathbf{k} = (k_x, k_y)$ . Right: the distribution of magnetisation (magenta), bulk (green) magnetic charges  $\rho_m$  and surface charges  $\pm\sigma_m$ .

in which the variation of magnetisation across the film is neglected. Consider an infinite film of thickness  $d$ , so that  $-d < z < 0$  within the film, see Fig. V.1. Let us assume the film is biased along the  $\hat{\mathbf{y}}$  direction by the field  $H_{\text{bias}}$  and the relevant saturation magnetisation is  $M_s$ . The dynamical magnetisation components are then oriented in the  $xz$  plane. As the film is uniform in the  $xy$  plane, one can seek solutions of the LLG equations in the form

$$m_{x,z}(\mathbf{r}, t) = m_{x,z}(\mathbf{k}, z, t) e^{i\mathbf{k}\cdot\mathbf{r}-i\omega_{\mathbf{k}}t}, \quad (\text{V.1.1})$$

where  $\mathbf{k} = (k_x, k_y)$  is a two-dimensional wavevector. We shall assume the mode to be uniform along  $z$  and therefore will suppress the  $z$  dependence. To obtain the mode, one has to consider demagnetising fields induced by  $m_x$  and  $m_z$ , which can be done by invoking the concept of a magnetic charge. In a film, the magnetic charges are built up in its bulk as well as on the surface, see Fig. V.1. For a mode at a given two-dimensional wavevector  $\mathbf{k} = (k_x, k_y)$ , the respective magnetic charges generated in the bulk of the film are

$$\rho_m = -\nabla \cdot \mathbf{M} = -ik_x m_x. \quad (\text{V.1.2})$$

The two faces of the film carry opposite magnetic charges  $\pm\sigma_m$ , with

$$\sigma_m = m_z. \quad (\text{V.1.3})$$

In what follows, it will be convenient to reason in terms of the magnetic potential  $\Phi_m(z)$  that gives the magnetic field strength  $\mathbf{H} = -\nabla\Phi_m$ . In the Fourier space, the magnetic potential induced by a unit point charge is given by the solution of Helmholtz equation in one dimension,  $\Phi''_m + \mathbf{k}^2\Phi_m = -\delta(z - z')$ , which is well-known:  $(2|\mathbf{k}|)^{-1} \exp[-|\mathbf{k}||z - z'|]$ . Replacing the bulk charges by a single charged plane, one may write the respective magnetic potential as

$$\Phi_m^{(x)} = \frac{\rho_m d}{2|\mathbf{k}|} e^{-|\mathbf{k}|z}, \quad (\text{V.1.4})$$

so that the respective demagnetising field is

$$\mathbf{H}^{(x)} = -\hat{\mathbf{x}}ik_x\Phi_m(z=0) = -\frac{k_x^2 d}{2} \hat{\mathbf{x}} m_x, \quad (\text{V.1.5})$$

which can be described in terms of demagnetisation coefficient

$$N_x(\mathbf{k}) \approx \frac{k_x^2 d}{2|\mathbf{k}|}. \quad (\text{V.1.6})$$

The surface charges form a parallel-plate capacitor. For  $\mathbf{k} = 0$ , there would be no field outside the capacitor, but for  $k \neq 0$  the capacitor becomes leaky. Above the capacitor, the potential is

$$\Phi_m^{(z)}(z > 0) = \frac{\sigma_m}{2|\mathbf{k}|} e^{-|\mathbf{k}|z} (1 - e^{-|\mathbf{k}|d}). \quad (\text{V.1.7})$$

The potential inside is given by

$$\Phi_m(-d < z < 0) = -\frac{\sigma_m}{2|\mathbf{k}|} [e^{|\mathbf{k}|z} - e^{|\mathbf{k}|(-d-z)}]. \quad (\text{V.1.8})$$

The respective vertical demagnetising field is, to the lowest two orders:

$$\mathbf{H}^{(z)} = -\frac{\sigma_m \hat{\mathbf{z}}}{2} [1 + |\mathbf{k}|z + 1 - |\mathbf{k}|(z + d)] = -m_z \left[ 1 - \frac{|\mathbf{k}|d}{2} \right]. \quad (\text{V.1.9})$$

This can be described in terms of the demagnetising factor

$$N_z(\mathbf{k}) \approx 1 - \frac{|\mathbf{k}|d}{2}. \quad (\text{V.1.10})$$

These expressions can be also improved if one assumes a uniform distribution of the magnetisation and averages the fields over  $z$ . This would yield

$$\boxed{N_x(\mathbf{k}) = \frac{k_x^2}{|\mathbf{k}|^2} \left[ 1 - \frac{1 - e^{-|\mathbf{k}|d}}{|\mathbf{k}|d} \right], \quad N_z(\mathbf{k}) = \frac{1 - e^{-|\mathbf{k}|d}}{|\mathbf{k}|d}.} \quad (\text{V.1.11})$$

At  $|\mathbf{k}|d \ll 1$ , these expressions are equivalent. At  $|\mathbf{k}|d \gtrsim 1$ , the expressions with exponents are better-behaved. Nevertheless, one should bear in mind that they cease to be accurate, as the magnetisation is expected to vary significantly across the film.

Introducing the  $\mathbf{k}$ -dependent demagnetising factors reduces the problem at each  $\mathbf{k}$ -space point to that of a Kittel dipole considered in Sec. I.2. To account for exchange effects, one may also incorporate the exchange field  $-J_{\text{ex}} \nabla^2 \mathbf{m}$ , where  $J_{\text{ex}}$  is the exchange integral<sup>1</sup>. Since the exchange field acts similarly on both magnetisation components, it can be considered to be an addition to the bias field, and thus included into the frequencies  $\omega_x(\mathbf{k})$  and  $\omega_z(\mathbf{k})$  that determine the precession ellipse for a given mode. Thus, we approximate the effects of demagnetisation and exchange by writing the LLG equations

$$\dot{m}_x(\mathbf{k}) = \omega_z(\mathbf{k}) m_z(\mathbf{k}), \quad \dot{m}_z(\mathbf{k}) = -\omega_x(\mathbf{k}) m_x(\mathbf{k}), \quad (\text{V.1.12})$$

with wavevector-dependent frequencies

$$\begin{aligned} \omega_x(\mathbf{k}) &= \gamma_s \mu_0 \left( H_{\text{bias}} + N_x(\mathbf{k}) M_s + J_{\text{ex}} \mathbf{k}^2 \right), \\ \omega_z(\mathbf{k}) &= \gamma_s \mu_0 \left( H_{\text{bias}} + N_z(\mathbf{k}) M_s + J_{\text{ex}} \mathbf{k}^2 \right). \end{aligned} \quad (\text{V.1.13})$$

The magnon spectrum takes the form (cf. Eq. I.2.5)

$$\omega_{\mathbf{k}} = \sqrt{\omega_x(\mathbf{k}) \omega_z(\mathbf{k})}, \quad (\text{V.1.14})$$

and the damping can be found as  $\gamma_{\mathbf{k}} = \frac{\alpha}{2} [\omega_x(\mathbf{k}) + \omega_z(\mathbf{k})]$ . The two magnetisation components can be expressed in terms of a single mode amplitude  $\psi_{\mathbf{k}}$ , similarly to Eq. (I.2.8):

$$\boxed{m_x(\mathbf{k}) = \sqrt{\frac{\gamma_s M_s}{2d}} \sqrt{\frac{\omega_{\mathbf{k}}}{\omega_x(\mathbf{k})}} \psi_{\mathbf{k}}, \quad m_z(\mathbf{k}) = \mp i \sqrt{\frac{\gamma_s M_s}{2d}} \sqrt{\frac{\omega_{\mathbf{k}}}{\omega_z(\mathbf{k})}} \psi_{\mathbf{k}}.} \quad (\text{V.1.15})$$

<sup>1</sup> The quantity  $J_{\text{ex}}$  is linked to the exchange energy constant  $A_{\text{ex}}$  via  $J_{\text{ex}} = 2A_{\text{ex}}/M_s^2$ .

Note that we did not use the real part here, as the Fourier components  $m_{x,z}(\mathbf{k})$  are complex-valued. In the real space, one would write<sup>2</sup> a generic solution in the form

$$\begin{aligned} m_x(\mathbf{r}, t) &= \sqrt{\frac{\gamma_s M_s}{2d}} \operatorname{Re} \sum_{\mathbf{k}} \sqrt{\frac{\omega_{\mathbf{k}}}{\omega_x(\mathbf{k})}} \psi_{\mathbf{k}} e^{i\mathbf{k}\cdot\mathbf{r}-i\omega_{\mathbf{k}}t} , \\ m_z(\mathbf{r}, t) &= \pm \sqrt{\frac{\gamma_s M_s}{2d}} \operatorname{Im} \sum_{\mathbf{k}} \sqrt{\frac{\omega_{\mathbf{k}}}{\omega_z(\mathbf{k})}} \psi_{\mathbf{k}} e^{i\mathbf{k}\cdot\mathbf{r}-i\omega_{\mathbf{k}}t} . \end{aligned} \quad (\text{V.1.16})$$

The two frequencies  $\omega_x(\mathbf{k})$  and  $\omega_z(\mathbf{k})$  behave very differently. As  $N_z \mathbf{k} \rightarrow 0$ ) = 1,  $N_x(\mathbf{k} \rightarrow 0) = 0$ , the frequency  $\omega_z(\mathbf{k})$  depends upon  $\mathbf{k}$  rather weakly, while  $\omega_x(\mathbf{k})$  is almost negligible at  $k_x = 0$ , but quickly grows with  $k_x$ . This makes the ellipticity  $\sqrt{\omega_x(\mathbf{k})/\omega_z(\mathbf{k})}$  to grow with wavevector, changing from almost linear precession for long wavelengths to a nearly circular one at short wavelengths. Note also that the link between  $m_{x,z}$  and  $\psi_{\mathbf{k}}$  is non-local.

The theory presented here is approximate, and only works for  $|\mathbf{k}|d \lesssim 1$ . In this limit, it coincides with approximate expressions

$$\omega(k_x) = \gamma\mu_0 \sqrt{H_{\text{bias}}^2 + H_{\text{bias}}M_s + M_s^2 [1 - \exp(-2|k_x|d)]} \quad (\text{V.1.17})$$

for waves propagating along  $\hat{\mathbf{x}}$  (the Damon-Eshbach case) and

$$\omega(k_y) = \gamma\mu_0 \sqrt{H_{\text{bias}} \left[ H_{\text{bias}} + M_s \frac{1 - \exp(-|k_y|d)}{|k_y|d} \right]} \quad (\text{V.1.18})$$

for waves propagating along  $\hat{\mathbf{y}}$  (the backward-volume case). The two approximations work well for  $|\mathbf{k}|d \gg 1$ , however, they are not compatible with each other: the expression for the Damon-Eshbach case assumes that the magnetisation decays as  $\exp(|k_x|z)$  into the film, while the expression for the backward-volume waves assumes uniform magnetisation. Therefore, to analyse the waves at  $|\mathbf{k}|d \gtrsim 1$ , one has to solve the relevant equations directly, which can be easily done numerically. Since the dependence upon  $x$  and  $y$  is known, and only  $z$ -dependence is to be found, one may write the LLG equations in the form

$$\begin{aligned} -i\omega_{\mathbf{k}} m_x(z) &= \gamma_s \mu_0 \left[ H_{\text{bias}} + J_{\text{ex}} \mathbf{k}^2 - J_{\text{ex}} \frac{d^2}{dz^2} \right] m_z(z) + \gamma_s \mu_0 \frac{d\Phi_m}{dz} , \\ -i\omega_{\mathbf{k}} m_z(z) &= -\gamma_s \mu_0 \left[ H_{\text{bias}} + J_{\text{ex}} \mathbf{k}^2 - J_{\text{ex}} \frac{d^2}{dz^2} \right] m_x(z) - ik_x \gamma_s \mu_0 \Phi_m(z) , \end{aligned} \quad (\text{V.1.19})$$

$$\Phi_m(z) = \frac{1}{2|\mathbf{k}|} \int_{-d}^0 dz' e^{-|\mathbf{k}||z-z'|} \left[ ik_x m_x(z') + m_z \frac{d}{dz} \right] e^{-|\mathbf{k}||z-z'|} . \quad (\text{V.1.20})$$

One can discretise these equations in  $z$ , so that they take the form

$$\begin{aligned} -i\omega \mathbf{m} &= \hat{L} \mathbf{m} + \hat{P} \Phi , \\ \Phi &= \hat{Q} \mathbf{m} , \end{aligned} \quad (\text{V.1.21})$$

<sup>2</sup> To be fully rigorous, one should introduce two solutions to the LLG equations,  $\psi_{\mathbf{k}}$  with frequency  $\omega_{\mathbf{k}}$ , and  $\tilde{\psi}_{\mathbf{k}}$  with frequency  $-\omega_{\mathbf{k}}$ . To make the magnetisation components real-valued at arbitrary  $\mathbf{r}$  and  $t$ , one would then demand  $\tilde{\psi}_{\mathbf{k}} = \bar{\psi}_{-\mathbf{k}}$ . See also Sec. VI.1.

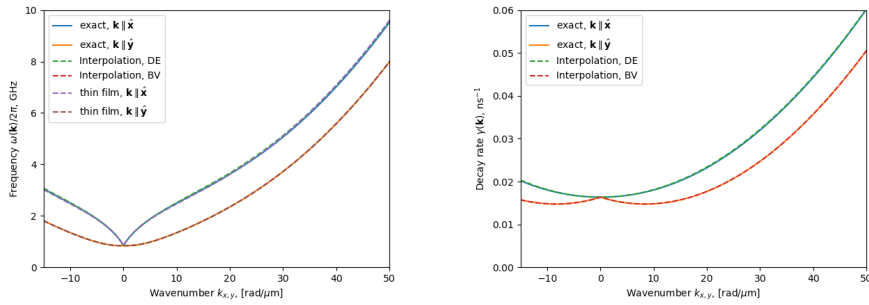


Figure V.2: The dispersion  $\omega_k$  and damping  $\gamma_k$  for a 50 nm thick YIG film ( $M_s = 140 \text{ kA/m}$ ), biased by  $B_{\text{ext}} = 5 \text{ mT}$ . The results are shown for both the Damon-Eshbach ( $\mathbf{k} \perp \mathbf{M}_s$ ) and backward-volume ( $\mathbf{k} \parallel \mathbf{M}_s$ ) geometries. Approximation (V.1.11) as well as Eqs. (V.1.17) and (V.1.18) are shown for comparison.

where  $\hat{L}$ ,  $\hat{P}$  and  $\hat{Q}$  are matrices operating on the discretised quantities. (For  $N$  discretisation points, the dimensions of the matrices are  $2N \times 2N$ ,  $2N \times N$ , and  $N \times 2N$ , respectively.) The variable  $\Phi$  can be easily eliminated, thus reducing the equations to an eigenvalue problem

$$-i\omega \mathbf{m} = [\hat{L} + \hat{P} \cdot \hat{Q}] \cdot \mathbf{m} \quad (\text{V.1.22})$$

with  $-i\omega_k$  being an eigenvalue. For modest frequencies ( $\omega/2\pi < 5 \text{ GHz}$ ) a relatively coarse discretisation, e.g. with  $N = 10$  is sufficient for most purposes. The respective eigenvectors are to be normalised by one magnon in the mode, as per Eq. (I.2.15), see also Sec. VI.1:

$$\int dz \bar{m}_x(z) m_z(z) = 2i\gamma_s M_s . \quad (\text{V.1.23})$$

The results of such analysis are shown in Fig. V.2. One can see that the approximation based on improved demagnetisation factors (V.1.11) gives a reasonable accuracy both in the dipole- and exchange-dominated regimes. The respective behaviour of  $|G_k(\omega)|$  is shown in Fig. V.3 for several values of frequency  $\omega$ . Directional dependencies of the wavenumber  $k_\omega(\theta)$  and group velocities  $u_\omega(\theta)$ ,  $v_\omega(\theta)$  are compared in Fig. V.4 and V.5 for approximation (V.1.11) and exact modes in the film. One can see that the approximate demagnetisation coefficients give approximately correct results not only at low frequencies, but also at high frequencies.

## V.2 Dipolar coupling between a thin film and a point Kittel dipole

Consider an isolated point-like Kittel dipole with magnetisation components  $\tilde{m}_{x,z}$ . The dipole is placed at the separation  $s$  from the surface, see Fig. V.6. We assume the same Damon-Eshbach geometry for the dipole: the magnetic precession occurs in the  $xz$  plane. Our task is to compute the energy of the coupling between spin waves in the film and the dipole. To this end, we need the magnetostatic potential

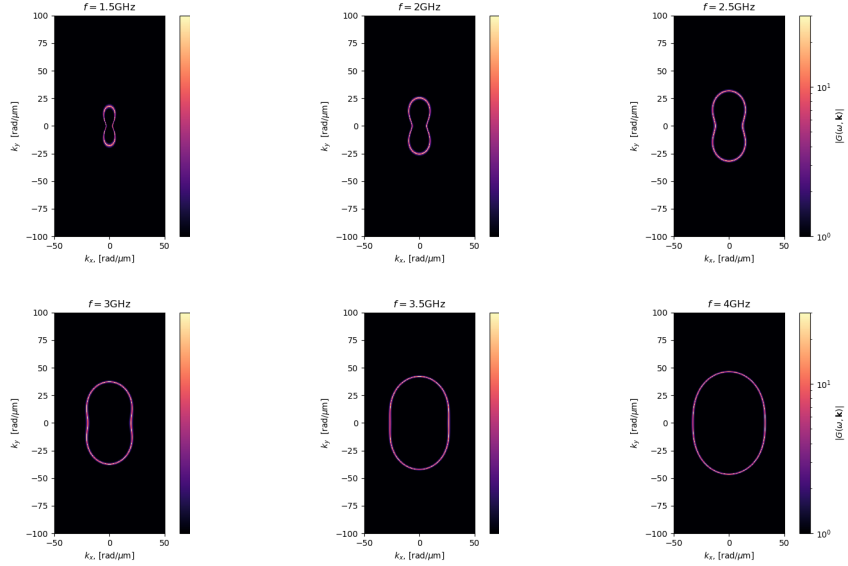


Figure V.3: Green's function maxima map out constant frequency contours for the dispersion in YIG. As the frequency is increased, strongly anisotropic contours of the dipolar regime cross over to more isotropic exchange-dominated contours.

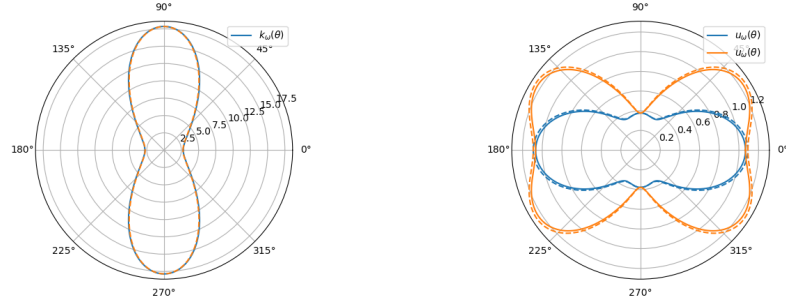


Figure V.4: Left: Directional dependence of  $k_\omega(\theta)$  for  $\omega/2\pi = 1.5 \text{ GHz}$ . Dashed line show the results with approximate demagnetisation factors (V.1.11). Right: the respective group velocities  $u_\omega(\theta)$  and  $v_\omega(\theta)$ .

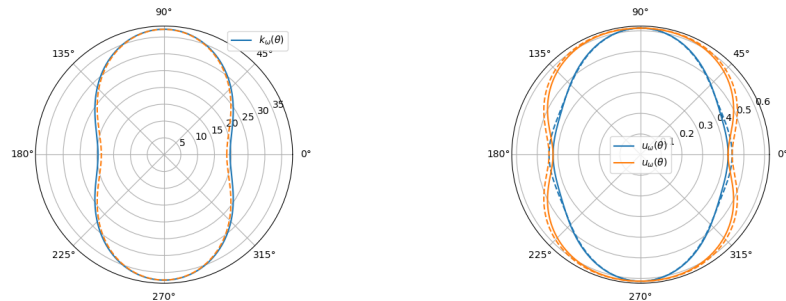


Figure V.5: Left: Directional dependence of  $k_\omega(\theta)$  for  $\omega/2\pi = 3 \text{ GHz}$ . Dashed line show the results with approximate demagnetisation factors (V.1.11). Right: the respective group velocities  $u_\omega(\theta)$  and  $v_\omega(\theta)$ .

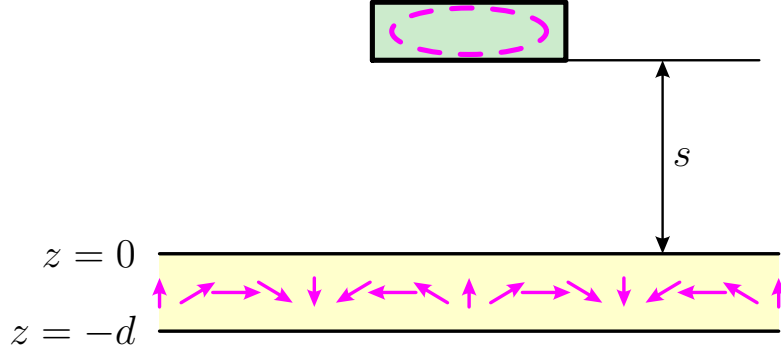


Figure V.6: A point-like Kittel dipole is placed at distance  $s$  from a film carrying spin waves.

induced above the film. The analysis given in the previous section yields

$$\Phi_{\text{out}}(z > 0; \mathbf{k}) = \frac{1}{2|\mathbf{k}|} e^{-|\mathbf{k}|z} [\rho_m d + \sigma_m |\mathbf{k}| d] = \frac{d}{2|\mathbf{k}|} e^{-|\mathbf{k}|z} [-ik_x m_x(\mathbf{k}) + |\mathbf{k}| m_z(\mathbf{k})]. \quad (\text{V.2.1})$$

One may also obtain a better form of this relation, applicable at  $|\mathbf{k}|d \sim 1$  by integrating the contributions to the potential over  $z$ :

$$\Phi_{\text{out}}(z > 0; \mathbf{k}) = \frac{1}{2|\mathbf{k}|^2} [1 - e^{-|\mathbf{k}|d}] e^{-|\mathbf{k}|z} [ik_x m_x(\mathbf{k}) + |\mathbf{k}| m_z(\mathbf{k})]. \quad (\text{V.2.2})$$

Expressing  $m_x(\mathbf{k})$  and  $m_z(\mathbf{k})$  via  $\psi_{\mathbf{k}}$ , we use Eq. (V.1.15) to write

$$\boxed{\Phi_{\text{out}}(z; \mathbf{k}) = -i\sqrt{\frac{d\gamma_s M_s \omega_{\mathbf{k}}}{2}} \frac{1}{|\mathbf{k}|} e^{-z|\mathbf{k}|} \left[ \frac{k_x}{\sqrt{\omega_x(\mathbf{k})}} + \frac{|\mathbf{k}|}{\sqrt{\omega_z(\mathbf{k})}} \right] \psi_{\mathbf{k}}.} \quad (\text{V.2.3})$$

Let us also give the relevant expression in the real space:

$$\Phi_{\text{out}}(\mathbf{r}, t) = \text{Im} \sum_{\mathbf{k}} \sqrt{\frac{d\gamma_s M_s \omega_{\mathbf{k}}}{8}} \frac{1}{|\mathbf{k}|} e^{-|\mathbf{k}|z} \left[ \frac{k_x}{\sqrt{\omega_x(\mathbf{k})}} + \frac{|\mathbf{k}|}{\sqrt{\omega_z(\mathbf{k})}} \right] \psi_{\mathbf{k}}(t) e^{i\mathbf{k}\cdot\mathbf{r} - i\omega_{\mathbf{k}}t}. \quad (\text{V.2.4})$$

Note that the full solution therefore includes the contributions proportional to  $\psi_{\mathbf{k}}$  and  $\bar{\psi}_{\mathbf{k}}$ , involving harmonics with wavevectors  $\mathbf{k}$  and  $-\mathbf{k}$ , respectively.

Once the stray magnetic field of the spin wave is known, we can compute the coupling energy. Let the dipole be described by a local variable  $\varphi(t)$ . According to Sec. I.2, the magnetisation components are given by (cf. Eq. I.2.8)

$$\tilde{m}_x(t) = \sqrt{\frac{2\tilde{\gamma}_s \tilde{M}_s \Omega_0}{V}} \frac{\text{Re } \varphi(t)}{\sqrt{\tilde{\Omega}_x}}, \quad \tilde{m}_z(t) = \sqrt{\frac{2\tilde{\gamma}_s \tilde{M}_s \Omega_0}{V}} \frac{\text{Im } \varphi(t)}{\sqrt{\tilde{\Omega}_z}}, \quad (\text{V.2.5})$$

Here and below the quantities with tilde refer to the resonator. One can then compute the energy of the dipole  $\tilde{\mathbf{m}}$  in the field  $\mathbf{H}$ :

$$E_{\text{coupling}} = - \int_V \tilde{\mathbf{m}} \cdot \mathbf{H} dV = \mu_0 V \tilde{\mathbf{m}} \cdot \nabla \Phi_m(x = y = 0, s), \quad (\text{V.2.6})$$

integrating over the volume  $V$  of the resonator. Since the potential is a plane wave in the  $xy$ -plane and an evanescent wave along  $z$ , one may write  $\nabla\Phi_{\text{out}} = (ik_x, ik_y, -|\mathbf{k}|)\Phi_{\text{out}}$  for the contribution proportional to  $\psi_{\mathbf{k}}$  and

$$\nabla\bar{\Phi}_m = (-ik_x, -ik_y, -\mathbf{k})\bar{\Phi}_m \quad (\text{V.2.7})$$

for the contribution of the mode  $\bar{\psi}_{\mathbf{k}}$ . Retaining only the resonant terms  $\propto \varphi\bar{\psi}_{\mathbf{k}}$  and its complex-conjugate, one finds

$$\begin{aligned} E_{\text{coupling}} = & -\frac{\mu_0\varphi\bar{\psi}_{\mathbf{k}}}{4}\sqrt{\gamma_s M_s \tilde{\gamma}_s \tilde{M}_s V d} \sqrt{\Omega_0 \omega_{\mathbf{k}}} \frac{1}{|\mathbf{k}|} e^{-s|\mathbf{k}|} \times \\ & \times \left[ \frac{k_x}{\sqrt{\omega_x(\mathbf{k})}} + \frac{|\mathbf{k}|}{\sqrt{\omega_z(\mathbf{k})}} \right] \left[ \frac{k_x}{\sqrt{\tilde{\Omega}_x}} - \frac{|\mathbf{k}|}{\sqrt{\tilde{\Omega}_z}} \right] + \text{c.c.} + \text{non-resonant}. \end{aligned} \quad (\text{V.2.8})$$

Here  $s$  is the spacing between the resonator and the film. Thus, we obtain an expression for the hybridisation:

$$\boxed{\Delta_{\mathbf{k}}^{(\text{DE})} = -\frac{\mu_0}{4}\sqrt{\gamma_s M_s \tilde{\gamma}_s \tilde{M}_s V d} \sqrt{\Omega_0 \omega_{\mathbf{k}}} \frac{1}{|\mathbf{k}|} e^{-s|\mathbf{k}|} \times \left[ \frac{k_x}{\sqrt{\omega_x(\mathbf{k})}} + \frac{|\mathbf{k}|}{\sqrt{\omega_z(\mathbf{k})}} \right] \left[ \frac{k_x}{\sqrt{\tilde{\Omega}_x}} - \frac{|\mathbf{k}|}{\sqrt{\tilde{\Omega}_z}} \right].} \quad (\text{V.2.9a})$$

It can be also rewritten in a slightly different form, to emphasize the role of ellipticities  $\epsilon_{xz}(\mathbf{k}) = \sqrt{\omega_x(\mathbf{k})/\omega_z(\mathbf{k})}$  of the wave and  $\tilde{e}_{xz} = \sqrt{\Omega_x/\Omega_z}$  of the resonator:

$$\begin{aligned} \Delta_{\mathbf{k}}^{(\text{DE})} = & -\frac{\mu_0}{4}\sqrt{\gamma_s M_s \tilde{\gamma}_s \tilde{M}_s V d} \frac{1}{|\mathbf{k}|} e^{-s|\mathbf{k}|} \times \\ & \times \left[ \frac{k_x}{\sqrt{\epsilon_{xz}(\mathbf{k})}} + |\mathbf{k}| \sqrt{\epsilon_{xz}(\mathbf{k})} \right] \left[ \frac{k_x}{\sqrt{\tilde{e}_{xz}}} - |\mathbf{k}| \sqrt{\tilde{e}_{xz}} \right]. \end{aligned} \quad (\text{V.2.10})$$

We see that the coupling to the film and the resonator in the Damon-Eshbach geometry involves two chirality factors. They have a similar structure, but their properties may be rather different due to the demagnetisation coefficients, and also the sign of the two terms are opposite<sup>3</sup>. For a chiral resonator,  $\tilde{\Omega}_x \approx \tilde{\Omega}_z$  the chirality factor  $\propto (k_x - |\mathbf{k}|)$  suppresses forward scattering and favours backward scattering. For a thin film,  $\omega_x(\mathbf{k}) \ll \omega_z(\mathbf{k})$ , the respective chirality factor  $\propto k_x$  favours forward and backward scattering ( $k_x \approx |\mathbf{k}|$ ) and suppresses sideways scattering ( $k_x \ll |\mathbf{k}|$ ). Note that the sign in the two chirality factors depend upon the handedness of precession in the resonator and in the film. If one of the two is reversed, so does the sign in the respective chiral factor.

One may also consider backward-volume orientation of the resonator. This would result in the coupling

$$\Delta_{\mathbf{k}}^{(\text{BV})} = [\dots] \left[ \frac{k_y}{\sqrt{\omega_x(\mathbf{k})}} + \frac{|\mathbf{k}|}{\sqrt{\omega_z(\mathbf{k})}} \right] \left[ \frac{k_y}{\sqrt{\tilde{\Omega}_y}} - \frac{|\mathbf{k}|}{\sqrt{\tilde{\Omega}_z}} \right]. \quad (\text{V.2.11})$$

<sup>3</sup> At first glance, different signs may seem counterintuitive. To explain this, one may notice that the sign in the chirality factor depends on whether the film is above or below the resonator. The stray field emanating above the film is  $\propto (k_x + \epsilon_{xz}|\mathbf{k}|)$ , while the field induced by the resonator with the same handedness of precession in the film is  $\propto (k_x - \tilde{e}_{xz}|\mathbf{k}|)$  because the film is below the resonator. Reciprocity therefore demands the overall coupling to be proportional to the factors with opposite signs.

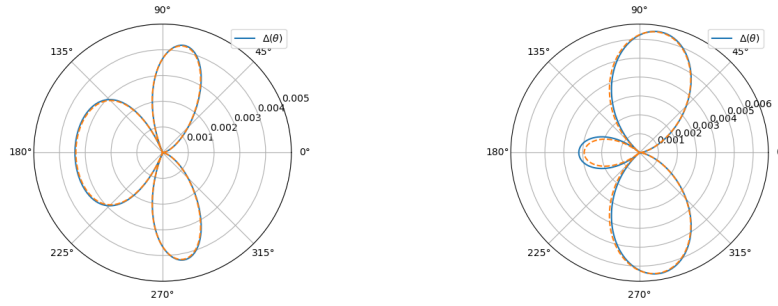


Figure V.7: Coupling  $\Delta_\theta$  between a point Kittel dipole with  $N_x = N_z = 1/2$ ,  $\mathbf{M}_s \parallel \hat{\mathbf{y}}$  and the modes of a 50 nm YIG film. Left panel:  $f = 1.5$  GHz (dipolar regime). Right panel:  $f = 3$  GHz (both exchange and dipolar interactions are important). Approximation (V.1.11) is shown for comparison as dashed lines.

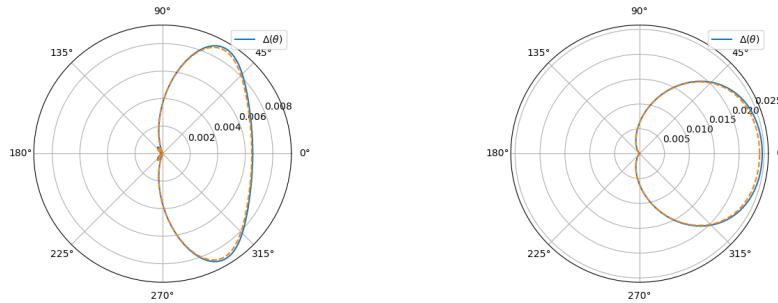


Figure V.8: Coupling  $\Delta_\theta$  between a point Kittel dipole with  $N_x = N_z = 1/2$ ,  $\mathbf{M}_s \parallel -\hat{\mathbf{y}}$  and the modes of a 50 nm YIG film. The left and right panel show the coupling in the two regimes,  $f = 1.5$  GHz (dipolar). and  $f = 3$  GHz (exchange and dipolar).

with the same dependence upon the material constants, but with different chiral factor for the resonator. Obviously, this results in a different angular dependence: for a chiral resonator, this would suppress emission in the negative- $y$  direction.

To illustrate the resulting angular dependencies, we have computed  $\Delta_\theta$  for a point Kittel dipole with  $N_x = N_y = 1/2$  coupled to the YIG film analysed above. The results are shown in Fig. V.7. If the magnetisation of the resonator is parallel to that of the film, the scattering at low frequencies exhibits three zeros: at nearly vertical directions, and in the forward direction. The “vertical” zeros originate from the chiral factors of the film, in which  $\omega_x(\mathbf{k}) \ll \omega_z(\mathbf{k})$ , and the precession is highly elliptical. The suppression of the forward coupling is due to the chirality of the resonator with circular free precession. At higher frequencies, however, the dynamics of the modes in the film is due to the exchange interaction, which makes the precession in the film circular. As a result, the chirality factor of the film partially suppresses backward scattering, which results in a pattern with perpendicular directivity. When the magnetisation in the resonator is reversed, the handedness of its precession is opposite to that in the film, and this strongly affects the directivity of the coupling, as shown in Fig. V.8, with the scattering strongly suppressed in the backward direction.

For a resonator in which magnetisation is oriented along  $\mathbf{x}$ , the situation is different, see Fig. V.9. A nearly upward peak at low frequencies, where the coupling is proportional to  $k_y$ , is transformed into a diagonal peak at higher frequencies,

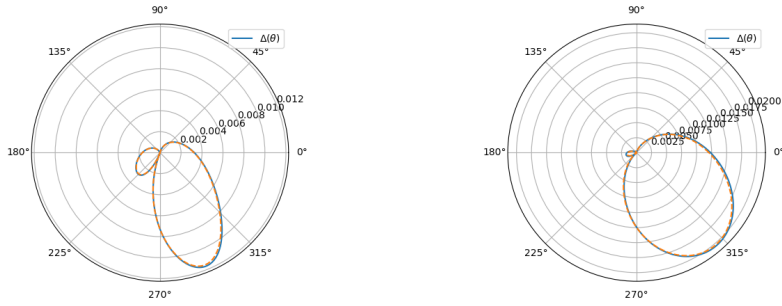


Figure V.9: Coupling  $\Delta_\theta$  between a point Kittel dipole with  $N_x = N_z = 1/2$ ,  $\mathbf{M}_s \parallel \hat{\mathbf{x}}$  and the modes of a 50 nm YIG film. Left panel:  $f = 1.5$  GHz (dipolar regime). Right panel:  $f = 3$  GHz (both exchange and dipolar interactions are important). Approximation (V.1.11) is shown for comparison as dashed lines.

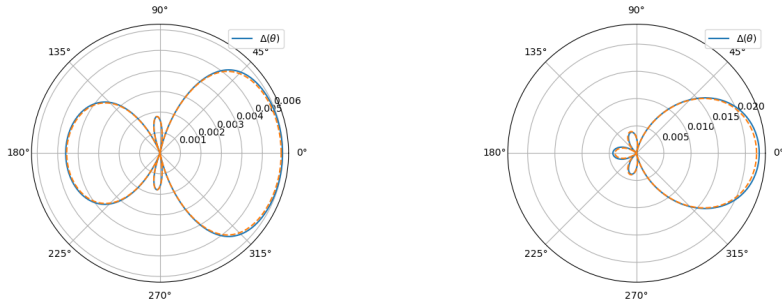


Figure V.10: Coupling  $\Delta_\theta$  between a point Kittel dipole with  $N_x = 0.01$ ,  $N_z = 0.99$ , with  $\mathbf{M}_s \parallel \hat{\mathbf{y}}$  and the modes of a 50 nm YIG film. Left panel:  $f = 1.5$  GHz (dipolar regime). Right panel:  $f = 3$  GHz (both exchange and dipolar interactions are important). Approximation (V.1.11) is shown for comparison as dashed lines.

with the coupling proportional to  $k_y + |\mathbf{k}|$ .

For “non-chiral” dipoles, with  $N_x \ll N_z$ , one obtains rather different distributions shown in Figs. V.10, V.11 and V.12. In the low-frequency regime, the two chirality factors  $\sim k_x$  favour forward and backward scattering for  $\mathbf{M}_s \parallel \hat{\mathbf{y}}$ , while the scattering in the perpendicular direction is suppressed. There is an approximate symmetry between forward and backward scattering, as the two chirality factors work in opposite directions. When the dipole is reversed, forward scattering is favoured over backward scattering, as dictated by the two chirality factors now working in sync. A dipole oriented along  $\hat{\mathbf{x}}$  emits the scattered waves along  $\hat{\mathbf{y}}$ , with comparable upward- and downward-going intensities. At higher frequencies, backscattering peak is suppressed in the aligned geometry, due to the chirality of the film, and this is also true for reverse alignment. In the case of perpendicular alignment, the distribution evolves into two forward-going diagonal peaks.

Let us also give an estimate for the strength of the coupling and its contribution to  $\Gamma_{\text{rad}}(\omega)$ . For simplicity, let us assume  $\gamma_s = \tilde{\gamma}_s$ ,  $\omega_x(\mathbf{k}) \sim \omega_z(\mathbf{k}) \sim \omega(\mathbf{k})$ ,  $\tilde{\Omega}_x(\mathbf{k}) \sim \tilde{\Omega}_z(\mathbf{k}) \sim \tilde{\Omega}_0(\mathbf{k})$ . One then finds

$$\Delta_\theta \sim \mu_0 \gamma_s \sqrt{M_s \tilde{M}_s V d} |\mathbf{k}| e^{-h|\mathbf{k}|} \sin^2 \frac{\theta}{2}. \quad (\text{V.2.12})$$

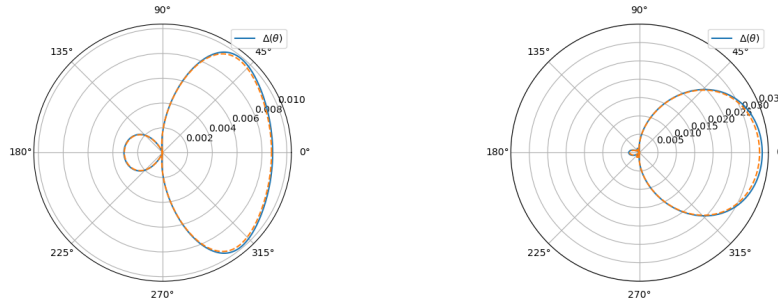


Figure V.11: Coupling  $\Delta_\theta$  between a point Kittel dipole with  $N_x = 0.01$ ,  $N_z = 0.99$ , with  $\mathbf{M}_s \parallel -\hat{\mathbf{y}}$  and the modes of a 50 nm YIG film. Left panel:  $f = 1.5$  GHz (dipolar regime). Right panel:  $f = 3$  GHz (both exchange and dipolar interactions are important). Approximation (V.1.11) is shown for comparison as dashed lines.

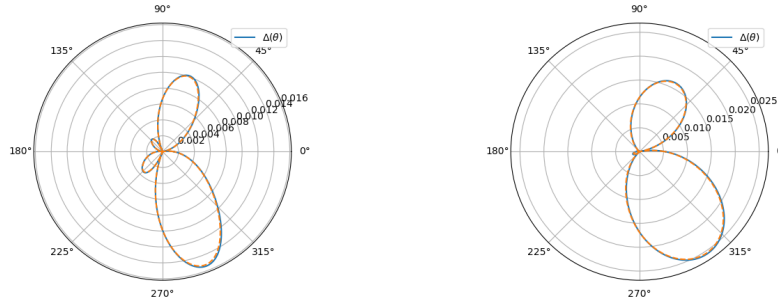


Figure V.12: Coupling  $\Delta_\theta$  between a point Kittel dipole with  $N_x = 0.01$ ,  $N_z = 0.99$ , with  $\mathbf{M}_s \parallel \hat{\mathbf{x}}$  and the modes of a 50 nm YIG film. Left panel:  $f = 1.5$  GHz (dipolar regime). Right panel:  $f = 3$  GHz (both exchange and dipolar interactions are important). Approximation (V.1.11) is shown for comparison as dashed lines.

Then, one can write for the radiative linewidth

$$\Gamma_{\text{rad}}(\omega) \sim \frac{1}{2} \frac{k_\omega |\Delta_\theta|^2}{2u_\omega} = \frac{3}{16} \frac{\mu_0^2 \gamma_s^2 M_s \tilde{M}_s k_\omega^3 V d}{u_\omega} = \frac{3}{16} \mu_0 \gamma_s M_s \frac{\mu_0 \gamma_s \tilde{M}_s}{u_\omega} k_\omega^3 V d e^{-2k_\omega s}. \quad (\text{V.2.13})$$

The factors  $\mu_0 \gamma_s M_s$  and  $\mu_0 \gamma_s \tilde{M}_s$  are of the order of  $\Omega_0$  or even larger. Thus, one finds an order-of-magnitude estimate

$$\boxed{\Gamma_{\text{rad}} \sim \Omega_0 e^{-2k_\omega s} (k_\omega W)(k_\omega L)(k_\omega H)(k_\omega d)}. \quad (\text{V.2.14})$$

The theory presented here assumes that the radiative linewidth is smaller than  $\Omega_0$ , so that the resonances are not quenched and well-defined. We see that the coupling can be suppressed for two reasons. First, each of the dimensions (resonator width  $W$ , its length  $L$  and height  $H$ , as well as the film thickness  $d$ ) enter the coupling via the factor  $k_\omega a$ . Second, the coupling is suppressed due to spacing  $h$  between the film and the resonator as  $\exp(-2k_\omega s)$ . However, for  $k_\omega \sim 20$  rad/ $\mu\text{m}$ ,  $W \sim L \sim 300$  nm,  $H \sim h \sim 20$  nm these suppression factors are unimportant, and the coupling may in fact quench the resonant modes. One should bear in mind, nevertheless, that in artificial antiferromagnets the coupling may be weakened due to the compensation between individual magnetisations of the two materials.

The estimate of  $\Gamma_{\text{rad}}$  can be also employed to obtain the field concentration factor. Consider a wave of amplitude  $m_x \sim m_z \sim m_{\text{inc}}$  in the film. What is the magnetisation induced in the resonator? To this end, we use the relation (I.2.8) between  $\varphi(t)$  and  $m_{x,z}(t)$  in the resonator, which yields

$$m_{\text{res}} \sim \sqrt{\frac{\tilde{\gamma}_s \tilde{M}_s}{V}} \varphi . \quad (\text{V.2.15})$$

(For simplicity, we ignore the ellipticity factors here.) Similarly, Eq. (V.1.15) yields for the incident wave:

$$m_{\text{inc}} \sim \sqrt{\frac{\gamma_s M_s}{d}} \psi_{\text{inc}} . \quad (\text{V.2.16})$$

The relation between  $\psi_{\text{inc}}$  and  $\varphi$  is given by Eq. (IV.5.2):

$$\varphi \sim \frac{\Delta}{\Gamma_{\text{res}}} \psi_{\text{inc}} . \quad (\text{V.2.17})$$

In two dimensions,  $\Gamma_{\text{rad}} \sim |\Delta|^2 k_\omega / v_\omega$ . Rewriting the above relation in terms of  $\Gamma_{\text{rad}}$  and assuming that  $\Gamma_{\text{rad}} \gtrsim \Gamma_0$ , one finds

$$\varphi \sim \sqrt{\frac{v_\omega}{\Gamma_{\text{rad}} k_\omega}} \psi_{\text{inc}} . \quad (\text{V.2.18})$$

Collecting all these relations together, one finds the field concentration factor

$$\frac{m_{\text{res}}}{m_{\text{inc}}} \sim \sqrt{\frac{\tilde{\gamma}_s \tilde{M}_s}{\gamma_s M_s}} \sqrt{\frac{d}{WLH}} \sqrt{\frac{v_\omega}{\Gamma_{\text{rad}} k_\omega}} .$$

(V.2.19)

One may make further simplifying assumptions: if the factors  $\gamma_s M_s$  are the same for both materials,  $k_\omega \sim \Omega_0 / v_\omega$ , and  $v_\omega \sim \omega_M d$ , with  $\omega_M = \gamma_s \mu_0 M_s$ , one can transform Eq. (V.2.19) to the form

$$\frac{m_{\text{res}}}{m_{\text{inc}}} \sim \left( \frac{d^3}{WLH} \frac{\omega_M^2}{\Omega_0 \Gamma_{\text{rad}}} \right)^{1/2} . \quad (\text{V.2.20})$$

This relation demonstrates that one can achieve rather high field concentration by using narrow resonant modes, and a strong coupling between the resonator and the film may be in fact undesirable. However, this analysis assumed that the dissipative linewidth  $\Gamma_0$  is negligible, otherwise the result would be suppressed by the factor  $\Gamma_0 / (\Gamma_{\text{rad}} + \Gamma_0)$ . This suggests that the maximal field concentration is achieved when  $\Gamma_{\text{rad}} \sim \Gamma_0$ .

For one-dimensional scattering, the calculation differs only in one aspect:  $\Gamma_{\text{rad}} \sim |\Delta|^2 / v_\omega$ , so that

$$\frac{m_{\text{res}}}{m_{\text{inc}}} \sim \left( \frac{\tilde{\gamma}_s \tilde{M}_s}{\gamma_s M_s} \frac{d}{LH} \frac{v_\omega}{\Gamma_{\text{rad}}} \right)^{1/2} \sim \left( \frac{d^2}{LH} \frac{\omega_M}{\Gamma_{\text{rad}}} \right)^{1/2} , \quad (\text{V.2.21})$$

and the conclusions of the previous paragraph remain valid.

Finally, we analyse frequency dependence of the radiative rate which is given by

$$\Gamma_{\text{rad}}(\omega) \propto \frac{k_\omega^3}{u_\omega} \exp(-2sk_\omega) . \quad (\text{V.2.22})$$

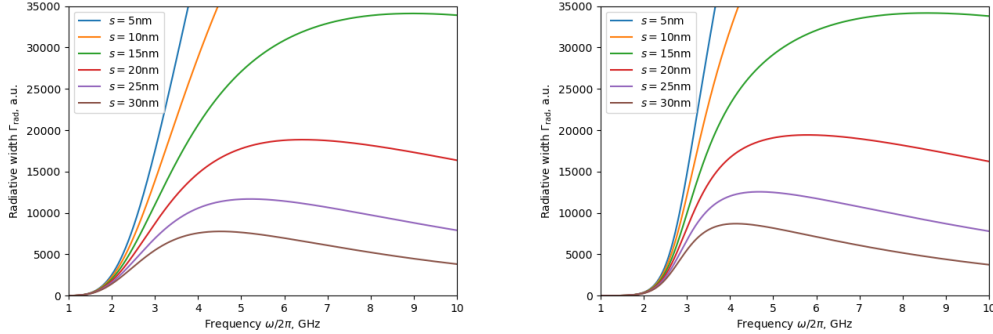


Figure V.13: Frequency dependence of the emission rate for  $d = 20$  nm (left panel) and  $d = 50$  nm (right panel). Different curves correspond to different values of the spacing  $s$ .

This quantity is plotted in Fig. V.13 for two film thicknesses, 20 nm and 50 nm and several spacings  $s$ . One can see that for  $s < 15$  nm the emission rate for a point dipole increases monotonically at all frequencies  $< 10$  GHz. When the spacing is made larger, the coupling at high frequencies is suppressed by the exponential decay.

### V.3 The off-resonant coupling

The calculation of the previous section also yields off-resonant couplings of the form  $\Delta'_{\mathbf{k}} \varphi \psi_{\mathbf{k}}$ . Extracting the relevant term, one finds for the Damon-Eshbach orientation:

$$\begin{aligned} \Delta'_{\mathbf{k}, \text{DE}} &= \frac{\mu_0}{4} \sqrt{\gamma_s M_s \tilde{\gamma}_s \tilde{M}_s V d} \frac{1}{|\mathbf{k}|} e^{-h|\mathbf{k}|} \\ &\times \left[ \frac{k_x}{\sqrt{\epsilon_{xz}(\mathbf{k})}} + |\mathbf{k}| \sqrt{\epsilon_{xz}(\mathbf{k})} \right] \left[ \frac{k_x}{\sqrt{\tilde{\epsilon}_{xz}}} + |\mathbf{k}| \sqrt{\tilde{\epsilon}_{xz}} \right]. \end{aligned} \quad (\text{V.3.1})$$

Here, all the quantities have the same meaning as in Eq. V.2.10. The primary difference is the sign of horizontal wavevector components in the chirality factors.

### V.4 Scattering of thin-film modes by large resonators.

The results of the previous section can be generalised to the case of large resonators if the respective magnon modes are well-resolved. Let  $\mathbf{m}^{(\nu)}(\mathbf{r})$  be the mode in the resonator. We assume it to be normalised by one magnon, as per Eq. (I.2.15). Then, the hybridisation can be written in the form

$$\begin{aligned} \Delta_{\mathbf{k}}^{(\nu)} &= -\frac{\mu_0}{4} \sqrt{\gamma_s M_s \omega_k d} \frac{1}{|\mathbf{k}|} e^{-h|\mathbf{k}|} \left[ \frac{k_x}{\sqrt{\omega_x(\mathbf{k})}} + \frac{|\mathbf{k}|}{\sqrt{\omega_z(\mathbf{k})}} \right] \\ &\times \int_V d^3 \mathbf{r} e^{-|\mathbf{k}|(z-h)-i\mathbf{k}\cdot\mathbf{r}} [k_x m_x^{(\nu)}(\mathbf{r}) + k_y m_y^{(\nu)}(\mathbf{r}) - i|\mathbf{k}| m_z^{(\nu)}(\mathbf{r})]. \end{aligned} \quad (\text{V.4.1})$$

For uniform modes,

$$m_x^{(\text{uni})} \approx \sqrt{\frac{2\tilde{\gamma}_s \tilde{M}_s \Omega_\nu}{V}} \frac{1}{\sqrt{\tilde{\Omega}_x}}, \quad m_z^{(\text{uni})} \approx -i\sqrt{\frac{2\tilde{\gamma}_s \tilde{M}_s \Omega_\nu}{V}} \frac{1}{\sqrt{\tilde{\Omega}_z}}, \quad (\text{V.4.2})$$

and negligible size of the resonator, this of course can be reduced to the expression above. If the mode is uniform, but the resonator is sufficiently large, one should also introduce the formfactor

$$\mathcal{F}(\mathbf{k}) = \frac{1}{V} \int_V d^3 \mathbf{r} e^{-i\mathbf{k} \cdot \mathbf{r} - |\mathbf{k}|(z-h)}, \quad (\text{V.4.3})$$

so that the coupling  $\Delta_{\mathbf{k}}$  for a large resonator can be obtained from its value  $\Delta_{\mathbf{k}}^{(\text{point})}$  for a point-like resonator via

$$\Delta_{\mathbf{k}} = \Delta_{\mathbf{k}}^{(\text{point})} \mathcal{F}(\mathbf{k}). \quad (\text{V.4.4})$$

E.g., for a thin rectangular bar of length  $L$  along  $x$ , width  $W$  along  $y$  and height  $H$  along  $z$ , one finds the formfactor

$$\mathcal{F}(\mathbf{k}) \approx \frac{2 \sin \frac{k_x L}{2}}{k_x L} \times \frac{2 \sin \frac{k_y W}{2}}{k_y W} \times \frac{1 - e^{-H|\mathbf{k}|}}{H|\mathbf{k}|}. \quad (\text{V.4.5})$$

The oscillating  $k_y$ -dependent factor here describes the Fraunhofer diffraction off a rectangular slit of width  $W$ . This may further collimate the scattering to  $|k_y|W < 2\pi$ . This effect suppresses the coupling  $\Delta_{\mathbf{k}}$  and the radiative linewidth  $\Gamma_{\text{rad}}(\omega)$  for resonator dimensions comparable with the wavelength or larger.

When the film thickness is not negligible, one may use modes normalised by one magnon as per Eq. (I.2.15). Then, the potential above the film can be found as

$$\Phi_m(z; \mathbf{k}) = \Phi_m(0; \mathbf{k}) e^{-|\mathbf{k}|z}, \quad (\text{V.4.6})$$

where  $\Phi_m(0; \mathbf{k})$  is the potential at the outer surface. E.g., in the uniform-mode approximation used above,

$$\Phi_m^{(\text{uni})}(0; \mathbf{k}) \approx i \sqrt{\frac{1}{2} \gamma_s M_s \omega_{\mathbf{k}}} \frac{1}{|\mathbf{k}|} \left[ \frac{k_x}{\sqrt{\omega_x(\mathbf{k})}} + \frac{|\mathbf{k}|}{\sqrt{\omega_z(\mathbf{k})}} \right]. \quad (\text{V.4.7})$$

The coupling is then given by

$$\Delta_{\mathbf{k}}^{(\nu)} = \frac{\mu_0}{4} e^{-s|\mathbf{k}|} \bar{\Phi}_m(0; \mathbf{k}) \left[ ik_x \mathcal{M}_x^{(\nu)}(\mathbf{k}) + ik_y \mathcal{M}_y^{(\nu)}(\mathbf{k}) + |\mathbf{k}| \mathcal{M}_z^{(\nu)}(\mathbf{k}) \right], \quad (\text{V.4.8})$$

with magnetic formfactors

$$\mathcal{M}_{x,y,z}^{(\nu)}(\mathbf{k}) \equiv \int_V dx dy dz' e^{-|\mathbf{k}|z' - ik_x x - ik_y y} m_{x,y,z}^{(\nu)}(x, y, z'). \quad (\text{V.4.9})$$

Here the coordinate  $z'$  is measured from the bottom point of the resonator,  $z' = z - s$ , so that the formfactors are independent of  $s$ .

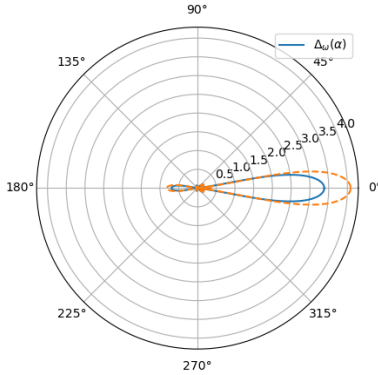


Figure V.14: Hybridisation coupling for a finite-size resonator,  $s = 10 \text{ nm}$ . The dashed line shows the same quantity computed for a thin film. The relatively large disagreement is due to suppression of the coupling under the full-wave condition, which makes the overall magnitude of the coupling rather sensitive to the details of the dispersion.

It is instructive to see how the one-dimensional limit is recovered when the resonator is sufficiently wide. The transverse dependence of the coupling  $\Delta(\theta)$  is then given by the sync function. Thus, one may write for  $\theta \approx 0$  or  $\theta \approx \pi$ :

$$\Delta(\theta \approx 0) = \Delta_{\text{fw}} \sqrt{W} \frac{\sin^{1/2} k_\omega \theta W}{1/2 k_\omega \theta W}, \quad (\text{V.4.10})$$

$$\Delta(\theta \approx \pi) = \Delta_{\text{bk}} \sqrt{W} \frac{2 \sin k_\omega \theta W / 2}{1/2 k_\omega \theta W}, \quad (\text{V.4.11})$$

where the constants  $\Delta_{\text{fw}}$  and  $\Delta_{\text{bk}}$  take care of the mode profile in the  $xz$  plane:

$$\Delta_{\text{fw,bk}} = \frac{\mu_0 k_\omega}{4} e^{-sk_\omega} \Phi_m(0; \pm k_\omega, 0) \int_V dx dz' [\pm i m_x(x, z') + m_z(x, z')] e^{-k_\omega z' \pm ik_\omega x}. \quad (\text{V.4.12})$$

The factors  $\sqrt{W}$  arise from normalising the modes. Then, the contributions of small forward-going angles to the radiative linewidths are

$$\begin{aligned} \Gamma_{\text{fw}} &= \frac{1}{4\pi} \int d\theta \frac{k_\omega(0)}{u_\omega(\theta)} |\Delta_\theta|^2 \\ &= \frac{k_\omega(0) |\Delta_{\text{fw}}|^2}{4\pi u_\omega(0)} \times \frac{4}{k_\omega^2(0) W} \int_{-\infty}^{\infty} \frac{\sin^2(1/2 k_\omega W \theta)}{\theta^2} d\theta, \end{aligned} \quad (\text{V.4.13})$$

where we extended the limits of integration to infinity, since the primary contribution comes from small angles  $\theta \sim (k_\omega W)^{-1} \ll 1$ . Using the well-known value for the integral,

$$\int_{-\infty}^{\infty} \frac{\sin^2 ax dx}{x^2} = \pi a, \quad (\text{V.4.14})$$

one finds

$$\Gamma_{\text{fw}} = \frac{|\Delta_{\text{fw}}|^2}{2u_\omega(0)}, \quad (\text{V.4.15})$$

which coincides with the expression from one-dimensional theory. The backward-going contribution acquires a similar form. Thus, the one-dimensional radiative

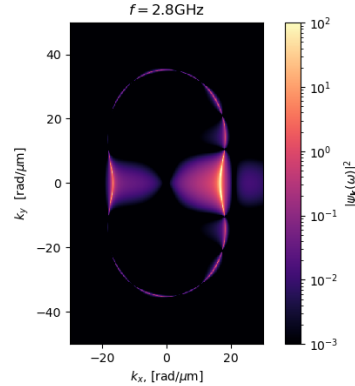


Figure V.15: Intensity of the scattered wave in the  $\mathbf{k}$ -space for a finite-size resonator,  $s = 10$  nm.

rates are equal to inclusive two-dimensional rates that include contributions of all the relevant transverse channels. Nearby, at distances  $|x| < W^2 k_\omega^2$ , the scattered forward and backward beams are indistinguishable from one-dimensional waves of nearly constant amplitudes that can be determined by ignoring transverse wavenumber  $k_y$  completely. The forward-going beam at these distances interferes with the incident beam, and the formula for one-dimensional transmission applies:

$$T = 1 - \frac{2i\Delta_{\text{fw}}}{u_\omega(0)} \frac{\varphi}{A_{\text{inc}}} . \quad (\text{V.4.16})$$

At larger distances, however, the beams diverge, and two-dimensional waves with amplitudes decaying as  $1/\sqrt{r}$  are formed.

We used the results of this section to analyse scattering by a non-chiral resonator of finite size tuned to  $f = 2.81$  GHz. The dimensions  $L \times W \times s$  of the resonator were chosen to be  $300\text{nm} \times 600\text{nm} \times 40\text{nm}$  to approximately match those used in micromagnetic simulations. The desired resonant frequency is obtained for  $N_x = 0.005$  and  $M_s = 800$  kA/m. We considered two values of the spacing  $s$ : 10 nm and 20 nm. The coupling  $\Delta_\theta$  computed from exact modes in the film and for a uniform mode in the resonator is shown in Fig. V.14 for the resonant frequency. It exhibits a narrow forward peak, which is primarily due to the formfactor  $F(k_y)$  that describes the Fraunhofer diffraction in the transverse direction. There is also a weaker backward-scattering peak. Suppression of this peak, relative to the forward peak can be attributed to the chirality of the film modes at such high frequencies. These features we discussed can be also seen in the distribution of the scattered wave  $|\psi_{\mathbf{k}}|$  in the  $\mathbf{k}$ -space shown in Fig. V.15.

The radiative linewidth computed from exact modes in the film and uniform modes in the resonator is shown in Fig. V.16. While  $\Gamma_{\text{rad}}(\omega)$  increases at small frequencies, it becomes suppressed at higher frequencies. This can be attributed to the following. In the vicinity of the desired resonant frequency, the wavenumber for the Damon-Eshbach modes is approximately  $k_x \approx 16\mu\text{m}^{-1}$ , which gives wavelength of  $\approx 390$  nm. Therefore, had the resonator been that wide, it would be equivalent to a full-wave dipole antenna, which is a rather inefficient radiator. As the frequency is increased, the full-wave condition is approached rather quickly: the wavelength is equal to  $L = 300$  nm for  $k = 21\mu\text{m}^{-1}$  which is achieved at  $\approx 3.4$  GHz. Away from this point, however, the radiative linewidth is very strong, and in fact exceeds the frequency of the mode.

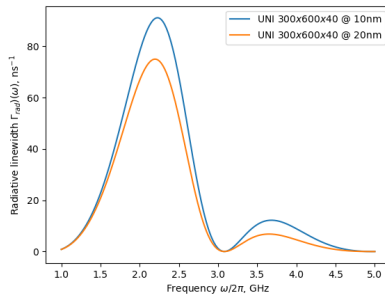


Figure V.16: Radiative linewidth for a finite-size resonator.

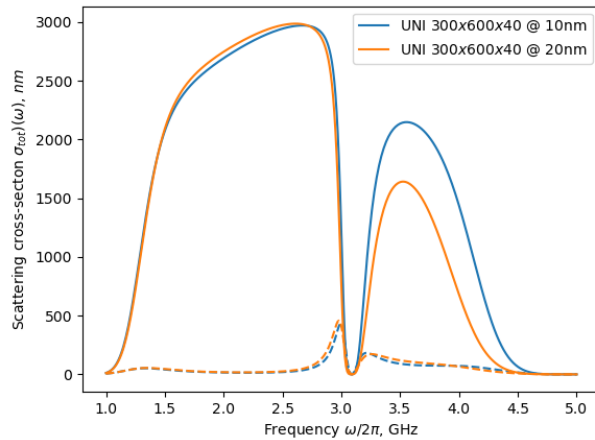


Figure V.17: Total cross-sections for scattering and absorption by a uniform mode. The absorption is shown by the dashed line of the respective colour.

The total scattering and absorption cross-sections are shown in Fig. V.17. The peculiar form of these curves reflects the suppression due to the full-wave condition which yields a minimum in  $\Gamma_{\text{rad}}(\omega)$  at approximately 3.1 GHz. Away from this point, the strong coupling between the resonant mode and the film saturates the cross-section in a wide frequency range where it reaches the unitary limit explained in the end of Sec. IV.5. In the absorption cross-section, one may notice a number of maxima which do not correspond to the resonant modes. Instead, these are due to increase in the linewidth when the frequency is raised at the lower end of the spectrum, and the full-wave condition at the high end.

One may also ask how this behaviour is modified if a synthetic antiferromagnet is used instead. A semi-realistic calculation is presented in Sec. ???. Here, we consider a simplified version of an antiferromagnetic mode: consider a resonator with its top half magnetised negatively, and bottom half magnetised positively. This would result in out-of-phase oscillations of  $m_x$  and in-phase oscillations of  $m_z$ , which can be easily incorporated via the respective formfactors. The resulting radiative linewidth is shown in Fig. V.18. One may notice a significant suppression in the overall magnitude. The scattering and absorption cross-sections are shown in Fig. V.19, and one may notice more regular shape of the resonant peaks, as the coupling is weakened in the antiferromagnetic mode.

Finally, forward- and backward-scattering cross-sections are shown in Fig. V.20 for both uniform and antiferromagnetic modes. A very strong, yet integrable, sin-

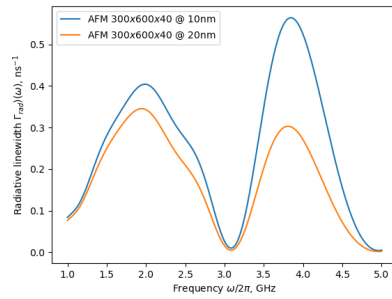


Figure V.18: Radiative linewidth for a finite-size resonator with an antiferromagnetic mode.

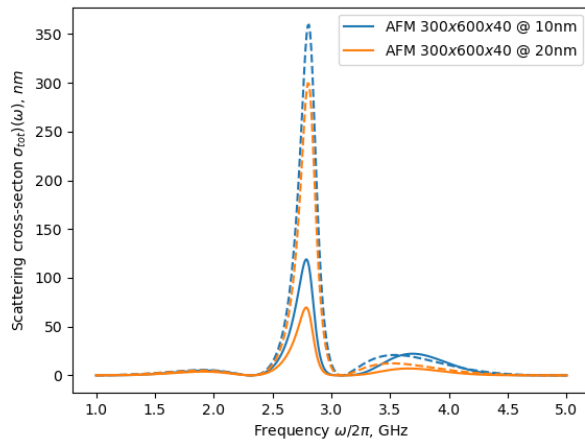


Figure V.19: Total cross-sections for scattering and absorption by an antiferromagnetic mode. The absorption is shown by the dashed line of the respective colour.

gularity occurs at  $f \approx 3.6$  GHz, when the constant-frequency contours is flattened.

Thus, we see that scattering by finite-size resonators may exhibit extra non-resonant features and one should exercise some care when interpreting the data of experiments or micromagnetic simulations.

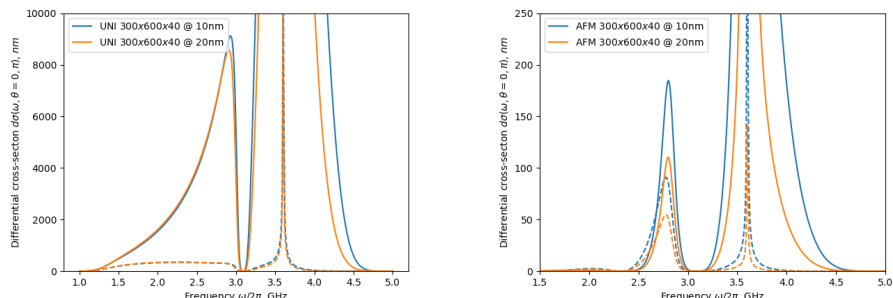


Figure V.20: Forward and backward scattering cross-sections are shown for both uniform and antiferromagnetic modes. The backward scattering cross-section is shown as a dashed curve of the respective colour. Left panel: uniform mode. Right panel: antiferromagnetic mode.

# Chapter VI

## Modelling large resonators

So far, our analysis assumed that the profiles of the localised resonant modes are already known, and were often assumed to be uniform. Often, this is a rather crude assumption. For a weak coupling between a resonator and a medium, one can instead compute the eigenmodes of an isolated resonator and assume they are not modified by the coupling. But the coupling does affect the resonant modes, e.g. due to the near-field effects, as it contributes to the self-energy of the modes and shifts the resonant frequencies. (Numerical experiments show that the frequencies of the modes may be rather prone to short-ranged effects, while their profiles are more robust.) This raises other questions: when a significant weight of the localised mode comes from the medium, how should one compute stray fields and avoid double-counting? The assumption of uniform magnetisation distribution may be rather inadequate for synthetic antiferromagnets. Therefore, a more systematic approach to the resonant modes may be desirable.

In this chapter, we discuss some methods to tackle that. We discuss the general structure of discretized Landau-Lifshitz-Gilbert equations and geometry of space of its solutions, which will be employed in what follows. We then explain how the models of isolated resonators can be modified to include near-field effects due to their coupling with the propagation medium. We shall also discuss how one can treat the case when the resonant modes overlap due to their strong coupling via the medium. Finally, we present the results of our simulations of synthetic antiferromagnets.

### VI.1 Mathematical structure of the LLG equations

To model large resonators with non-uniform resonant modes, one needs the profiles of the modes to be used in formfactor calculation. Let us discuss the structure of the linearised equations. If the Gilbert damping is negligible, they can be written in the form

$$\dot{\mathbf{m}} = \gamma_s [\mathbf{M}_s \times \mathbf{H}_{\text{eff}}(\mathbf{m})] , \quad (\text{VI.1.1})$$

where  $\mathbf{m}(t)$  is the vector formed by the dynamical magnetisation components,  $\mathbf{M}_s$  is the saturation magnetisation, so that  $\mathbf{M}_s \perp \mathbf{m}(t)$ , and  $\mathbf{H}_{\text{eff}}[\mathbf{m}]$  is the effective field. In the continuum theory, the latter is given by variation of the energy

functional with respect to magnetisation:

$$\mathbf{H}_{\text{eff}} = -\frac{\delta E[\mathbf{m}]}{\delta \mathbf{m}}, \quad (\text{VI.1.2})$$

where  $E[\mathbf{m}]$  is the energy functional.

To model a resonator numerically, one may discretise it into e.g. individual uniformly magnetised boxes. The resulting configuration is described by a  $2N$ -component vector, where  $N$  is the number of boxes in the resonator. In what follows,  $\mathbf{m}$  denotes such a vector. Recalling that the variational derivative is defined by the relation,

$$\delta E = \int_V \frac{\delta E}{\delta \mathbf{m}} \delta \mathbf{m} d^3 r \quad (\text{VI.1.3})$$

one can write for the field in the  $i$ th cell:

$$\Delta V_i \mathbf{H}_i = -\frac{\partial E}{\partial \mathbf{m}_i}, \quad (\text{VI.1.4})$$

where  $\mathbf{m}_i$  is the magnetisation of the cell, and  $\Delta V_i$  is the respective volume element. In the linearised regime, the energy is a real-valued quadratic function of the magnetisation, and can be specified by a symmetric ( $2N \times 2N$ ) matrix  $\mathcal{H}$ :

$$E[\mathbf{m}] = \frac{1}{2} \mathbf{m}^T \mathcal{H} \mathbf{m}, \quad (\text{VI.1.5})$$

where  $\mathbf{m}^T$  is the transposition of  $\mathbf{m}$ . One may assume  $\mathcal{H} = \mathcal{H}^T$ , as the antisymmetric terms drop out automatically. Thus,

$$\Delta V_i \mathbf{H}_i = -(\mathcal{H} \cdot \mathbf{m})_i \quad (\text{VI.1.6})$$

The equations for  $\mathbf{m}(t)$  can be written in the form

$$\boxed{\mathcal{I} \cdot \dot{\mathbf{m}} = \mathcal{H} \cdot \mathbf{m}}, \quad (\text{VI.1.7})$$

where

$$\boxed{\mathcal{I} \equiv \begin{pmatrix} 0 & -\text{diag} \frac{\Delta V}{\gamma_s M_s} \\ \text{diag} \frac{\Delta V}{\gamma_s M_s} & 0 \end{pmatrix}}. \quad (\text{VI.1.8})$$

The symbol diag denotes an  $N \times N$  matrix with elements  $\Delta V_i / (\gamma_s M_s)$  on its diagonal. (Note that one should use the values of  $\gamma_s M_s$  within the respective cell when these quantities are non-uniform.) By its definition,  $\mathcal{I}$  is antisymmetric:  $\mathcal{I}^T = -\mathcal{I}$ .

Eigenmodes  $\mathbf{m}_\omega$  of the resonator are then defined by solving a generalised eigenvalue problem. Setting  $\mathbf{m}(t) = \mathbf{m}_\omega \exp(-i\omega t)$ , one finds

$$-i\omega \mathcal{I} \mathbf{m}_\omega = \mathcal{H} \mathbf{m}_\omega, \quad (\text{VI.1.9})$$

in which matrices  $\mathcal{H}$  and  $i\mathcal{I}$  on both sides are Hermitian. For comparison, it may be helpful to recall that eigenmodes of a coupled oscillator system mass matrix  $\mathcal{M}$  and rigidity matrix  $\mathcal{K}$  are obtained by solving the generalised eigenvalue problem

$$\omega^2 \mathcal{M} \mathbf{x}_\omega = \mathcal{K} \mathbf{x}_\omega, \quad (\text{VI.1.10})$$

where  $\mathbf{x}$  are the coordinates of the oscillators. Both matrices  $\mathcal{M}$  and  $\mathcal{K}$  are assumed to be Hermitian and positive. The generalised problem is reduced to a standard eigenvalue problem by passing to different coordinate system,  $\mathbf{y}_\omega = \sqrt{\mathcal{M}}\mathbf{x}_\omega$ , which transforms the mass matrix into the identity matrix, and replaces the rigidity matrix with  $\tilde{\mathcal{K}} = \mathcal{M}^{-1/2}\mathcal{K}\mathcal{M}^{-1/2}$ . The latter is guaranteed to be Hermitian. In the new basis, the modes obey the standard eigenvalue equation

$$\omega^2 \mathbf{y}_\omega = \tilde{\mathcal{K}} \mathbf{y}_\omega . \quad (\text{VI.1.11})$$

According to the standard theory of linear systems, the modes  $\mathbf{y}_\omega$  are orthogonal to each other:  $\mathbf{y}_{\omega'}^\top \cdot \mathbf{y}_\omega = 0$  if  $\omega' \neq \omega$ . This means the modes  $\mathbf{x}_\omega$  obey the orthogonality relation with the mass matrix:

$$\mathbf{x}_{\omega'}^\top \cdot \mathcal{M} \cdot \mathbf{x}_\omega = 0 \quad \text{if} \quad \omega' \neq \omega . \quad (\text{VI.1.12})$$

Thus, the mass matrix specifies the metric relationships in the space of solutions of the eigenvalue problems.

The LLG eigensystem (VI.1.9) is formally similar to a generalised eigensystem, with an important difference: the matrix  $i\mathcal{I}$  is not positive, and hence has no hermitian square root. To derive the properties of its eigenvectors and eigenvalues, we first notice that the right-hand side of the original equation has only real coefficients, while the coefficients on the left-hand side are purely imaginary. This makes the modes  $\mathbf{m}_\omega$  complex-valued. One may link together the modes with positive and negative frequencies<sup>1</sup>: if  $\mathbf{m}_\omega$  is an eigenmode belonging to eigenvalue  $\omega$ , then  $\bar{\mathbf{m}}_\omega$  is also an eigenmode belonging to the negative eigenvalue  $(-\omega)$ :

$$-i(-\omega)\mathcal{I}\bar{\mathbf{m}}_\omega = \mathcal{H}\bar{\mathbf{m}}_\omega , \quad (\text{VI.1.13})$$

so that it suffices to consider only the positive eigenmodes with  $\omega > 0$ , as the negative eigenmodes can be obtained via  $\mathbf{m}_{-\omega} = \bar{\mathbf{m}}_\omega$ . The real-valued solutions are given by superposition of the two contributions:

$$\mathbf{m}(t) = \operatorname{Re} \mathbf{m}_\omega \varphi_\omega(t) = \frac{1}{2} \mathbf{m}_\omega \varphi_\omega(t) + \frac{1}{2} \bar{\mathbf{m}}_\omega \bar{\varphi}_\omega(t) , \quad (\text{VI.1.14})$$

where  $\varphi_\omega(t)$  is the respective oscillator variable:  $\varphi_\omega(t) \propto \exp(-i\omega t)$ . (This approach works both for localised and delocalised modes; however, in the delocalised case one should also change the sign of the wavevector,  $\mathbf{k} \rightarrow -\mathbf{k}$ .) Thus, one may focus on the positive-frequency solutions only.

Now consider two eigenmodes  $\mathbf{m}_{1,2}$  belonging to eigenvalues  $\omega_{1,2}$  respectively, and compute the quantity  $\mathbf{m}_2^\top \cdot \mathcal{H} \cdot \mathbf{m}_1$ . Employing the eigenvalue equation, one may write

$$\mathbf{m}_2^\top \cdot \mathcal{H} \cdot \mathbf{m}_1 = -i\omega_1 \mathbf{m}_2^\top \cdot \mathcal{I} \cdot \mathbf{m}_1 . \quad (\text{VI.1.15})$$

On the other hand, since  $\mathcal{H}^\top = \mathcal{H}$  and  $\mathcal{I}^\top = -\mathcal{I}$ , one may switch the action of the operators to the right to obtain

$$\mathbf{m}_2^\top \cdot \mathcal{H} \cdot \mathbf{m}_1 = i\omega_2 \mathbf{m}_2^\top \cdot \mathcal{I} \cdot \mathbf{m}_1 . \quad (\text{VI.1.16})$$

---

<sup>1</sup> For a finite Gilbert damping, the modes can be classified by the sign of the real part of their frequency. Conjugation then transforms a mode with frequency  $\omega_1 + i\omega_2$  into a mode with frequency  $-\omega_1 + i\omega_2$ , so that a decaying mode remains decaying.

Together, these relations imply

$$(\omega_1 + \omega_2) \mathbf{m}_2^T \cdot \mathcal{I} \cdot \mathbf{m}_1 = 0 . \quad (\text{VI.1.17})$$

We can now introduce the overlap between the modes defined as

$$\langle \mathbf{m}_2, \mathbf{m}_1 \rangle \equiv \mathbf{m}_2^T \cdot \mathcal{I} \cdot \mathbf{m}_1 = \int \frac{d^3r}{\gamma_s M_s} [m_{z,2}(\mathbf{r}) m_{x,1}(\mathbf{r}) - m_{x,2}(\mathbf{r}) m_{z,1}(\mathbf{r})] .$$

(VI.1.18)

Let us establish its basic properties. Firstly, from the definition (VI.1.18), it is obvious that the overlap is antisymmetric:

$$\langle \mathbf{m}_1, \mathbf{m}_2 \rangle = -\langle \mathbf{m}_2, \mathbf{m}_1 \rangle , \quad (\text{VI.1.19})$$

so that  $\langle \mathbf{m}, \mathbf{m} \rangle = 0$ . Secondly, from the above relation we see it is only non-zero when  $\omega_1 + \omega_2 = 0$ . We therefore conclude that for all the positive-energy modes  $\langle \mathbf{m}_1, \mathbf{m}_2 \rangle = 0$ .

Consider now frequencies  $-\omega_1 < 0$  and  $\omega_2 > 0$ , and express the overlap in terms of the positive frequency components, replacing  $\mathbf{m}_1$  with  $\bar{\mathbf{m}}_1$ . If the eigenvalues are non-degenerate, the overlap also vanishes:

$$\langle \bar{\mathbf{m}}_1, \mathbf{m}_2 \rangle = 0 , \quad \text{for } \omega_1 \neq \omega_2 . \quad (\text{VI.1.20})$$

Finally, if  $\omega_1 = -\omega_2 = -\omega$ , the overlap  $\langle \bar{\mathbf{m}}_\omega, \mathbf{m}_\omega \rangle$  may be non-zero, and one may link it to the energy of the real-valued oscillation (VI.1.14):

$$\begin{aligned} E[\mathbf{m}(t)] &= \frac{1}{2} \mathbf{m}^\dagger(t) \cdot \mathcal{H} \cdot \mathbf{m}(t) = \frac{1}{8} (-i\omega) [\langle \bar{\mathbf{m}}_\omega, \mathbf{m}_\omega \rangle - \langle \mathbf{m}_\omega, \bar{\mathbf{m}}_\omega \rangle] \\ &= \frac{\omega}{4i} \langle \bar{\mathbf{m}}_\omega, \mathbf{m}_\omega \rangle . \end{aligned} \quad (\text{VI.1.21})$$

Therefore, the value of  $\langle \bar{\mathbf{m}}_\omega, \mathbf{m}_\omega \rangle$  is proportional to the number  $E/\omega$  of quanta excited in the mode. For the single-magnon normalisation considered previously, we write

$$\langle \bar{\mathbf{m}}_\omega, \mathbf{m}_\omega \rangle = 4i . \quad (\text{VI.1.22})$$

One can summarise our findings in terms of positive-frequency modes:

$$\langle \bar{\mathbf{m}}_{\omega'}, \mathbf{m}_\omega \rangle = 4i \delta_{\omega' \omega} , \quad \langle \mathbf{m}_{\omega'}, \mathbf{m}_\omega \rangle = \langle \bar{\mathbf{m}}'_\omega, \bar{\mathbf{m}}_\omega \rangle = 0 ,$$

(VI.1.23)

where  $\delta_{\omega' \omega}$  is the standard Kronecker's delta-symbol.

We see that the space of solutions of the LLG equation can be equipped with an antisymmetric scalar product  $\langle \bar{\mathbf{m}}_2, \mathbf{m}_1 \rangle$  that vanishes between different eigenmodes, and gives the number of quanta if the two modes are the same. Spaces with an antisymmetric scalar product are known as *symplectic spaces*, and antisymmetric scalar product specified by the matrix  $\mathcal{I}$  is known as the respective *symplectic structure*. Symplectic spaces are different from ordinary Euclidean spaces in many important aspects. The coordinate system in a symplectic space can be changed in such a way that the symplectic structure is preserved, such isometries form the *symplectic group*. The symplectic structure is usually specified via the matrix

$$\mathcal{I}_{\text{std}} = \begin{bmatrix} 0 & -1 \\ 1 & 0 \end{bmatrix} , \quad (\text{VI.1.24})$$

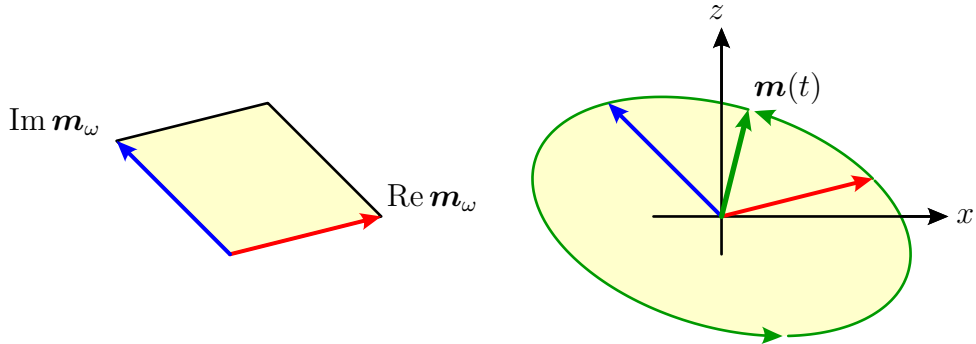


Figure VI.1: Left: complex-valued mode vector  $\mathbf{m}_\omega$  defines a parallelogram spanned by its real and imaginary components. Right: the corresponding precession ellipse. Both areas are proportional to the cross-product  $\text{Re } \mathbf{m}_\omega \times \text{Im } \mathbf{m}_\omega$ .

but in general, it does not have to be of this canonical form: it can be specified by an arbitrary antisymmetric matrix. It is known, though, that if the matrix  $\mathcal{I}$  is non-degenerate, one may find a set of base vectors in which it takes the standard form. Such a basis is also known as a symplectic basis. Its choice is not unique: two different symplectic bases are related via a symplectic transform. The antisymmetric combination of the components of  $\mathbf{m}$  in the scalar product has a geometric interpretation: it is the area spanned by parallelogram based on  $\text{Re } \mathbf{m}_\omega$  and  $\text{Im } \mathbf{m}_\omega$ , shown in the left panel of Fig. VI.1. Indeed:

$$\bar{m}_{x,\omega} m_{z,\omega} - \bar{m}_{x,\omega} m_{z,\omega} = \bar{\mathbf{m}}_\omega \times \mathbf{m}_\omega = 2i \text{Re } \mathbf{m}_\omega \times \text{Im } \mathbf{m}_\omega . \quad (\text{VI.1.25})$$

The two vectors  $\text{Re } \mathbf{m}_\omega(\mathbf{r})$  and  $\text{Im } \mathbf{m}_\omega(\mathbf{r})$  define precession ellipse swept by the magnetisation  $\mathbf{m}(t, \mathbf{r})$  at a given point  $\mathbf{r}$  in the sample, and one may show that the area  $S$  of the ellipse is proportional to the same quantity:

$$S = \pi \text{Re } \mathbf{m}_\omega \times \text{Im } \mathbf{m}_\omega = \frac{\pi}{2i} \bar{\mathbf{m}}_\omega \times \mathbf{m}_\omega . \quad (\text{VI.1.26})$$

An important example of a symplectic space is the phase space of a mechanical system with generalised coordinates  $(q_1, \dots, q_n)$  and corresponding canonical momenta  $(p_1, \dots, p_n)$ . Points in the phase space can be specified as  $2n$ -component vectors  $(q_1, \dots, q_n; p_1, \dots, p_n)$ . In general, distances between such points are ill-defined, as coordinates and momenta have different physical units. Nevertheless, for two arbitrary vectors in this space one may consider the parallelogram spanned by them, and project it to individual planes  $(q_1, p_1)$ ,  $(q_2, p_2)$ , etc. The sum of projected areas gives the metric in this space. One may also notice the similarity between Hamiltonian equations in the phase space and the LLG equations if one identifies e.g. the magnetisation component  $m_x$  with a coordinate and the other component,  $m_z$ , with the respective canonical momentum, up to the factor  $\gamma_s M_s$ .

Let us also recall some important facts from mechanics that are connected with the symplectic geometry of phase space. One may recall the formula for the action of a mechanical system

$$\begin{aligned} S[\mathbf{q}(t)] &= \int L dt = \int [\mathbf{p} \cdot \dot{\mathbf{q}} - H(\mathbf{p}, \mathbf{q})] dt \\ &= \int \mathbf{p} \cdot d\mathbf{q} - \int H(\mathbf{p}, \mathbf{q}) dt , \end{aligned} \quad (\text{VI.1.27})$$

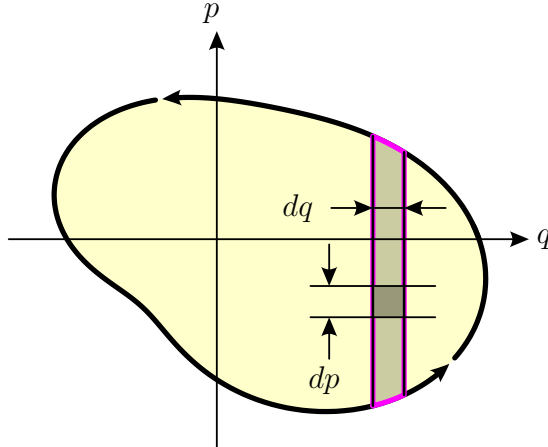


Figure VI.2: Phase space trajectory for a one-dimensional mechanical system. The element of the area swept by the trajectory is  $dpdq$ , integrating it over vertical stripes as shown in the figure yields the abbreviated action  $pdq$ .

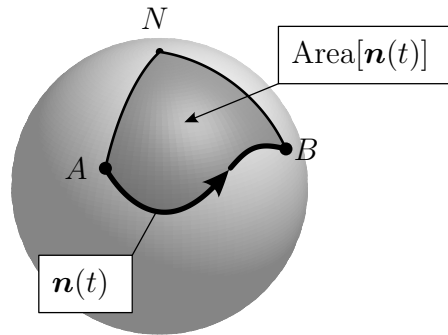


Figure VI.3: The action for spin is proportional to area on the unit sphere swept by the tip of the unit vector  $\mathbf{n}(t)$  describing the orientation of the spin. The area is measured from a fixed arbitrary point, such as the North pole  $N$ .

where  $H(\mathbf{p}, \mathbf{q})$  is the Hamiltonian, and  $L = \mathbf{p} \cdot \dot{\mathbf{q}} - H(\mathbf{p}, \mathbf{q})$  is the Lagrangian. The first term in Eq. (VI.1.27) is known as the Maupertuis action, or abbreviated action, and it is sometimes used to analyse motion with conserved energy. For a system moving along a closed trajectory in one dimension, this quantity is equal to the area swept by the trajectory, as can be seen from Fig. VI.2:

$$\oint pdq = \iint dpdq . \quad (\text{VI.1.28})$$

For a harmonic oscillator of frequency  $\omega$ , it is equal to  $\pi E/\omega$ , and therefore is proportional to the number of quanta in the mode, if one neglects the zero-point motion energy  $1/2\hbar\omega$ . By virtue of the Bohr-Sommerfeld quantisation rule, this is in fact true for an arbitrary mechanical system that exhibits a quasiperiodic motion. This quantity is also known as the adiabatic invariant, and is known to be conserved when parameters of the oscillator are slowly varied. One may also recall the theorems by Darboux and Liouville that state that the phase-space areas and volumes are preserved by Hamiltonian dynamics.

Magnetisation dynamics in the LLG equations can be also described with the help of an action functional. It is well-known that dynamics of a quantum spin  $s$  can be described by introducing the respective action functional for a unit vector  $\mathbf{n}$  describing orientation of the spin. The “kinetic” term in the action is proportional

to the area swept by the tip of  $\mathbf{n}(t)$  on the sphere, see Fig. VI.3:

$$S[\mathbf{n}] = \hbar s \text{Area}[\mathbf{n}(t)] - \int E(\mathbf{n}(t)) dt . \quad (\text{VI.1.29})$$

(The first term represents the Berry phase picked up by the spin.) In general, the area swept by magnetisation on a unit sphere is difficult to define explicitly. However, when  $\mathbf{m}_{x,z} \ll M_s$ , one may neglect the curvature, so that the area swept in a short time segment  $dt$  is given by  $1/2\mathbf{n}_0 \cdot [\mathbf{n}_\perp \times \dot{\mathbf{n}}_\perp] dt$ , where  $\mathbf{n}_\perp \approx \mathbf{n} - \mathbf{n}_0$  is the deviation of the vector  $\mathbf{n}$  from its equilibrium position  $\mathbf{n}_0$ . One may link this vector to the respective magnetic dipole  $\boldsymbol{\mu} = \gamma_s \hbar s \mathbf{n}$ . Summing up the “kinetic” terms over all the spins yields the action for magnetisation dynamics in the linearised regime:

$$S[\mathbf{m}(t)] = \int \frac{d^3 \mathbf{r} dt}{2\gamma_s M_s} [m_x \dot{m}_z - m_z \dot{m}_x] - \int dt E[\mathbf{m}(t, \mathbf{r})] . \quad (\text{VI.1.30})$$

Integration by parts in the first term reduces it to the form  $m_x dm_z$ , similar to  $\mathbf{p} \cdot d\mathbf{q}$ . One may therefore conclude that (i) this quantity gives the number of excitations, (ii) that it is conserved by the dynamics, and (iii) it is unchanged when parameters of the resonator are varied adiabatically. The interpretation in terms of the Berry phase highlights the connection between the action and the total area of precession ellipses swept by all the spins in the sample.

Symplectic structure of phase space is technically helpful. It allows one to normalize the eigenmodes in an error-prone way: by demanding that

$$\langle \bar{\mathbf{m}}_\omega, \mathbf{m}_\omega \rangle \equiv \int \frac{d^3 \mathbf{r}}{\gamma_s M_s} [\bar{m}_z(\mathbf{r}) m_x(\mathbf{r}) - \bar{m}_x(\mathbf{r}) m_z(\mathbf{r})] = 4i , \quad (\text{VI.1.31})$$

one obtains the energy  $E[\mathbf{m}] = \omega$ . Moreover, one may write a general real-valued solution as a sum over modes

$$\mathbf{m}(t) = \text{Re} \sum_\omega \mathbf{m}_\omega \varphi_\omega(t) = \frac{1}{2} \sum_\omega \mathbf{m}_\omega \varphi_\omega(t) + \frac{1}{2} \sum_\omega \bar{\mathbf{m}}_\omega \bar{\varphi}_\omega(t) \quad (\text{VI.1.32})$$

and show that the energy takes the expected form

$$E[\mathbf{m}(t)] = \sum_\omega \omega |\varphi_\omega(t)|^2 , \quad (\text{VI.1.33})$$

in which all of the modes are decoupled.

The symplectic structure also provides a regular method to check closeness of the two modes by computing the relevant scalar product, and to extract the contribution of a given mode from a complicated distribution  $\mathbf{m}(\mathbf{r})$ . Also, invariance of equations of motion under the symplectic group restrict their form.

## VI.2 Treatment of the Gilbert damping

Let us now discuss how the equations are modified when the Gilbert damping is present. The damping enters via the term proportional to the derivative of the magnetisation, so that the resulting equations can be written in the form

$$(\mathcal{I} - \mathcal{A}) \cdot \dot{\mathbf{m}} = \mathcal{H} \cdot \mathbf{m} + \mathbf{h} , \quad (\text{VI.2.1})$$

where the symmetric matrix  $\mathcal{A} \sim \alpha$  describes the effect of the damping:

$$\mathcal{A} = \begin{pmatrix} \text{diag} \frac{\alpha(\mathbf{r}_i) \Delta V_i}{\gamma_s M_s(\mathbf{r}_i)} & \\ & \text{diag} \frac{\alpha(\mathbf{r}_i) \Delta V_i}{\gamma_s M_s(\mathbf{r}_i)} \end{pmatrix} .$$

The term  $\mathbf{h}$  represents external fields applied to the resonator, either from external sources or from waves propagating in a medium nearby. The spectral theory for Eq. (VI.2.1) is more complicated, as the matrix on the right-hand side is neither symmetric or antisymmetric:  $(\mathcal{I} - \mathcal{A})^T = -\mathcal{I}^T - \mathcal{A}^T$ . First, the eigenfrequencies  $\omega_a = \Omega_a - i\Gamma_a$  are in general complex-valued. However, since the differential equation is real-valued, its eigenmodes occur in complex-conjugate pairs: if  $\mathbf{m}_a(t)$  is an eigenvector for the  $a$ th mode,

$$-i(\Omega_a - i\Gamma_a)(\mathcal{I} - \mathcal{A}) \cdot \mathbf{m}_a = \mathcal{H} \cdot \mathbf{m}_a , \quad (\text{VI.2.2})$$

then  $\bar{\mathbf{m}}_a$  is an eigenvector for the conjugate mode with frequency  $-\bar{\omega}_a = -\Omega_a - i\Gamma_a$ :

$$-i(-\Omega_a - i\Gamma_a)(\mathcal{I} - \mathcal{A}) \cdot \bar{\mathbf{m}}_a = \mathcal{H} \cdot \bar{\mathbf{m}}_a .$$

This way, one may expand the dynamics over the eigenmodes:

$$\mathbf{m}(t) = \frac{1}{2} \sum_a [\mathbf{m}_a \varphi_a(t) + \bar{\mathbf{m}}_a \bar{\varphi}_a(t)] = \sum_a \text{Re } \mathbf{m}_a \varphi_a(t) . \quad (\text{VI.2.3})$$

Free dynamics is described by decaying complex exponentials:

$$\varphi_a(t) \propto \exp(-i\Omega_a t - \Gamma_a t) \quad \bar{\varphi}_a(t) \propto \exp(i\Omega_a t - \Gamma_a t) .$$

However, the eigenvectors  $\mathbf{m}_a$  are no longer orthogonal. The analogue of Eq. (VI.1.17) now takes the form

$$i(\omega_a + \omega_b) \mathbf{m}_b^T \cdot \mathcal{I} \cdot \mathbf{m}_a - i(\omega_a - \omega_b) \mathbf{m}_b^T \cdot \mathcal{A} \cdot \mathbf{m}_b = 0 . \quad (\text{VI.2.4})$$

In particular, one may apply it to a pair of conjugated modes:  $\mathbf{m}_b = \bar{\mathbf{m}}_a$ ,  $\omega_b = -\Omega_a - i\Gamma_a$ . Thus, one finds

$$\Gamma_a \mathbf{m}_a^\dagger \cdot \mathcal{I} \cdot \mathbf{m}_a = i\Omega_a \mathbf{m}_a^\dagger \cdot \mathcal{A} \cdot \mathbf{m}_a , \quad (\text{VI.2.5})$$

which can be interpreted in terms of (averaged) energy dissipation proportional to  $\mathbf{m}^T \cdot \mathcal{A} \cdot \mathbf{m}$ . In general, however, one cannot make e.g. a conclusion about orthogonality of two modes with different positive frequencies.

To separate the dynamics of individual damped modes, one may introduce the dual basis  $\tilde{\mathbf{m}}_a$ , such that

$$\tilde{\mathbf{m}}_b^T \cdot (\mathcal{I} - \mathcal{A}) \cdot \mathbf{m}_a = 4i\delta_{ab} , \quad (\text{VI.2.6})$$

which can be viewed as a modification of Eq. (VI.1.23). (The dual vectors  $\tilde{\mathbf{m}}^T$  form a basis in the space  $V^*$  dual to the space  $V$  spanned by vectors  $\mathbf{m}_a$ .) The direct comparison indicates that  $\tilde{\mathbf{m}}_a = \bar{\mathbf{m}}_a + O(\alpha)$ , assuming that the eigenmodes  $\mathbf{m}_a$  are still normalised as before<sup>2</sup>:

$$\tilde{\mathbf{m}}_a^T \cdot \mathcal{I} \cdot \mathbf{m}_a = 4i .$$

<sup>2</sup> When the modes  $\mathbf{m}_a$  are rescaled by a factor  $C$ , the dual modes  $\tilde{\mathbf{m}}_a$  are to be rescaled by  $C^{-1}$ , so that even for  $\alpha = 0$  the dual modes cease to be equal to  $\bar{\mathbf{m}}_a$ .

If the eigenmodes are non-degenerate, one may use Eq. (VI.2.5) to obtain a more accurate expression:

$$\tilde{\mathbf{m}}_a \approx \eta_a \bar{\mathbf{m}}_a , \quad \eta_a \equiv \frac{\Omega_a}{\Omega_a + i\Gamma_a} ,$$

which includes the first-order contribution along the original vector. The dual vectors  $\tilde{\mathbf{m}}_a$  satisfy the equation for the left eigenvectors of the eigensystem (VI.2.2):

$$-i\omega_a \tilde{\mathbf{m}}_a^T \cdot (\mathcal{I} - \mathcal{A}) = \tilde{\mathbf{m}}_a^T \cdot \mathcal{H} .$$

Hence they can be obtained by taking left eigenvectors and normalising them properly. One can also verify that the dual vector for the conjugate mode  $\bar{\mathbf{m}}_a$  is given by conjugate of the dual vector  $-\tilde{\mathbf{m}}_a$ . (The negative sign is due to a different sign of  $\langle \mathbf{m}, \mathbf{m} \rangle$  for negative-frequency modes.)

One can employ the basis to obtain equations of motion for a system driven by an external field  $\mathbf{h}(t)$ . Let the solution to Eq. (VI.2.1) be of the form (VI.2.3) with unknown mode variables  $\varphi_a(t)$ . The contribution of the  $a$ th mode can be singled out by projecting Eq. (VI.2.1) to the respective dual direction:

$$\tilde{\mathbf{m}}_a^T \cdot (\mathcal{I} - \mathcal{A}) \sum_b \frac{1}{2} \mathbf{m}_b \dot{\varphi}_b(t) = \tilde{\mathbf{m}}_a^T \cdot \mathcal{H} \sum_b \frac{1}{2} \mathbf{m}_b \varphi_b(t) + \tilde{\mathbf{m}}_a^T \cdot \mathbf{h}(t) .$$

(Here, for brevity, the sum over  $b$  denotes a sum over both positive and negative frequency modes.) Using the definition (VI.2.6), together with the eigenvalue equation (VI.2.2), one obtains an equation for a driven oscillator,

$$i\dot{\varphi}_a = (\Omega_a - i\Gamma_a)\varphi_a + \Phi_a(t) ,$$

with the source term

$$\Phi_a(t) \equiv \frac{1}{2} \tilde{\mathbf{m}}_a^T \cdot \mathbf{h}(t) .$$

We see that the field is projected to the dual vector. Similarly, one finds for the conjugate mode:

$$i\dot{\bar{\varphi}}_a = (-\Omega_a - i\Gamma_a)\bar{\varphi}_a + \bar{\Phi}_a(t) , \quad \bar{\Phi}_a(t) \equiv -\frac{1}{2} \tilde{\mathbf{m}}_a^T \cdot \mathbf{h}(t) .$$

This leads to the following observation. When the damping of the resonant mode is significant, its hybridisation with external fields or propagating modes is no longer symmetric. The hybridisation coefficients  $\Delta_{\mathbf{k}}$  and  $\Delta'_{\mathbf{k}}$  that describe emission produced by the mode depend upon the mode profile and therefore are expressed in terms of the eigenvector  $\mathbf{m}_a$ . However, the effect of external fields or modes on the damped mode involve the dual eigenvector  $\tilde{\mathbf{m}}_a$ , so that the couplings  $\bar{\Delta}_{\mathbf{k}}$  and  $\bar{\Delta}'_{\mathbf{k}}$  should be modified accordingly. This may result in slight violation of reciprocity of the coupling.

## VI.3 The near-field approximation

When a resonator is brought into proximity with a medium that hosts propagating waves, the coupling between the two affects eigenmodes of the resonator. This

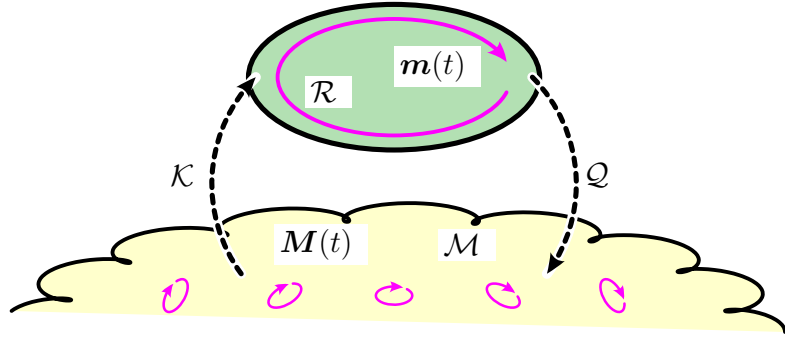


Figure VI.4: Resonator with magnetisation  $\mathbf{m}(t)$  is coupled to the medium with magnetisation  $\mathbf{M}(t)$  via near-field effects.

involves physical effects of a different nature. There are near-field effects that occur at short distances of the order of the dimensions of the resonator: the oscillating mode in the resonator induces a response in the medium, which in turn affects the resonant mode. This can be thought of as a magnetic analogue of screening in electrostatics. There is also a different contribution: oscillating field in the resonator excites outgoing waves that carry away the energy, and thus result in radiative friction. The outgoing wave is formed at large distances, of the order of  $k_\omega^{-1}$ . The self-energy  $\Sigma(\omega)$  of the resonator introduced in Sec. IV.4 treats both effects on equal footing: the near-field screening contributes to its real part, while the radiative friction gives rise to its imaginary part. In general, this hinders numerical modelling a resonator: the attached medium should have diameter of at least several wavelengths, the propagating modes are affected by boundary conditions, and only a handful of these modes would fall within radiative linewidth of the resonator. It would be desirable to separate the near-field and radiative contributions, so that one can model the near-field coupling using moderate-size systems, and then consider its coupling to an infinite medium by computing the respective radiative linewidths from the profile of the relevant modes. Here we explain how this could be achieved.

Consider the LLG equations describing the resonator coupled with the medium as shown in Fig. VI.4:

$$\begin{aligned} \mathcal{I}_R \dot{\mathbf{m}} &= \mathcal{R}\mathbf{m} + \mathcal{K}\mathbf{M}, \\ \mathcal{I}_M \dot{\mathbf{M}} &= \mathcal{M}\mathbf{M} + \mathcal{Q}\mathbf{m} + \mathbf{J}. \end{aligned} \quad (\text{VI.3.1})$$

Here  $\mathbf{m}$  is the magnetisation in the resonator, and  $\mathbf{M}$  is the magnetisation in the medium. The matrix  $\mathcal{R}$  describes the effective fields induced by an isolated resonator in itself, while the matrix  $\mathcal{M}$  describes the dynamics of an isolated medium. These matrices include both dipolar and exchange fields, and perhaps other contributions. The matrices  $\mathcal{I}_R$  and  $\mathcal{I}_M$  describe the kinetic response to the fields, and also define the symplectic structure of the LLG equations. As it was discussed in the previous section, they scale as  $(\gamma_s M_s)^{-1}$  with the gyromagnetic ratio  $\gamma_s$  and static magnetisation  $M_s$ . The matrices  $\mathcal{K}$  describe the influence of the medium on the resonator and vice versa, so that one should expect  $\mathcal{Q} = \mathcal{K}^T$ . The relevant coupling is provided by stray dipolar fields. Finally, we introduced the source  $\mathbf{J}$  that would describe external excitation in the medium. Let us attempt to solve these equations. For a monochromatic wave, the second equation can be

recast as

$$(-i\omega\mathcal{I}_M - \mathcal{M})\mathbf{M} = \mathcal{Q}\mathbf{m} + \mathbf{J}, \quad (\text{VI.3.2})$$

and is solved by

$$\mathbf{M} = \frac{1}{-i\omega\mathcal{I}_M - \mathcal{M}}\mathcal{Q}\mathbf{m} + \mathbf{M}_{\text{inc}}, \quad (\text{VI.3.3})$$

where the incident wave is

$$\mathbf{M}_{\text{inc}} = \frac{1}{-i\omega\mathcal{I}_M - \mathcal{M}}\mathbf{J}. \quad (\text{VI.3.4})$$

(Here and below, the fractions denote matrix inversion, and one should be careful about ordering in the matrix dot products.) Then, the dynamics of the resonator variables obeys the equation

$$\left[ -i\omega\mathcal{I}_R - \mathcal{R} - \mathcal{K}\frac{1}{-i\omega\mathcal{I}_M - \mathcal{M}}\mathcal{Q} \right] \mathbf{m} = \mathcal{K}\mathbf{M}_{\text{inc}}. \quad (\text{VI.3.5})$$

We see that the dynamics of the resonator is modified by the contribution

$$\hat{\Sigma}(\omega) = \mathcal{K}\frac{1}{-i\omega\mathcal{I}_M - \mathcal{M}}\mathcal{Q}, \quad (\text{VI.3.6})$$

which represents the self-energy of the resonator (IV.4.5). One may link the two expressions by noticing that the contribution of the infinite medium can be represented as a sum over modes with a well-defined wavevectors  $\mathbf{k}$ , so that the matrix  $\mathcal{M}$  is diagonal in  $\mathbf{k}$  with eigenvalues  $\omega_{\mathbf{k}}$  on the diagonal. Then,  $\Delta_{\mathbf{k}}$  would play the role of  $\mathcal{Q}$  and  $\bar{\Delta}_{\mathbf{k}}$  the role of  $\mathcal{K}$ .

To separate the near-field effects, we use the following insight: near-fields are not retarded, and therefore can be obtained if one neglects retardation in the medium. The latter is controlled by the respective gyromagnetic ratio: when it is formally sent to infinity, magnetisation of the medium is enslaved by that of the resonator. This is similar to how setting the speed of light  $c$  to infinity suppresses retardation and reduces Maxwell's equations to electrostatics and magnetostatics of the near fields. For the LLG equations, this is achieved by dropping the terms proportional to  $\mathcal{I}_M$ , so that the dynamics of the resonator is described by the effective matrix

$$\mathcal{R}_{\text{nrf}} \equiv \mathcal{R} - \mathcal{K}\mathcal{M}^{-1}\mathcal{Q}. \quad (\text{VI.3.7})$$

In other words, the self-energy  $\Sigma$  is replaced by its value at  $\omega = 0$ .

Let us derive this approximation more rigorously. By expressing  $\mathcal{R}$  in terms of  $\mathcal{R}_{\text{nrf}}$ , one finds

$$\left[ -i\omega\mathcal{I}_R - \mathcal{R}_{\text{nrf}} - \mathcal{K}\mathcal{M}^{-1}\mathcal{Q} + \mathcal{K}\frac{1}{i\omega\mathcal{I}_M + \mathcal{M}}\mathcal{Q} \right] \mathbf{m} = \mathcal{K}\mathbf{M}_{\text{inc}}. \quad (\text{VI.3.8})$$

Simplifying the last two terms on the left-hand side, we arrive at

$$\left[ -i\omega\mathcal{I}_R - \mathcal{R}_{\text{nrf}} - i\omega\mathcal{K}\frac{1}{i\omega\mathcal{I}_M + \mathcal{M}}\mathcal{I}_M\mathcal{M}^{-1}\mathcal{Q} \right] \mathbf{m} = \mathcal{K}\mathbf{M}_{\text{inc}}. \quad (\text{VI.3.9})$$

Since the equation for an isolated resonator involves the term proportional to  $\omega$ , it makes sense to retain this term. (This is equivalent to retaining the linear in  $\omega$  term in  $\hat{\Sigma}(\omega)$ .) One may rewrite the above relation as

$$\left[ -i\omega\mathcal{I}_{\text{nrf}} - \mathcal{R}_{\text{nrf}} - \omega^2\mathcal{K}\mathcal{M}^{-1}\mathcal{I}_M\frac{1}{i\omega\mathcal{I}_M + \mathcal{M}}\mathcal{I}_M\mathcal{M}^{-1}\mathcal{Q} \right] \mathbf{m} = \mathcal{K}\mathbf{M}_{\text{inc}}, \quad (\text{VI.3.10})$$

with the renormalised symplectic structure:

$$\mathcal{I}_{\text{nrf}} \equiv \mathcal{I}_R + \mathcal{K}\mathcal{M}^{-1}\mathcal{I}_M\mathcal{M}^{-1}\mathcal{Q} . \quad (\text{VI.3.11})$$

The remaining correction scales as  $\omega^2$  and therefore becomes less relevant when linear dimensions  $a$  of the resonator are much smaller than the wavelength  $\lambda_\omega$ .

Thus, the near-field modes of the resonator can be obtained by solving the eigenvalue problem with renormalised matrices:

$$-i\omega\mathcal{I}_{\text{nrf}}\mathbf{m}_\omega = \mathcal{R}_{\text{nrf}}\mathbf{m}_\omega , \quad (\text{VI.3.12})$$

so that the eigenvalues are found by diagonalising the matrix  $\mathcal{I}_{\text{nrf}}^{-1}\mathcal{R}_{\text{nrf}}$ . The matrix  $\mathcal{R}_{\text{nrf}}$  couples together the nodes of the resonator, and yields a set of well-separated discrete modes. They obey the orthogonality relation with the amended symplectic structure  $\mathcal{I}_{\text{nrf}}$ :

$$\langle \bar{\mathbf{m}}_{\omega'}, \mathbf{m}_\omega \rangle_{\text{nrf}} \equiv \bar{\mathbf{m}}_{\omega'} \cdot \mathcal{I}_{\text{nrf}} \cdot \mathbf{m}_\omega = 0 , \quad \text{for } \omega' \neq \omega , \quad (\text{VI.3.13})$$

and should be normalised via

$$\langle \bar{\mathbf{m}}_\omega, \mathbf{m}_\omega \rangle_{\text{nrf}} = 4i . \quad (\text{VI.3.14})$$

To understand the origin of the extra contribution in  $\mathcal{I}_{\text{nrf}}$ , one may recall that stray fields induce excitation in the medium,

$$\mathbf{M} \approx \mathbf{M}_{\text{nrf}} = -\mathcal{M}^{-1}\mathcal{Q}\mathbf{m} . \quad (\text{VI.3.15})$$

This leak affects the computation of scalar product and norm. (One may also notice that this term represents the  $Z_{\text{res}}$  factor in the self-energy expansion.) The discrete eigenmodes acquire a finite width due to the coupling to the incident waves described by the term  $\mathcal{K}\mathbf{M}_{\text{inc}}$  on the right-hand side. It is important to notice that the coupling does not include the contribution from the leaked modes: the matrix  $\mathcal{K}$  only includes the points within the resonator. Similarly, the scattered wave

$$\mathbf{M}_{\text{scat}} = \frac{1}{-i\omega\mathcal{I}_M - \mathcal{M}}\mathcal{Q}\mathbf{m} \quad (\text{VI.3.16})$$

is computed as if the mode were confined entirely within the resonator.

Working with a renormalised scalar product  $\mathcal{I}_{\text{nrf}}$  may be inconvenient. To get around this issue, one may change the basis in the mode space. This can be achieved by finding a transform  $\mathcal{S}_{\text{nrf}}$ ,

$$\mathbf{m}_\omega = \mathcal{S}_{\text{nrf}}\tilde{\mathbf{m}}_\omega , \quad (\text{VI.3.17})$$

that brings  $\mathcal{I}_{\text{nrf}}$  to the canonical form  $\mathcal{I}_R$ :

$$\mathcal{S}_{\text{nrf}}^T \mathcal{I}_{\text{nrf}} \mathcal{S}_{\text{nrf}} = \mathcal{I}_R . \quad (\text{VI.3.18})$$

(This procedure is equivalent to finding a symplectic basis in the space with symplectic structure  $\mathcal{I}_{\text{nrf}}$ .) This, however, would also change the form of  $\mathcal{R}_{\text{nrf}}$ . More importantly, the coupling to the incident waves takes a less trivial form:

$$(-i\omega\mathcal{I}_R - \mathcal{S}_{\text{nrf}}^T \mathcal{R}_{\text{nrf}} \mathcal{S}_{\text{nrf}}) \tilde{\mathbf{m}} = \mathcal{S}_{\text{nrf}}^T \mathcal{K}\mathbf{M}_{\text{inc}} , \quad (\text{VI.3.19})$$

Mode frequency, GHz	Mode 0	Mode 1	Mode 2
Isolated resonator	1.952	2.785	3.917
Near-field approximation	1.791	2.724	3.904
Transmission minima	1.770	2.640	3.832

Table VI.1: Eigenmode frequencies for an isolated resonator compared with those obtained by near-field approximation and extracted from transmission minima.

Dissipative linewidth, ns <sup>-1</sup>	Mode 0	Mode 1	Mode 2
$\Gamma_0^{(\text{nrf})}$	0.0223	0.0228	0.0278
$\Gamma_0^{(\text{bare})}$	0.0163	0.0184	0.0249

Table VI.2: Dissipative linewidths in the near-field approximation. Figures for an isolated resonator are given for comparison.

so that the coupling is to be computed with the matrix  $\tilde{\mathcal{K}} = \mathcal{S}_{\text{nrf}}^T \mathcal{K}$ . Similarly, the scattered wave is given by the matrix  $\tilde{\mathcal{Q}} = \mathcal{Q} \mathcal{S}_{\text{nrf}}$ . The matrix  $\mathcal{R}_{\text{nrf}}$  is also to be transformed to the new basis:  $\tilde{\mathcal{R}}_{\text{nrf}} = \mathcal{S}_{\text{nrf}}^T \mathcal{R}_{\text{nrf}} \mathcal{S}_{\text{nrf}}$ .

To test the usefulness of the near-field approximation, consider a YIG resonator of a rectangular cross-section 200 nm × 30 nm, infinite along the  $y$  direction magnetised by 5 mT field. We covered it by a 50 × 5 rectangular grid and first diagonalised the LLG eigensystem for the isolated resonator. The frequencies of the lowest three modes are listed in Table VI.1. We then considered its coupling to a 20 nm-thick YIG film positioned 10 nm away from the resonator. We have extended the film by 200 nm either side to account for stray fields, using 100 × 6 rectangular grid. The new frequencies are also listed in Table VI.1, and the respective linewidths are given in Table VI.2. One can see that the lowest mode is shifted downwards by a noticeable amount. The same is also true for other modes, but the shift is less significant. We then compared these results with positions of transmission minima. The latter were obtained by simulating a larger film with damping stubs at its ends and an excitation source (the data is shown in Fig. VI.7). One can see that the near-field approximation accounts for most of the shift in the frequency of the lowest mode, and gives reasonable estimates for other modes.

One may also examine the resulting stray fields, which are shown for the lowest-frequency mode in Fig. VI.5 as a pseudocolor plot, and in Fig. VI.6 as a quiver plot. We see that the dominant stray field comes from the horizontal component  $m_x$ : the stray field lines connect two magnetic charges at the opposite vertical edges of the resonator. The figures also show that the stray fields do not propagate far along the film, and there is no need to make the film much wider than the resonator.

One may also ask how the near-field contributions affect the distribution of magnetisation in general and ellipticity of the mode in particular. Fig. VI.8 shows precession ellipses without near-field effects, and with near-field effects included. The near-field coupling makes the precession ellipse more prolonged: for an isolated resonator ellipticity at the center of its bottom face is 0.42, while for a resonator coupled with the medium it is 0.37. This change is achieved mostly due to an increase in the  $m_x$  component, with insignificant reduction in the  $z$ -component.

This change, however, is insufficient to explain nearly-perfect forward-backward symmetry of transmission curves in Fig. VI.7 around 2 GHz frequency: ellipticity  $e_{xz} = 0.37$  would result in coupling asymmetry  $(1 - e_{xz})/(1 + e_{xz}) \approx 0.46$ .

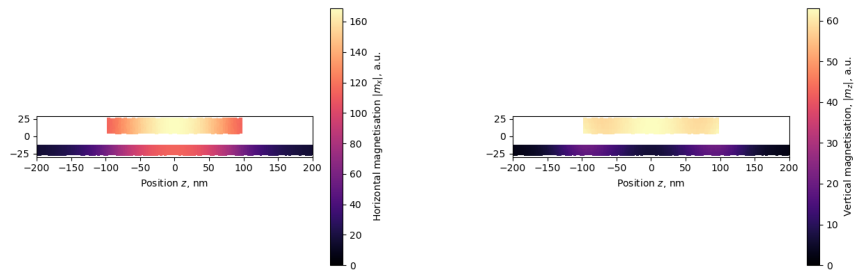


Figure VI.5: Distribution of magnetisation in the resonator and in the film for the lowest-frequency mode. Left panel: the horizontal component  $m_x$ . Right panel: the vertical component  $m_z$ .

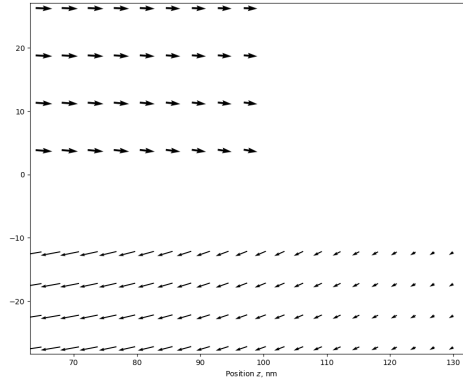


Figure VI.6: Orientation of the magnetisation in the resonator and in the film.

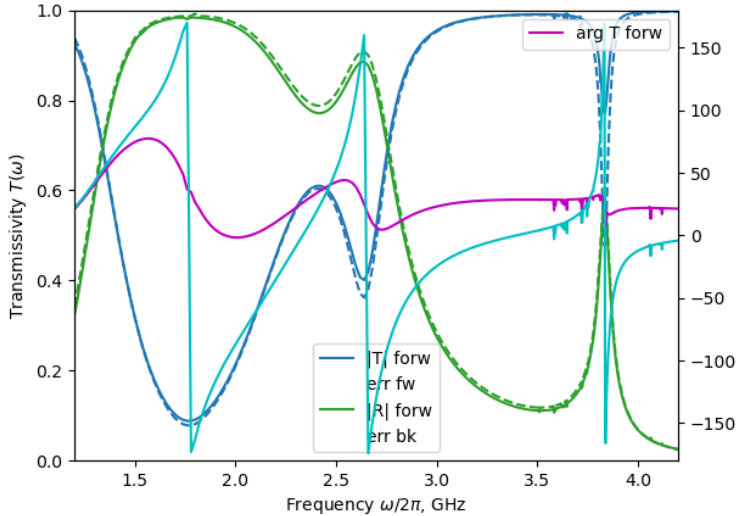


Figure VI.7: Transmission and reflection coefficients for a  $200 \times 30 \text{ nm}^2$  resonator coupled to a 20 nm-thick film at 10 nm. Solid lines represent transmission and reflection in the forward direction (left-to-right), the dashed lines represent the same quantity in the backward direction. One may see that the two lowest modes are not chiral, while the third mode is: the backward transmission minimum at 3.9 GHz is noticeably deeper. This indicates high ellipticity of precession in the lowest mode.

Radiative linewidth, $\text{ns}^{-1}$	Mode 0	Mode 1	Mode 2
$\Gamma_R^{(\text{nrf})}$	0.0390	$4.86 \cdot 10^{-5}$	$3.86 \cdot 10^{-4}$
$\Gamma_L^{(\text{nrf})}$	0.0987	$4.9 \cdot 10^{-4}$	$1.92 \cdot 10^{-4}$
$\Gamma_R^{(\text{bare})}$	0.027	$1.75 \cdot 10^{-5}$	$2.77 \cdot 10^{-4}$
$\Gamma_L^{(\text{bare})}$	0.087	$3.53 \cdot 10^{-4}$	$2.52 \cdot 10^{-4}$

Table VI.3: Radiative contributions to the linewidths  $\Gamma_R$  and  $\Gamma_L$  of the lowest resonant modes. The values in the top two rows are those obtained in the near-field approximation, while the values in the bottom rows represent the linewidths obtained assuming mode profile to be the same as in an isolated resonator.

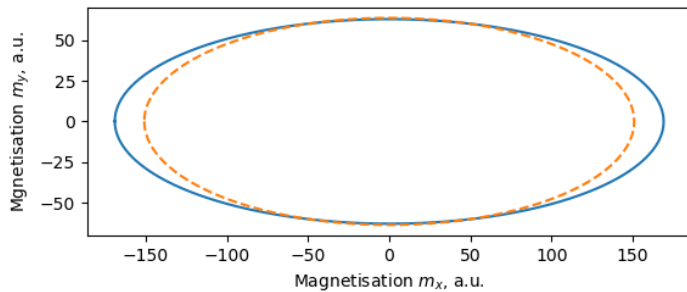


Figure VI.8: Precession ellipse at the midpoint of the bottom face of the resonator. The dashed line is the precession ellipse for an isolated resonator.

This, in turn, would yield nearly four-fold difference in the radiative linewidths  $\Gamma \propto |1 \pm e_{xz}|^2$ . The linewidths computed from the profiles of near-field modes, by weighting the profile with the evanescent potential  $\exp(-ikx - |k|z)$ , are listed in Table VI.3, together with their “bare” analogues . Examining this data reveals an asymmetry noticeably weaker than what one might expect from the ellipticity figures:  $\Gamma_L = 0.098 \text{ ns}^{-1}$ ,  $\Gamma_R = 0.039 \text{ ns}^{-1}$ . This difference can be explained by noticing phase variation that develops across the top edge of the resonator, as shown in Fig. VI.9. When the magnetisation distribution is convolved with a plane wave, the phase variation suppresses one of the overlaps and enhances the other, thus reducing the asymmetry between the modes. Still, it is clear from the given numbers that the behaviour of transmission near the 1.7 GHz resonance cannot be fully accounted for by a model involving a single resonant mode described in the near-field approximation.

To attempt more quantitative comparison of the resonance in transmission and reflection, we begin with the well-resolved resonance at 3.94 GHz. In Fig. VI.10, the scattering data is plotted against various approximation. First, the dash-dotted curves indicate the resonant curves obtained from the modes of an isolated resonator. One can see that both the positions and depths/heights of the resonant minima/maxima are changed by the coupling to the film. The dashed curves that

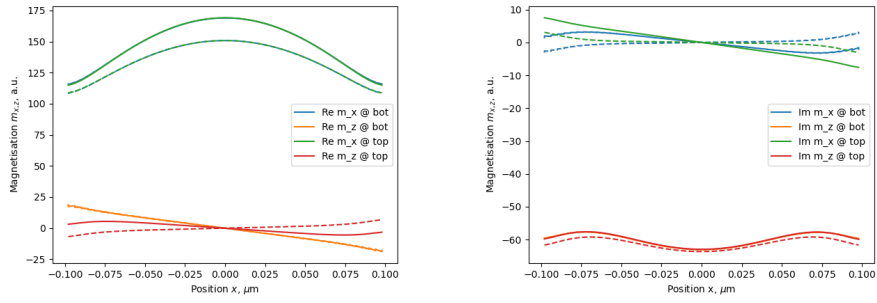


Figure VI.9: Distribution of the magnetisation in the resonator exhibits phase variation that is absent for an isolated resonator. This can be revealed by inspecting magnetisation components  $m_{x,z}$  on the top and bottom faces. Left panel: real part of  $m_x, m_z$ . Dashed curves illustrate the behaviour in an isolated resonator. Right panel: Imaginary part (i.e. the distribution a quarter period later).

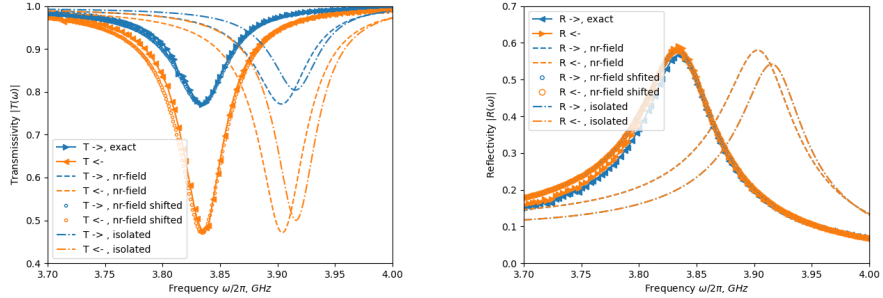


Figure VI.10: Transmission and reflection resonances near  $3.94 \text{ GHz}$  for  $s = 10 \text{ nm}$ . Left panel: transmissivity  $|T(\omega)|$ . Right panel: reflectivity  $|R(\omega)|$ . Blue curves indicate the incoming wave incident from the left, orange curves show the same quantity for the incidence from the right. Dashdot curves show the modes for an isolated resonator, and dashed curves show the near-field approximation. Near-field curves shifted to match the resonant minimum are shown as circles.

show the near-field approximation give correct depth, but do not fully account for the change in position. If one shifts the near-field curves to match the resonant minima (circles), one obtains a rather good description of the resonances. Thus, the deviation between the near-field results and the scattering data can be ascribed to the real part of self-energy, which is more pronounced at higher frequency.

To perform a similar comparison for the lowest-energy resonances at  $1.9 \text{ GHz}$  and  $2.7 \text{ GHz}$ , one may consider larger separations  $s = 100 \text{ nm}$  and  $s = 200 \text{ nm}$ , which makes them well-resolved. see Fig. VI.11. Both the near-field and isolated resonances reproduce the scattering data after a suitable frequency renormalisation. The resonance at  $2.77 \text{ GHz}$  exhibits a similar behaviour at  $s = 50 \text{ nm}$  and  $s = 100 \text{ nm}$ , see Fig. VI.12.

However, at smaller spacings the coupling between the resonant modes and the channel become strong, and resonances start to overlap. As can be seen from Fig. VI.13, at spacings  $s \leq 50 \text{ nm}$  the single-mode approximation does not properly capture the shape of the resonant curve near  $1.80 \text{ GHz}$ , even when the frequency dependence of the radiative linewidth is taken into account. Similarly, the resonance at  $2.77 \text{ GHz}$  becomes strongly coupled at  $s \leq 20 \text{ nm}$ , as can be seen from

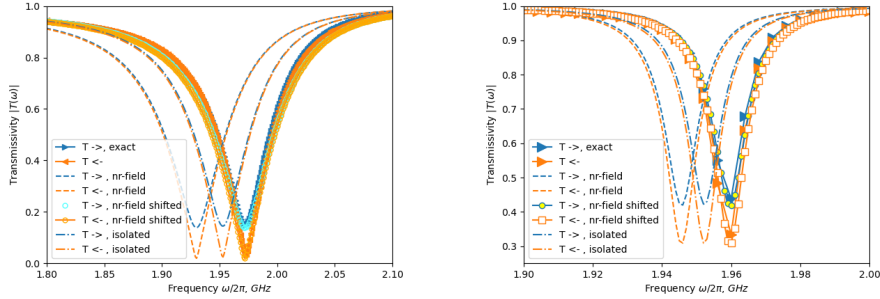


Figure VI.11: Transmission resonances near 1.94 GHz Left panel: transmissivity  $|T(\omega)|$  for  $s = 100$  nm. Right panel: the same for  $s = 200$  nm. Blue curves indicate the incoming wave incident from the left, orange curves show the same quantity for the incidence from the right. Dashdot curves show the modes for an isolated resonator, and dashed curves show the near-field approximation. Near-field curves shifted to match the resonant minimum are shown as circles.

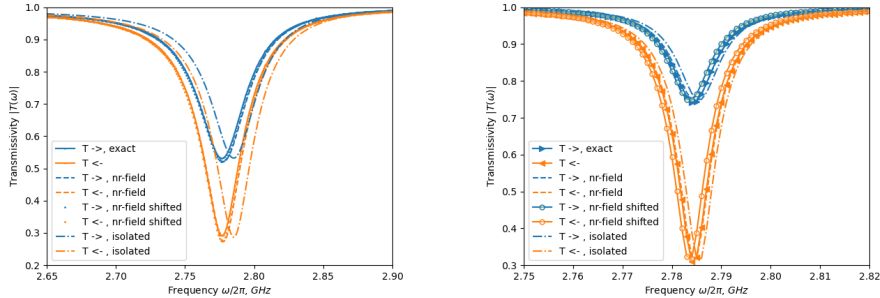


Figure VI.12: Transmission resonances near 2.77 GHz Left panel: transmissivity  $|T(\omega)|$  for  $s = 50$  nm. Right panel: the same for  $s = 100$  nm. Blue curves indicate the incoming wave incident from the left, orange curves show the same quantity for the incidence from the right. Dashdot curves show the modes for an isolated resonator, and dashed curves show the near-field approximation. Near-field curves shifted to match the resonant minimum are shown as circles.

Fig. VI.14. The resulting lineshapes exhibit notable asymmetry, and cannot be properly described in terms of single-mode resonant scattering. This can be explained by noticing that the resonant modes in this regime become overlapping, and the analysis in terms of single resonant mode is inadequate. Qualitatively, one may treat an overlap between the modes as a combination of the resonant scattering via the nearest mode, and off-resonant scattering via the other, which results in a Fano-like asymmetry.

To conclude, we see that the near-field approximation helps one to consider the coupling effect and to identify the leading trend arising from short-distance physics. It also gives somewhat satisfactory description of the lowest-energy modes, but might fail for higher-frequency modes. This can be explained by the effects of the residual self-energy

$$\hat{\Sigma}''(\omega) = \omega^2 \mathcal{K} \mathcal{M}^{-1} \mathcal{I}_M \frac{1}{-i\omega \mathcal{I}_M - \mathcal{M}} \mathcal{I}_M \mathcal{M}^{-1} \mathcal{Q} \quad (\text{VI.3.20})$$

that grows with frequency. Although the approximation by itself cannot explain all the anomalies in the transmission spectra, it is still a useful starting point: one may use it to identify the modes, compute their couplings and contributions to the

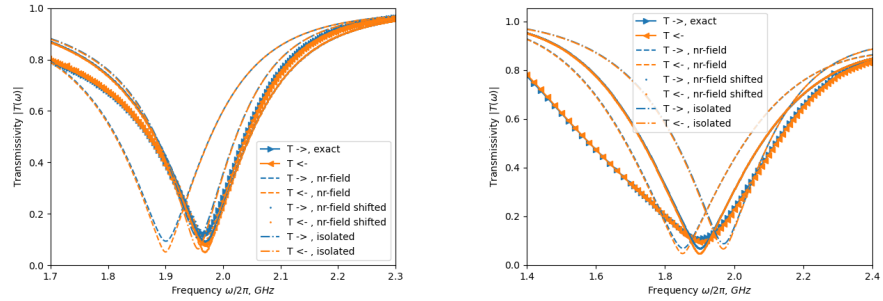


Figure VI.13: Transmission resonances near 1.80 GHz Left panel: transmissivity  $|T(\omega)|$  for  $s = 50 \text{ nm}$ . Right panel: the same for  $s = 20 \text{ nm}$ . Blue curves indicate the incoming wave incident from the left, orange curves show the same quantity for the incidence from the right. Dashdot curves show the modes for an isolated resonator. The dashed curves are computed with the help of the approximation described in the next section.

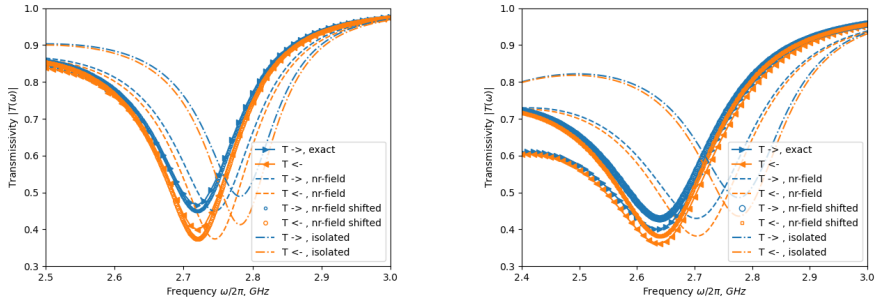


Figure VI.14: Transmission resonances near 2.70 GHz Left panel: transmissivity  $|T(\omega)|$  for  $s = 20 \text{ nm}$ . Right panel: the same for  $s = 10 \text{ nm}$ . Blue curves indicate the incoming wave incident from the left, orange curves show the same quantity for the incidence from the right. Dashdot curves show the modes for an isolated resonator, and dashed curves show the near-field approximation. Near-field curves shifted to match the resonant minimum are shown as circles.

residual self-energy to improve accuracy. The case of overlapping resonant modes, however, might require a separate treatment.

## VI.4 Multi-mode analysis

While in this memo we are mostly interested in the case of individual well-resolved resonant modes, this is sometimes not the case, as can be seen from Figs. VI.14, VI.13 and VI.7. The case of strongly coupled modes is of less practical relevance for the MANNGA project: such broad resonances do not exhibit field concentration, and reaching the nonlinear regime in such a settings may be noticeably harder. Yet, it is instructive to describe them quantitatively, to see which phenomena may become relevant in the strong-coupling regime.

Consider a resonator with several resonant modes with frequencies  $\Omega_a$  and widths  $\Gamma_a$  described by the respective variables  $\varphi_a(t)$ . (Here the index  $a$  enumerates the modes.) The Hamiltonian that couples these modes to propagating modes  $\psi_k$

can be taken in the form<sup>3</sup>

$$H = \dots + \sum_{\mathbf{k}, a} \Delta_{\mathbf{k}, a} \bar{\psi}_{\mathbf{k}} \varphi_a + \text{c.c.} \quad (\text{VI.4.1})$$

The respective equations of motion take the form

$$i\dot{\psi}_{\mathbf{k}} = (\omega_{\mathbf{k}} - i\gamma_{\mathbf{k}})\psi_{\mathbf{k}} + \sum_a \Delta_{\mathbf{k}, a} \varphi_a , \quad (\text{VI.4.2})$$

$$i\dot{\varphi}_a = (\Omega_a - i\Gamma_a)\varphi_a + \sum_{\mathbf{k}} \bar{\Delta}_{\mathbf{k}, a} \psi_{\mathbf{k}} . \quad (\text{VI.4.3})$$

One can eliminate the bulk modes  $\psi_{\mathbf{k}}$  as before, by introducing the self-energy operator

$$\Sigma_{ab}(\omega) = \sum_{\mathbf{k}} \frac{\bar{\Delta}_{\mathbf{k}, a} \Delta_{\mathbf{k}, b}}{\omega - \omega_{\mathbf{k}} + i\gamma_{\mathbf{k}}} \quad (\text{VI.4.4})$$

and rewriting the equations for the local modes in the form

$$[\omega \mathbb{1}_{a,b} - (\Omega_a - i\Gamma_a) \mathbb{1}_{a,b} - \Sigma_{a,b}(\omega)] \varphi_a = \bar{\Delta}_{\text{inc}, a} A_{\text{inc}} , \quad (\text{VI.4.5})$$

where  $A_{\text{inc}}$  is the amplitude of the incident wave. Thus, the dynamics of the mode is described by the self-energy operator that acts as a matrix  $\hat{\Sigma}(\omega)$  in the mode space. The solution can be obtained by inverting the respective matrix. It can be written symbolically as

$$\varphi_a = [\omega \hat{\mathbb{1}} - \hat{\Omega}_0 + i\hat{\Gamma}_0 - \hat{\Sigma}(\omega)]^{-1} \bar{\Delta}_{\text{inc}, a} A_{\text{inc}} , \quad (\text{VI.4.6})$$

where the matrices  $\hat{\Omega}_0$  and  $\hat{\Gamma}_0$  have a diagonal form:

$$\hat{\Omega}_0 = \begin{bmatrix} \Omega_a & & \\ & \Omega_b & \\ & & \ddots \end{bmatrix} , \quad \hat{\Gamma}_0 = \begin{bmatrix} \Gamma_a & & \\ & \Gamma_b & \\ & & \ddots \end{bmatrix} . \quad (\text{VI.4.7})$$

The scattered wave can be written in the form

$$\psi_{\mathbf{k}}^{(\text{scat})} = G_{\mathbf{k}}(\omega) \hat{\Delta}^T \cdot [\omega \hat{\mathbb{1}} - \hat{\Omega}_0 + i\hat{\Gamma}_0 - \hat{\Sigma}(\omega)]^{-1} \cdot \bar{\Delta}_{\text{inc}} A_{\text{inc}} , \quad (\text{VI.4.8})$$

where  $\hat{\Delta}^T$  is the transposed vector of couplings. In particular, in one dimension, one can obtain the transmission and reflection coefficients

$$T(L \rightarrow R) = 1 - \frac{i}{v_R} \hat{\Delta}_R^T \cdot [\omega \hat{\mathbb{1}} - \hat{\Omega}_0 + i\hat{\Gamma}_0 - \hat{\Sigma}(\omega)]^{-1} \cdot \bar{\Delta}_R , \quad (\text{VI.4.9})$$

$$R(L \rightarrow L) = -\frac{i}{\sqrt{v_R v_L}} \hat{\Delta}_L^T \cdot [\omega \hat{\mathbb{1}} - \hat{\Omega}_0 + i\hat{\Gamma}_0 - \hat{\Sigma}(\omega)]^{-1} \cdot \bar{\Delta}_R ,$$

where  $\Delta_L$  and  $\Delta_R$  are the vectors formed by the hybridisation coefficients for the left- and right-going waves.

<sup>3</sup> The equations stated in this section neglect the effect of Gilbert damping on the coupling between the modes, and this can sometimes violate energy conservation. This can be improved by replacing all occurrences of  $\bar{\Delta}$  by a different coupling  $\tilde{\Delta}$  in which the complex-conjugate magnetisation  $\tilde{\mathbf{m}}_a$  is replaced with the dual vector  $\tilde{\mathbf{m}}_a$  introduced in Sec. VI.2.

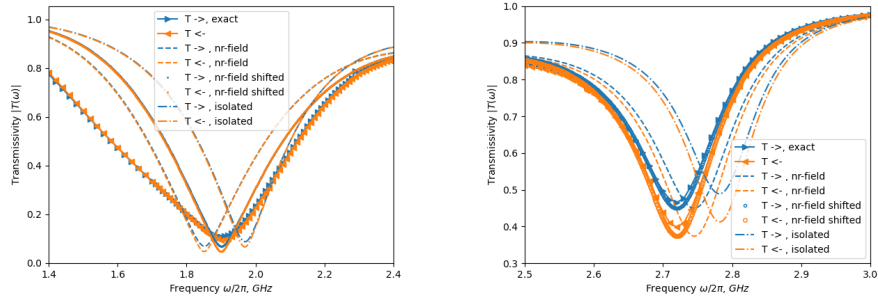


Figure VI.15: Transmission resonances for  $s = 20 \text{ nm}$ . Left panel: transmissivity  $|T(\omega)|$  near the 1.80 GHz mode. Right panel: the same for the 2.70 GHz mode. Blue curves indicate the incoming wave incident from the left, orange curves show the same quantity for the incidence from the right. Dashdot curves show the modes for an isolated resonator, and dashed curves show the calculation in which off-diagonal elements  $\Gamma_{ab}(\omega)$  are included.

As in the single-mode case, there are two contributions to the self-energy part

$$\Sigma_{ab}(\omega) = \text{Re } \Sigma_{ab}(\omega) - i\Gamma_{ab}(\omega) . \quad (\text{VI.4.10})$$

The radiative contribution  $-i\Gamma_{a,b}(\omega)$  of the pole at  $\omega = \omega_k$  yields the linewidth, and the off-shell contribution  $\text{Re } \Sigma_{ab}(\omega)$  describes the shift of the resonant frequencies. The radiative term can be written in the form

$$\Gamma_{ab}^{(\text{rad})}(\omega) = \pi \sum_{\mathbf{k}} \bar{\Delta}_{\mathbf{k},a} \Delta_{\mathbf{k},b} \delta(\omega - \omega_{\mathbf{k}}) . \quad (\text{VI.4.11})$$

It has the property of Hermitianess,  $\Gamma_{a,b}(\omega) = \bar{\Gamma}_{b,a}(\omega)$ , so that the contribution  $-i\Gamma_{a,b}(\omega)$  is antihermitian. In general, it has off-diagonal elements that describe mutual influence of the modes due to the radiative friction. The real part can be linked to the imaginary part via the dispersion relation:

$$\text{Re } \Sigma_{a,b}(\omega) = \int_0^\infty \frac{d\omega'}{\pi} \frac{\omega^2}{\omega'^2(\omega' - \omega)} \Gamma_{a,b}(\omega') . \quad (\text{VI.4.12})$$

(Here we assumed that the near-field contribution is already subtracted.) Unlike the single-mode case, when the real part of the self-energy can be incorporated into the definition of the eigenfrequency  $\Omega_0$ , in the case of multiple modes one has to include possible hybridisation between the modes described by the off-diagonal elements of  $\text{Re } \Sigma_{a,b}(\omega)$ .

Because of the difficulty of computing  $\text{Re } \Sigma(\omega)$ , one may attempt to drop it, and to treat the coupling between the modes entirely in terms of the radiative friction  $\Gamma_{a,b}(\omega)$ . An attempt of such a comparison is made in Fig. VI.15 for the two lowest modes at  $s = 20 \text{ nm}$ . One can see that the multimode approximation shown with dashed lines gives the correct trend in the overlap between the modes, but does not fully describe the overlapping behaviour. The agreement is significantly improved if  $\text{Re } \Sigma_{ab}(\omega)$  is included in the calculation, as shown in the left panel of Fig. ???. However, when  $s$  is further decreased to 10 nm, the difference between the multimode result and the transmission curves is again noticeable.

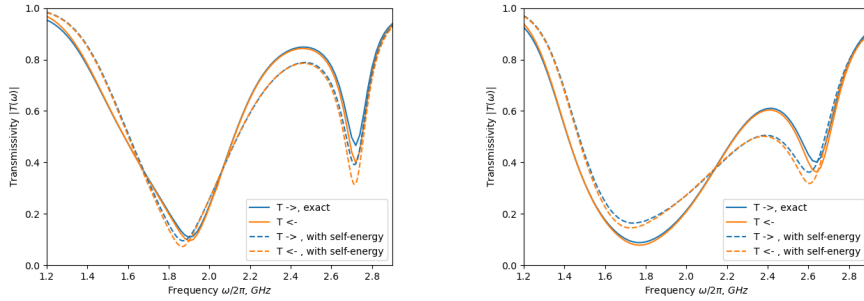


Figure VI.16: Transmission resonances for  $s = 20 \text{ nm}$  Left panel: transmissivity  $|T(\omega)|$  for  $s = 10 \text{ nm}$ . Right panel: the same for  $s = 10 \text{ nm}$ . Blue curves indicate the incoming wave incident from the left, orange curves show the same quantity for the incidence from the right. Dashdot curves show the modes for an isolated resonator, and dashed curves show the calculation in which off-diagonal elements  $\Gamma_{ab}(\omega)$  are included.

To explain this, one may generalise the above analysis to include off-resonant contributions. The most general Hamiltonian that couples the local modes to the propagating modes is of the form

$$H = \dots + \sum_{\mathbf{k},a} \Delta_{\mathbf{k},a} \bar{\psi}_{\mathbf{k}} \varphi_a + \sum_{\mathbf{k},a} \Delta'_{\mathbf{k},a} \psi_{\mathbf{k}} \varphi_a + \text{c.c.} \quad (\text{VI.4.13})$$

The terms of the form  $\propto \psi_{\mathbf{k}} \varphi_a$  and  $\propto \bar{\psi}_{\mathbf{k}} \bar{\varphi}_a$  are not resonant, as the frequencies in the two modes do not match. Yet, they may become important in the strong-coupling regime. As will be seen from the equations below, the effect of these terms is to intermix  $\varphi_a$  and  $\bar{\varphi}_a$ , which describes how the coupling between the modes alter their ellipticities. To describe the behaviour in this regime, it may be helpful to consider  $\bar{\psi}_{\mathbf{k}}$  as formally independent of  $\psi_{\mathbf{k}}$ , as well as  $\bar{\varphi}_a$  independent of  $\varphi_a$ . The equations of motion for the propagating modes  $\psi_{\mathbf{k}}, \bar{\psi}_{\mathbf{k}}$  take the form<sup>4</sup>

$$\begin{aligned} i\dot{\psi}_{\mathbf{k}} &= (\omega_{\mathbf{k}} - i\gamma_{\mathbf{k}})\psi_{\mathbf{k}} + \sum_b \Delta_{\mathbf{k},b} \varphi_b + \sum_b \bar{\Delta}'_{\mathbf{k},b} \bar{\varphi}_b , \\ i\dot{\bar{\psi}}_{\mathbf{k}} &= -(\omega_{\mathbf{k}} + i\gamma_{\mathbf{k}})\bar{\psi}_{\mathbf{k}} - \sum_b \bar{\Delta}_{\mathbf{k},b} \bar{\varphi}_b - \sum_b \Delta'_{\mathbf{k},b} \varphi_b . \end{aligned} \quad (\text{VI.4.14})$$

The equations for the local modes  $\varphi_a, \bar{\varphi}_a$  have a similar structure<sup>5</sup>:

$$\begin{aligned} i\dot{\varphi}_a &= (\Omega_a - i\Gamma_a)\varphi_a + \sum_{\mathbf{k}} \bar{\Delta}_{\mathbf{k},a} \psi_{\mathbf{k}} + \sum_b \bar{\Delta}'_{\mathbf{k},a} \bar{\psi}_{\mathbf{k}} , \\ i\dot{\bar{\varphi}}_a &= -(\Omega_a + i\Gamma_a)\bar{\varphi}_a - \sum_{\mathbf{k}} \Delta_{\mathbf{k},a} \bar{\psi}_{\mathbf{k}} - \sum_b \Delta'_{\mathbf{k},a} \psi_{\mathbf{k}} . \end{aligned} \quad (\text{VI.4.15})$$

Some terms here oscillate with positive frequency,  $\Omega_a$  or  $\omega_{\mathbf{k}}$ , while the others oscillate with negative frequency. The mixing, in general, yields various oscillating contributions in the solution. Yet it suffices to assume that all the quantities here oscillate at the same frequency  $\omega > 0$ . The mode  $\psi_{\mathbf{k}}$  is then a propagating mode,

<sup>4</sup> The couplings  $\bar{\Delta}_{\mathbf{k}}$  and  $\bar{\Delta}'_{\mathbf{k}}$  here should be understood as complex-conjugates of the couplings  $\Delta_{\mathbf{k}}$  and  $\Delta'_{\mathbf{k}}$ , even in the presence of damping.

<sup>5</sup> In these equations,  $\bar{\Delta}_{\mathbf{k}}$  and  $\bar{\Delta}'_{\mathbf{k}}$  should be replaced with the dual-mode couplings  $\tilde{\Delta}_{\mathbf{k}}$  and  $\tilde{\Delta}'_{\mathbf{k}}$  if the effects of damping are significant.

while its counterpart  $\bar{\psi}_k$  is not, as there is no resonant pole in  $(\omega + \omega_k)^{-1}$ , and  $\bar{\psi}_k$  is a purely evanescent contribution. A far-away source therefore emits only  $\psi_k$ , and the scattered wave is also given by  $\psi_k$ . The latter receives the contribution from both  $\varphi_a$  and  $\bar{\varphi}_a$ :

$$\psi_k^{(\text{scat})} = G_k(\omega) \sum_b [\Delta_{k,b} \varphi_b + \bar{\Delta}'_{k,b} \bar{\varphi}_b] . \quad (\text{VI.4.16})$$

Eliminating the scattered wave  $\psi_k$  and the near-field contribution

$$\bar{\psi}_k = -\frac{1}{\omega + \omega_k} \sum_b [\bar{\Delta}_{k,b} \bar{\varphi}_b + \Delta'_{k,b} \varphi_b] , \quad (\text{VI.4.17})$$

we write the dynamics of the modes  $\varphi_a$  and  $\bar{\varphi}_a$  as follows:

$$[\omega \mathbb{1} - \hat{\Omega}_0 + i\hat{\Gamma}_0 - \hat{\Sigma}_{++}(\omega)] \boldsymbol{\varphi} - \hat{\Sigma}_{+-}(\omega) \bar{\boldsymbol{\varphi}} = \bar{\boldsymbol{\Delta}}_{\text{inc}} A_{\text{inc}} , \quad (\text{VI.4.18})$$

$$[\omega \mathbb{1} + \hat{\Omega}_0 + i\hat{\Gamma}_0 + \hat{\Sigma}_{--}(\omega)] \bar{\boldsymbol{\varphi}} + \hat{\Sigma}_{-+}(\omega) \boldsymbol{\varphi} = -\boldsymbol{\Delta}'_{\text{inc}} A_{\text{inc}} , \quad (\text{VI.4.19})$$

with the following self-energy operator:

$$\Sigma_{++,ab}(\omega) = \sum_k \frac{\bar{\Delta}_{k,a} \Delta_{k,b}}{\omega - \omega_k + i\gamma_k} - \sum_k \frac{\bar{\Delta}'_{k,a} \Delta'_{k,b}}{\omega + \omega_k} , \quad (\text{VI.4.20})$$

$$\Sigma_{--,ab}(\omega) = \sum_k \frac{\Delta'_{k,a} \bar{\Delta}'_{k,b}}{\omega - \omega_k + i\gamma_k} - \sum_k \frac{\Delta_{k,a} \bar{\Delta}_{k,b}}{\omega + \omega_k} , \quad (\text{VI.4.21})$$

$$\Sigma_{+-,ab}(\omega) = \sum_k \frac{\bar{\Delta}_{k,a} \bar{\Delta}'_{k,b}}{\omega - \omega_k + i\gamma_k} - \sum_k \frac{\bar{\Delta}'_{k,a} \bar{\Delta}_{k,b}}{\omega + \omega_k} , \quad (\text{VI.4.22})$$

$$\Sigma_{-+,ab}(\omega) = \sum_k \frac{\Delta'_{k,a} \Delta_{k,b}}{\omega - \omega_k + i\gamma_k} - \sum_k \frac{\Delta_{k,a} \Delta'_{k,b}}{\omega + \omega_k} . \quad (\text{VI.4.23})$$

The resulting system of equations can be also stated in the matrix form

$$\mathcal{P} \begin{bmatrix} \boldsymbol{\varphi} \\ \bar{\boldsymbol{\varphi}} \end{bmatrix} = A_{\text{inc}} \begin{bmatrix} \bar{\boldsymbol{\Delta}}_{\text{inc}} \\ -\boldsymbol{\Delta}'_{\text{inc}} \end{bmatrix} , \quad (\text{VI.4.24})$$

with

$$\mathcal{P} \equiv \begin{bmatrix} \omega - \hat{\Omega}_0 + i\hat{\Gamma}_0 - \hat{\Sigma}_{++}(\omega) & -\hat{\Sigma}_{+-}(\omega) \\ \hat{\Sigma}_{-+} & \omega + \hat{\Omega}_0 + i\hat{\Gamma}_0 + \hat{\Sigma}_{--}(\omega) \end{bmatrix} . \quad (\text{VI.4.25})$$

The matrix  $\mathcal{P}$  operates in the  $2N$ -dimensional space formed by  $\varphi_a$  and  $\bar{\varphi}_a$ . The scattered wave can be obtained by inverting the matrix  $\mathcal{P}$ :

$$\psi_k^{(\text{scat})} = A_{\text{inc}} G_k(\omega) [\boldsymbol{\Delta}_k \quad \bar{\boldsymbol{\Delta}}'_k] \cdot \mathcal{P}^{-1} \cdot \begin{bmatrix} \bar{\boldsymbol{\Delta}}_{\text{inc}} \\ -\boldsymbol{\Delta}'_{\text{inc}} \end{bmatrix} . \quad (\text{VI.4.26})$$

In one dimension, this reduces to the expressions for transmission and reflection:

$$T(L \rightarrow R) = 1 - \frac{i}{v_R} [\Delta_R \quad \bar{\Delta}'_R] \cdot \mathcal{P}^{-1} \cdot \begin{bmatrix} \bar{\boldsymbol{\Delta}}_R \\ -\boldsymbol{\Delta}'_R \end{bmatrix} , \quad (\text{VI.4.27})$$

$$R(L \rightarrow L) = -\frac{i}{\sqrt{v_R v_L}} [\Delta_L \quad \bar{\Delta}'_L] \cdot \mathcal{P}^{-1} \cdot \begin{bmatrix} \bar{\boldsymbol{\Delta}}_R \\ -\boldsymbol{\Delta}'_R \end{bmatrix} , \quad \text{etc}$$

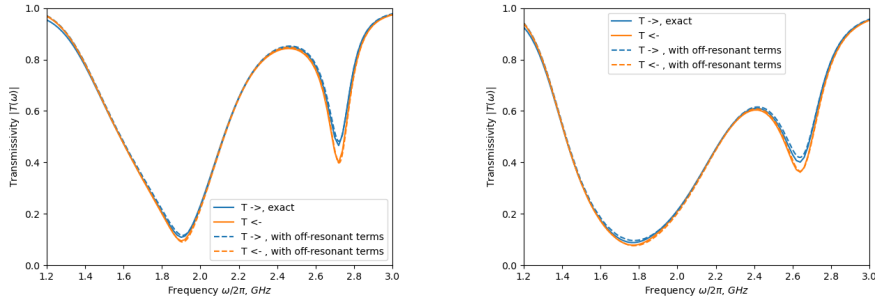


Figure VI.17: Transmission resonances for  $s = 20 \text{ nm}$  Left panel: transmissivity  $|T(\omega)|$  for  $s = 10 \text{ nm}$ . Right panel: the same for  $s = 10 \text{ nm}$ . Blue curves indicate the incoming wave incident from the left, orange curves show the same quantity for the incidence from the right. Dashdot curves show the modes for an isolated resonator, and dashed curves show the calculation that includes cross-talk between the resonant modes via  $\Gamma_{ab}(\omega)$  and  $\text{Re } \Sigma_{ab}(\omega)$ , as well as the off-resonant contributions involving  $\Delta'_{k,a}$ .

Such an approach gives more accurate results in the strong-coupling regime.

Computing self-energies (??)–(??) involves handling the pole at  $\omega_k = \omega$ . This can be performed by first tabulating the “generalised linewidths”

$$\Gamma_{++,ab}(\omega) \equiv \Gamma_{\text{rad},ab}(\omega) = \sum_{d=R,L} \bar{\Delta}_{d,a}(\omega) \Delta_{d,b}(\omega) , \quad (\text{VI.4.28})$$

$$\Gamma_{--,ab}(\omega) \equiv \sum_{d=R,L} \Delta'_{d,a}(\omega) \bar{\Delta}'_{d,b}(\omega) , \quad \Gamma_{+-,ab}(\omega) \equiv \Gamma_{\text{rad},ab}(\omega) \sum_{d=R,L} \bar{\Delta}_{d,a}(\omega) \Delta'_{d,b}(\omega) , \quad (\text{VI.4.29})$$

$$\Gamma_{-+,ab}(\omega) \equiv \sum_{d=R,L} \Delta'_{d,a}(\omega) \Delta_{d,b}(\omega) , \quad (\text{VI.4.30})$$

where  $\Delta_{R,L}(\omega)$  is evaluated at the pole, on the respective dispersion branch. Then, the self-energy can be found via

$$\Sigma_{++,ab}(\omega) = -i\Gamma_{++,ab}(\omega) + \int \frac{d\omega' \Gamma_{++,ab}(\omega')}{\omega - \omega'} - \sum_{\mathbf{k}} \frac{\bar{\Delta}'_{\mathbf{k},a} \Delta'_{\mathbf{k},b}}{\omega + \omega_{\mathbf{k}}} , \quad (\text{VI.4.31})$$

$$\Sigma_{--,ab}(\omega) = -i\Gamma_{--,ab}(\omega) + \int \frac{d\omega' \Gamma_{--,ab}(\omega')}{\omega - \omega'} - \sum_{\mathbf{k}} \frac{\Delta_{\mathbf{k},a} \bar{\Delta}_{\mathbf{k},b}}{\omega + \omega_{\mathbf{k}}} , \quad (\text{VI.4.32})$$

$$(\text{VI.4.33})$$

etc. The frequency integral here is interpreted as principal value:

$$\int d\omega' [\dots] = \lim_{\epsilon \rightarrow 0} \left[ \int_{-\infty}^{\omega - \epsilon} d\omega' [\dots] + \int_{\omega + \epsilon}^{\infty} d\omega' [\dots] \right] .$$

Comparison between Eq. ?? and the simulation is attempted in Fig. ???. One can see that including both the “active” and “reactive” cross-talk, together with the off-resonant contribution, yields a satisfactory quantitative description of one-dimensional scattering for overlapping modes. This indicates the role of the off-resonant couplings in the strong-coupling regime.

Mode	$s = \infty$	20 nm	10 nm	5 nm
0	1.79	1.77	1.77	1.76
1	3.63	3.47	3.31	3.06
2	5.57	4.78	4.16	3.83
3	7.60	6.24	5.79	5.46
4		8.24	7.49	6.79
5			9.06	8.57

Table VI.4: Frequencies (in GHz) of the lowest-lying modes for various spacings  $s$  between the resonator and the film.

## VI.5 Semi-realistic case: a large synthetic antiferromagnet

Let us employ the theory we have developed to compute scattering off a synthetic antiferromagnet (sAFM). Consider an antiferromagnet formed by 20 nm thick layer of negatively magnetised permalloy ( $M_s = -800 \text{ kA/m}$ ,  $A_{\text{ex}} = 13 \text{ pJ/m}$ ,  $\alpha = 5 \cdot 10^{-3}$ ) with 15 nm thick layer of positively magnetised CoFeB ( $M_s = 1150 \text{ kA/m}$ ,  $A_{\text{ex}} = 16 \text{ pJ/m}$ ,  $\alpha = 5 \cdot 10^{-3}$ ) on top, biased by 5 mT field. The propagating medium is a YIG 50 nm film ( $M_s = 140 \text{ kA/m}$ ,  $A_{\text{ex}} = 3.5 \text{ pJ/m}$ ,  $\alpha = 10^{-3}$ ), biased by the same field. In the propagation plane, the sAFM geometry is  $600 \text{ nm} \times 300 \text{ nm}$ . The two ferromagnets in the sAFM are coupled by the RKKY interaction with the coupling strength  $1.5 \text{ mJ/m}$ .

The isolated system exhibits its lowest resonances at four frequencies: 1.79 GHz, 3.63 GHz, 5.57 GHz, and 7.60 GHz. The respective intrinsic widths of the modes are  $0.282 \text{ ns}^{-1}$ ,  $0.302 \text{ ns}^{-1}$ ,  $0.346 \text{ ns}^{-1}$  and  $0.390 \text{ ns}^{-1}$ . When the resonator is coupled to the film, the near-field approximation yields the frequencies given in Table ???. One can see that the low-frequency modes are weakly affected by the coupling, while the higher-frequency modes are shifted down quite significantly.

This behaviour is contrary to the intuition one may acquire by looking at the coupling of uniform modes, such as those analysed in the previous sections. It can be explained by inspecting magnetisation profiles in the modes. The lowest-lying mode at 1.8 GHz is a uniform antiferromagnetic mode, as can be seen from its real and imaginary components shown in Fig. ???. Such a magnetisation distribution is nearly compensated and does not generate a strong field. In contrast to this, the first-excited mode at  $\gtrsim 3 \text{ GHz}$  exhibits a node in the middle, as shown in Fig. ?? and the associated magnetic charge induces a field in the film. One may also notice that at higher frequencies the factor  $\exp(-k_\omega z)$  suppresses the contribution of the top layer of sAFM, and the field becomes uncompensated.

An interesting feature of the resonant modes in this structure is the phase variation shown in Fig. ???. It indicates change in orientation of precession ellipse between the left and right edge of the resonator.

In what follows, we shall treat the two modes as separate resonances, neglecting their possible cross-couplings. The respective radiative linewidths are shown in Fig. ???. One can see that the 3 GHz mode is a far more efficient radiator. One may also see that the 300 nm length of the resonator suppresses radiation at  $\sim 3 \text{ GHz}$ , due to the full-wave condition. Total scattering and absorption cross-sections are shown in Fig. ???. For the lowest mode, the cross-sections exhibit symmetric

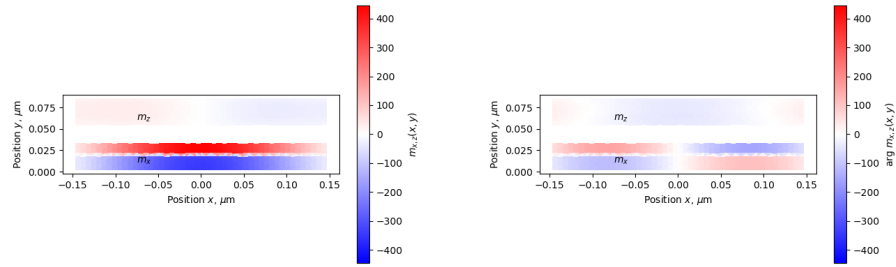


Figure VI.18: Real and imaginary components of magnetisation in the lowest-lying mode for  $s = 10\text{ nm}$ . Left panel:  $\text{Re } m_{x,z}$ . Right panel:  $\text{Im } m_{x,z}$ .

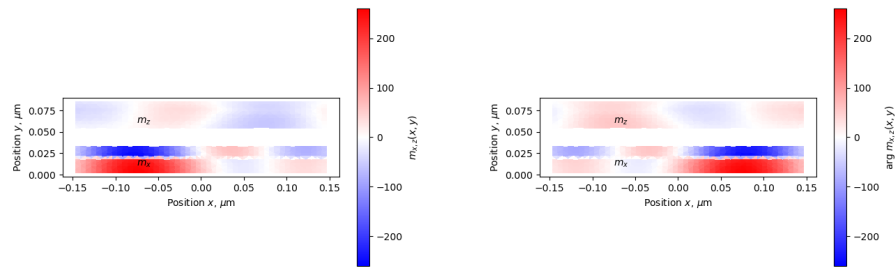


Figure VI.19: Real and imaginary components of magnetisation in the first-excited mode for  $s = 10\text{ nm}$ . Left panel:  $\text{Re } m_{x,z}$ . Right panel:  $\text{Im } m_{x,z}$ .

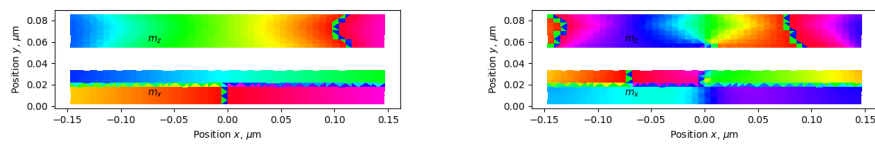


Figure VI.20: Oscillation phase for  $m_x$  and  $m_z$  in the two lowest modes. Left panel: the lowest-lying mode at  $\approx 1.80\text{ GHz}$ . Right panel: the first-excited mode at  $\gtrsim 3\text{ GHz}$ .

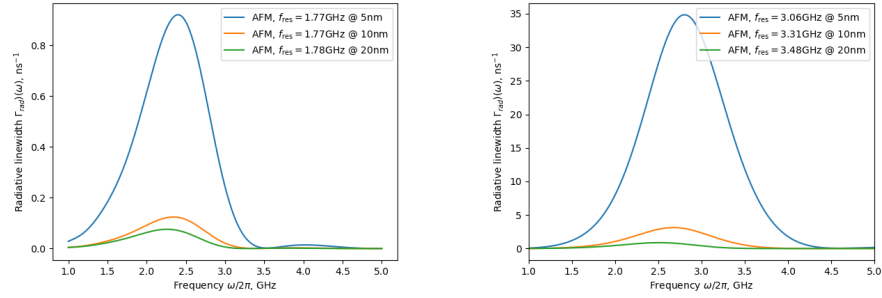


Figure VI.21: Radiative linewidth as a function of frequency  $\omega$ . Left panel: the lowest-lying mode at  $\approx 1.8$  GHz. Right panel: the first-excited mode at  $\gtrsim 3$  GHz.

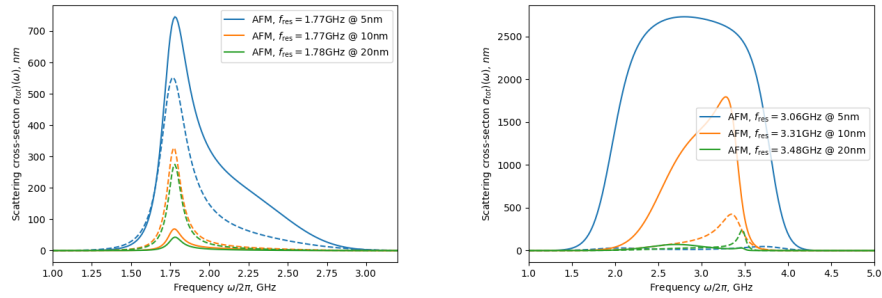


Figure VI.22: Scattering and absorption cross-sections as a function of frequency  $\omega$  are shown as the solid line (scattering) and dashed line (absorption) of the respective colour. Left panel: the lowest-lying mode at  $\approx 1.8$  GHz. Right panel: the first-excited mode at  $\gtrsim 3$  GHz.

resonant peaks. But for the first excited mode, the resonant peaks are rather broad and asymmetric. This is related to two effects. First, the radiative linewidth varies significantly across the resonance, due to the full-wave condition between its edges and the cancellation of the outgoing radiation by destructive interference. But one may also see a nearly saturated behaviour at lower frequencies for  $s = 5$  nm. This is the manifestation of unitary limit of scattering: when the coupling between the local mode and the propagating modes becomes too strong, the total cross-section is saturated at  $2/v\Gamma_{\text{res}}^{-1}d\Gamma_{\text{res}}/d\theta$ .

The angular distribution of the coupling for the 1.8 GHz mode is shown in Fig. ???. The emission occurs predominantly in the forward direction, and is nearly flat for propagation angles  $\alpha \lesssim 20^\circ$ . For the 3 GHz mode, Fig. ?? the distribution features a rather narrow forward peak, due to the Fraunhofer diffraction. The respective real-angle distribution is even more narrow.

The respective behaviour of the scattered wave in the  $k$ -space is shown in Figs. ?? and ???. One can clearly see weak backscattering for the lowest-lying mode, and its suppression in the first-excited mode. For the 3 GHz mode, one may also see clearly the minima due to Fraunhofer diffraction.

As the scattering occurs predominantly at zero angle, one may also inspect the differential scattering cross-section for  $\theta = 0$ . (Note this is different from  $\alpha = 0$ , as the contributions for  $\alpha = 0$  may arise from several segments of the constant frequency contour.) Its frequency dependence is shown in Fig. ???. The non-resonant singularity at  $f \approx 3.5$  GHz is due to flattening of the contour  $k_\omega(\theta)$ . One

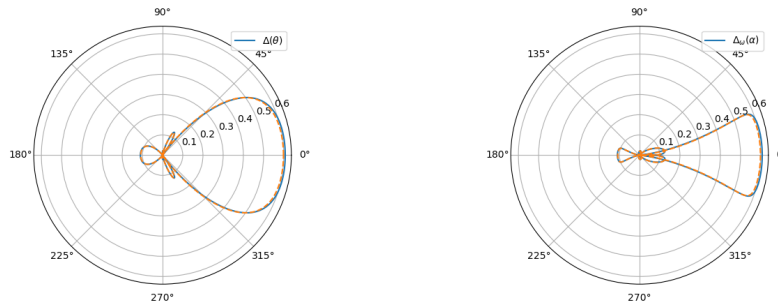


Figure VI.23: Angular distribution of the resonant coupling at  $f = 1.8$  GHz,  $s = 5$  nm. Left panel: directivity  $|\Delta(\theta)|$  in the  $\mathbf{k}$ -space. Right panel: directivity  $|\Delta(\alpha)|$  in the real space.

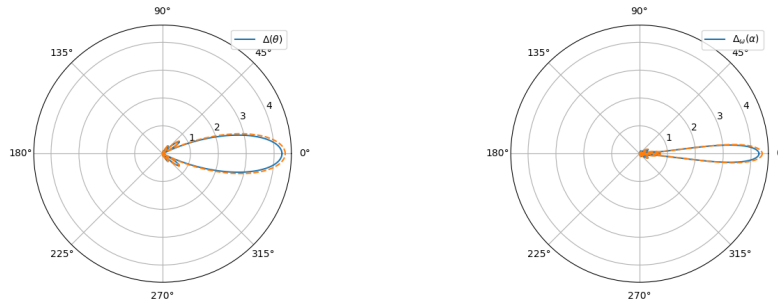


Figure VI.24: Angular distribution of the resonant coupling at  $f = 3$  GHz,  $s = 5$  nm. Left panel: directivity  $|\Delta(\theta)|$  in the  $\mathbf{k}$ -space. Right panel: directivity  $|\Delta(\alpha)|$  in the real space.

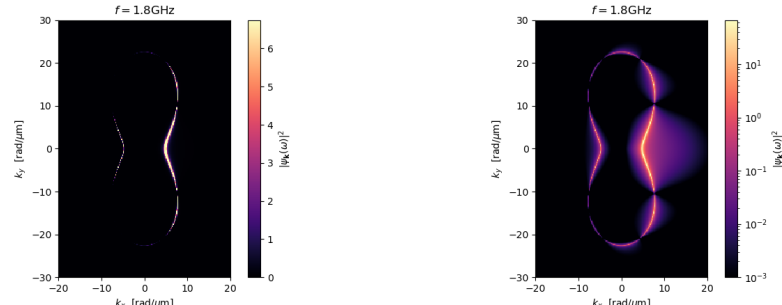


Figure VI.25: Distribution of the scattered intensity in the  $\mathbf{k}$ -space for  $f = 1.8$  GHz,  $s = 5$  nm. Left panel: linear pseudocolor scale. Right panel: log scale.

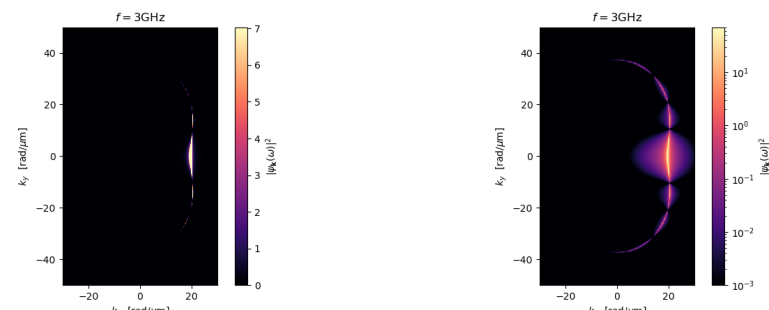


Figure VI.26: Distribution of the scattered intensity in the  $\mathbf{k}$ -space for  $f = 3$  GHz,  $s = 5$  nm. Left panel: linear pseudocolor scale. Right panel: log scale.

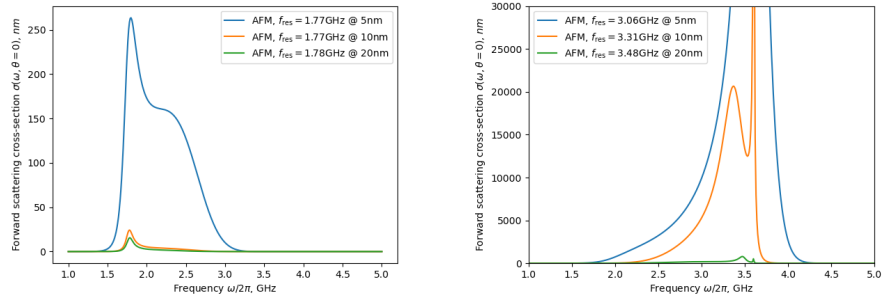


Figure VI.27: Frequency dependence of the forward scattering cross-section for both resonant modes.

Spacing $s$	Mode 0, GHz	Mode 1, GHz
$\infty$	4.10	8.57
30 nm	4.05	8.69
25 nm	4.04	8.71
20 nm	4.03	8.73
15 nm	4.02	8.74
10 nm	4.00	8.75
5 nm	3.97	8.75

Table VI.5: Resonant frequencies from the near-field approximation for a  $120 \times 200$  nm synthetic antiferromagnet with net magnetisation antiparallel to that in the film.

may notice that this singularity obscures the behaviour of the cross-section for the first excited mode at  $s = 5$  nm

## VI.6 The case of a smaller resonator

Let us now see how the dimensions of the resonator affect its properties. We consider a synthetic antiferromagnet in which the lower permalloy layer is magnetised positively (relative to the film), and the top CoFeB layer is magnetised negatively. (This is opposite of what was analysed in the previous section: the net magnetisation of the resonator is antiparallel to that in the film). The layers are again 20 nm and 15 nm thick, but the length and width are made smaller:  $120 \times 200$  nm. The lowest modes of an isolated resonator are at 4.10 GHz and 8.57 GHz. The near-field approximation yields the resonant frequencies listed in Table ???. The intrinsic widths of the modes are  $0.3 \text{ ns}^{-1}$  and  $0.4 \text{ ns}^{-1}$ , respectively, and they are only weakly affected by the coupling. An interesting trend is that the dark mode goes up in frequency as the spacing is decreased.

The radiative linewidths for both modes are shown in Fig. ???. One can see that the emission rate for the quasiuniform mode exhibits a peak and then falls off, presumably due to the formfactor and the exponential decay. The behaviour of the emission from the dark mode is somewhat similar, with a minimum between 3 and 4 GHz, which probably reflects destructive interference between waves emitted by the two opposite endpoints. One can see that for the quasiuniform mode the emission rate becomes comparable with the intrinsic linewidth at narrow separations.

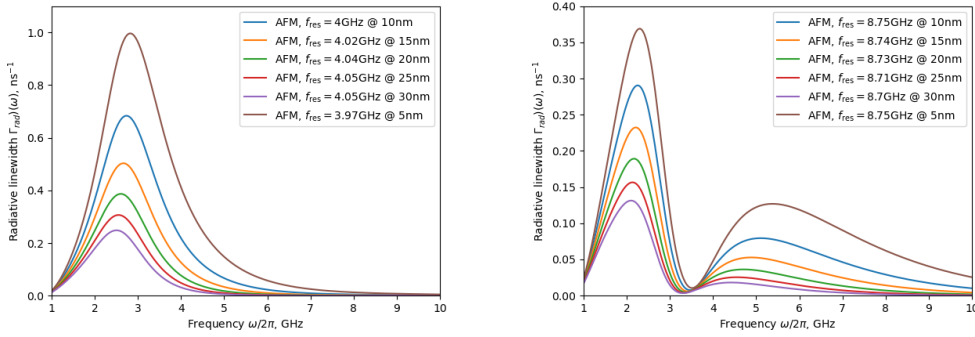


Figure VI.28: Radiative linewidth for the 4 GHz quasi-uniform mode (left) and 8 GHz dark mode (right) for several values of the spacing.

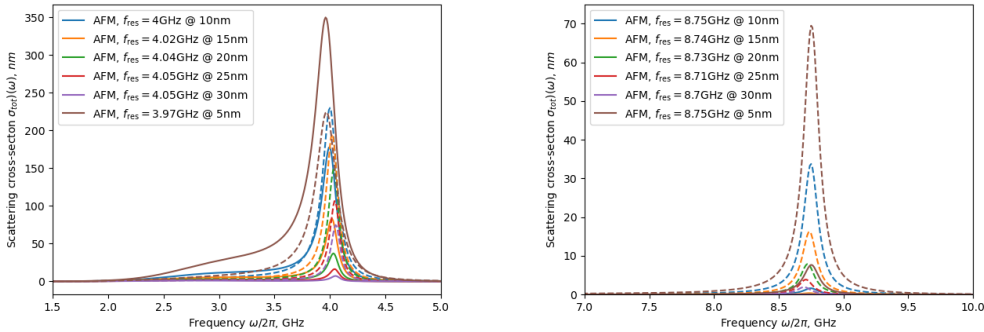


Figure VI.29: Scattering (solid) and absorption (dashed) cross-sections for the 4 GHz quasi-uniform mode (left) and 8 GHz dark mode (right) for several values of the spacing.

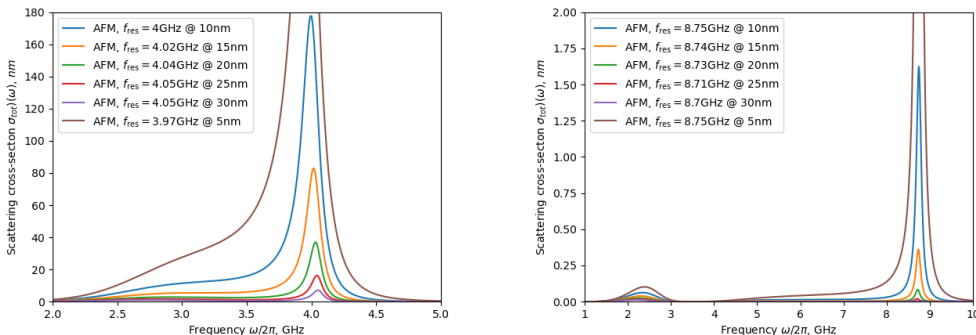


Figure VI.30: Total scattering cross-sections for the 4 GHz quasi-uniform mode (left) and 8 GHz dark mode (right) for several values of the spacing.

The scattering and absorption cross-sections are shown in Fig. ???. One can see that the 8 GHz mode is predominantly absorbed, while the 4 GHz mode is predominantly scattered if the spacing is less than 15 nm. An asymmetric shoulder in the cross-section is due to increase of  $\Gamma_{\text{rad}}(\omega)$  with  $\omega$  at low frequencies, and its rapid falloff at higher frequencies. For bettered readability, total scattering cross-sections are also shown in Fig. ???. One may notice a spurious peak in the scattering by the dark mode. This is due to the maximum in the emission rate and not related to a resonant level.

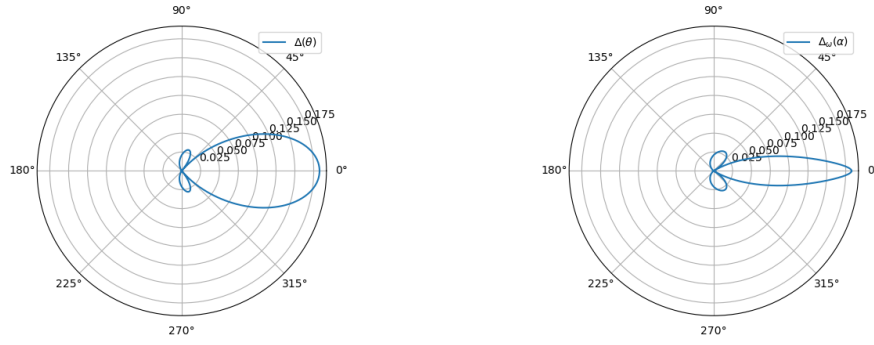


Figure VI.31: Directivity of the coupling  $\Delta_\theta$  is shown as a function of  $k$ -space angle  $\theta$  (left) and real-space angle  $\alpha$  (right) for the 4 GHz resonant mode at  $s = 15$  nm.

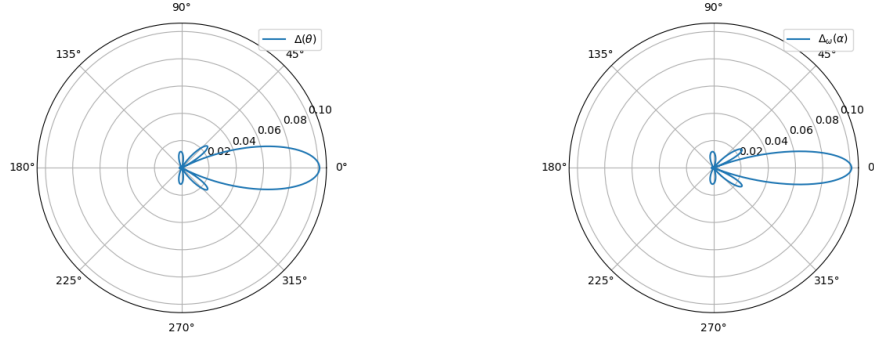


Figure VI.32: Directivity of the coupling  $\Delta_\theta$  is shown as a function of  $k$ -space angle  $\theta$  (left) and real-space angle  $\alpha$  (right) for the 8 GHz resonant mode at  $s = 10$  nm.

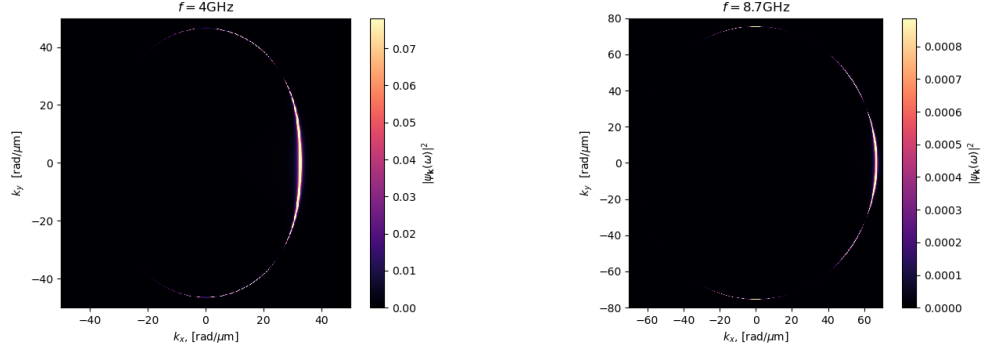


Figure VI.33: Scattered wave in the  $k$ -space. Left: quasi-uniform mode for  $s = 15$  nm,  $f = 4$  GHz. Right: dark mode, for  $s = 10$  nm,  $f = 8.7$  GHz.

Directivity of hybridisation, both in the  $k$ -space ( $\Delta_\theta$ ) and in the real space ( $\Delta(\alpha)$ ) are shown in Fig. ?? and ???. One can see that the emission still occurs predominantly in the forward direction.

The distribution of intensity in the  $k$ -space is shown in Fig. ???. One can see that a better coverage of the constant-frequency contour is achieved, but the two zeros due to the formfactor are still visible.

It may be interesting to compare this case with what happens when the magnetisation in the synthetic antiferromagnet is aligned parallel with that of the film.

Spacing $s$	Mode 0, GHz	Mode 1, GHz
$\infty$	4.06	8.49
30 nm	4.00	7.84
25 nm	3.98	7.67
20 nm	3.97	7.44
15 nm	3.94	7.10
10 nm	3.90	6.62
5 nm	3.84	5.94

Table VI.6: Resonant frequencies from the near-field approximation for a  $120 \times 200$  nm synthetic antiferromagnet in which net magnetisation is parallel to that in the film.

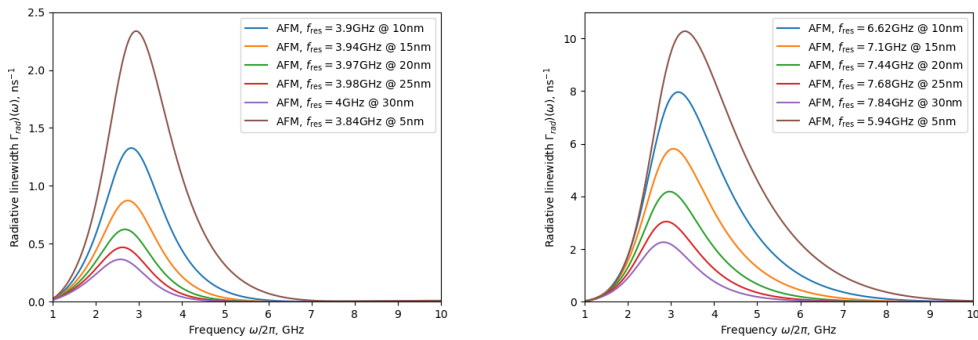


Figure VI.34: Radiative linewidth for the 4 GHz quasi-uniform mode (left) and 8 GHz dark mode (right) for several values of the spacing.

The respective mode frequencies are listed in Table ???. Unlike Table ??, the dark mode is rapidly downshifted in frequency when the resonator is brought into proximity with the film. The relevant radiative rates shown in Fig. ?? behave similarly, but are noticeably higher, which indicates a rather strong coupling, especially for the dark mode. (The strong downshift of this mode is likely to be the consequence of this strong coupling.)

The respective scattering cross-sections are shown in Fig. ???. Again, an asymmetric shoulder of the 4 GHz mode is due to a maximum in the radiative rate. More interestingly, the cross-section for the dark mode exhibits a rather strong secondary maximum for the same reason. The strong coupling to the dark mode is seen in the contribution to the cross-section that exceeds the one from the quasi-uniform mode.

The respective directivity patterns are rather similar to Figs. ?? and ?? and are not given here.

We thus see that small resonators provide a stronger large-angle scattering, and their coupling may be sufficiently strong for the scattering to dominate over absorption.

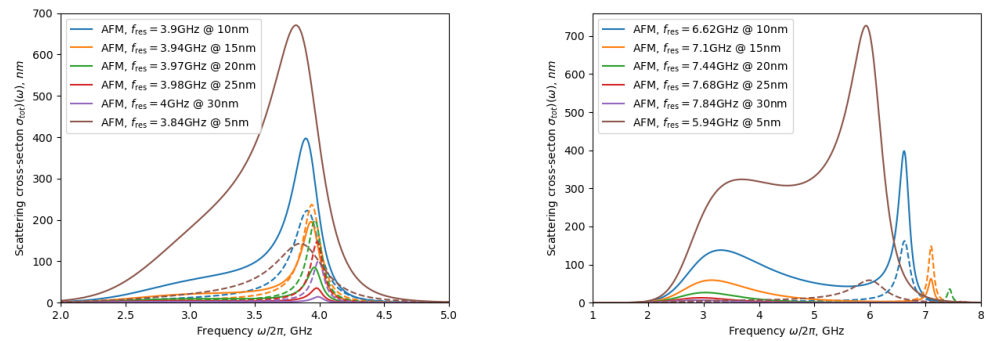


Figure VI.35: Scattering (solid) and absorption (dashed) cross-sections for the 4 GHz quasi-uniform mode (left) and 8 GHz dark mode (right) for several values of the spacing. Parallel net magnetisation assumed.

## Chapter VII

# Outlook: nonlinear multidimensional resonators

The concepts developed in these notes allow one to analyse dynamics of a multidimensional nonlinear resonator embedded into a linear medium. Indeed, only dynamics of the resonant mode is modified by the nonlinearity. Hence, the scattered waves can be eliminated in the same way as in Sec. IV.4, resulting in the self-energy contribution, so that the dynamics of the local mode  $\varphi$  is given by

$$i\dot{\varphi} - (\Omega_0 - i\Gamma_0)\varphi - \Sigma(\hat{\omega})\varphi - \lambda_\varphi|\varphi|^2\varphi = \Delta_{\text{inc}}A_{\text{inc}}(t) , \quad (\text{VII.0.1})$$

where  $\Sigma(\omega)$  is the self-energy part. To study the temporal dynamics, one should interpret the frequency  $\omega$  as a differential operator:

$$\hat{\omega} = i\frac{\partial}{\partial t} . \quad (\text{VII.0.2})$$

To study the response to a monochromatic incident wave, one may write  $\varphi = \varphi_0 \exp(-i\omega t)$ , and obtain an equation for the amplitude  $\varphi_0$ :

$$[\omega - \Omega_0 + i\Gamma_0 - \Sigma(\omega) - \lambda_\varphi|\varphi_0|^2]\varphi_0 = \Delta_{\text{inc}}A_{\text{inc}} . \quad (\text{VII.0.3})$$

Near the resonance, one may expand the self-energy part as explained in Sec. IV.4:

$$[Z_{\text{res}}^{-1}(\omega - \Omega_{\text{res}}) + i\Gamma_{\text{res}} - \lambda_\varphi|\varphi_0|^2]\varphi = \Delta_{\text{inc}}A_{\text{inc}} . \quad (\text{VII.0.4})$$

Here the resonant frequency  $\Omega_{\text{res}}$ , the linewidth  $\Gamma_{\text{res}}$  and the pole residue  $Z_{\text{res}}$  are given by Eqs. (IV.4.7), (IV.4.8) and (IV.4.11). Eq. (??) makes the resulting problem completely equivalent to the one considered in Ch. III, cf. Eq. (III.3.4). The nonlinear frequency shift is given by  $Z_{\text{res}}\lambda_\varphi|\varphi_0|^2$ , where the mode amplitude  $|\varphi_0|$  is again given by the solution to the cubic equation (III.3.5). As in Sec. III.3, this results in a bistability at sufficiently high driving amplitudes. Then, the scattered wave is given by Eq. (IV.2.19)

$$\psi_{\mathbf{k}}^{(\text{scat})} = G_{\mathbf{k}}(\omega)\Delta_{\mathbf{k}}\varphi_0 , \quad (\text{VII.0.5})$$

where  $G_{\mathbf{k}}(\omega)$  is Green's function (IV.2.2) of the medium. In real space, the long-distance behaviour of the scattered wave can be computed with the help of results

of Sec. IV.2, see Eq. (IV.2.19). The similarity suggests that most of the conclusions of Ch. III can be carried directly into the multidimensional context.

Thus, all the components required to model dynamics of neurons and their mutual influence are included in this report. A system of coupled neurons is described by the system of equations

$$\left[ i\partial_t - \Omega_i + i\Gamma_i - \lambda_i |\varphi_i|^2 \right] \varphi_i = \Phi_i(t) + \sum_{j \neq i} \int_0^t dt' w_{ij}(t-t') \varphi_j(t') , \quad (\text{VII.0.6})$$

where  $\Omega_i$  is the resonant frequency of  $i$ th neuron described by  $\varphi_i(t)$ ,  $\Gamma_i$  the respective linewidth,  $\lambda_i$  the nonlinearity parameter. The external source  $\Phi_i(t)$  can be linked to the incident wave(s)  $I_{\mathbf{k}}(t, \mathbf{r})$  as

$$\Phi_i(t) = \sum_{\mathbf{k}} I_{\mathbf{k}}(t, \mathbf{r}_i) \bar{\Delta}_{i,\mathbf{k}} . \quad (\text{VII.0.7})$$

The last term with weights  $w_{ij}(t-t')$  describes how neurons influence each other.

The weights  $w_{ij}(t-t')$  of the network are, in general, non-local retarded kernels (i.e.,  $w_{ij}(t-t') \neq 0$  only for  $t > t'$ ). Whether the respective delays are important or not, depends upon how the information is conveyed in the signal, i.e., the modulation/multiplexing methods. The kernels can be obtained from their Fourier images  $w_{ij}(\omega)$ :

$$w_{ij}(t-t') = \int_{-\infty}^{\infty} \frac{d\omega}{2\pi} w_{ij,\omega} e^{-i\omega(t-t')} . \quad (\text{VII.0.8})$$

When the delays are irrelevant, one can replace  $\omega$  by the respective carrier frequency, but in general  $\omega$ -dependence must be retained. For a given frequency  $\omega$ , the quantity  $w_{ij,\omega}$  is given by a sum over all possible modes propagating between the nodes at positions  $\mathbf{r}_i$  and  $\mathbf{r}_j$ :

$$w_{ij,\omega} = \sum_{\mathbf{k}} \bar{\Delta}_{i,\mathbf{k}} G_{\mathbf{k}}(\omega) \Delta_{j,\mathbf{k}} e^{i\mathbf{k} \cdot (\mathbf{r}_i - \mathbf{r}_j)} . \quad (\text{VII.0.9})$$

Here  $\Delta_{i,\mathbf{k}}$  are the hybridisation couplings between the mode at wavevector  $\mathbf{k}$  and a neuron at position  $\mathbf{r}_i$ . One may also employ the expression (IV.2.1). Integration over frequencies then amounts to closing the contour in the lower half-plane to catch the pole at  $\omega = \omega_{\mathbf{k}} - i\gamma_{\mathbf{k}}$ . This is only allowed if  $t > t'$ , which makes the coupling retarded. The pole contribution yields

$$w_{ij}(t > t') = -i \sum_{\mathbf{k}} \bar{\Delta}_{i,\mathbf{k}} \Delta_{j,\mathbf{k}} e^{i\mathbf{k} \cdot (\mathbf{r}_i - \mathbf{r}_j) - i\omega_{\mathbf{k}}(t-t') - \gamma_{\mathbf{k}}(t-t')} . \quad (\text{VII.0.10})$$

If the neurons are more than a wavelength apart, they communicate predominantly via the far field. One can employ the fact that Green's function is peaked at the dispersion contour  $k_{\omega}(\theta)$ , and the expression for the weights can be recast in the form discussed in Sec. IV.3:

$$w_{ij,\omega}^{(\text{far})} = \bar{\Delta}_{i,\mathbf{K}(i,j)} G(\omega, \mathbf{r}_i - \mathbf{r}_j) \Delta_{j,\mathbf{K}(i,j)} , \quad (\text{VII.0.11})$$

with the wavevector  $\mathbf{K}(i, j)$  chosen so that the group velocity  $\mathbf{v}_{\mathbf{K}(i,j)} \parallel \mathbf{r}_i - \mathbf{r}_j$  (see the definition of  $\theta^*$  in Eq. (IV.2.11)), and the real-space Green's function  $G(\omega, \mathbf{r})$  given by Eq. (IV.2.19). We see that in this approximation time-dependence of the

weight  $w_{ij}(t - t')$  reproduces that of  $G(t - t', \mathbf{r}_i - \mathbf{r}_j)$  given by Eq. (IV.3.7). In particular, one can expect the wave to be delayed by propagation time

$$\tau_{ij} \equiv \frac{|\mathbf{r}_i - \mathbf{r}_j|}{|v_{\mathbf{K}}(i, j)|}. \quad (\text{VII.0.12})$$

The respective r.h.s. is then

$$\begin{aligned} \int w_{ij}(t - t') \varphi_j(t') dt' &= \bar{\Delta}_{i,\mathbf{K}(i,j)} G(\omega, \mathbf{r}_i - \mathbf{r}_j) \Delta_{j,\mathbf{K}(i,j)} \varphi_j(t - \tau_{ij}) \\ &= W_{ij} \varphi(t - \tau_{ij}) \end{aligned} \quad (\text{VII.0.13})$$

with

$$\begin{aligned} W_{ij} &= \bar{\Delta}_{i,\mathbf{K}(i,j)} \Delta_{j,\mathbf{K}(i,j)} \left[ \frac{|\mathbf{K}(i, j)|}{2\pi i u_{\omega}(\mathbf{K}(i, j)) v_{\omega}(\mathbf{K}(i, j))} \frac{d\theta^*}{d\alpha} \right]^{1/2} \\ &\times \frac{1}{\sqrt{|\mathbf{r}_i - \mathbf{r}_j|}} \exp(i\mathbf{K}(i, j) \cdot (\mathbf{r}_i - \mathbf{r}_j)). \end{aligned} \quad (\text{VII.0.14})$$

The frequency  $\omega$  here should be understood as the carrier frequency. One may notice a significant enhancement of the weight if the wave propagates along the caustic,  $d\alpha/d\theta^* \approx 0$ . However, in this regime the frequency dependence is also strong, which may result in an untolerable distortion of the signal.

Neurons placed at short distances from each other communicate via near fields, and the delays can be mostly ignored. This way, one obtains the weights

$$w_{ij,\omega}^{(\text{near})} = \sum_{\mathbf{k}} \frac{\bar{\Delta}_{i,\mathbf{k}} \Delta_{j,\mathbf{k}}}{\omega_{\mathbf{k}}} e^{i\mathbf{k} \cdot (\mathbf{r}_i - \mathbf{r}_j)}. \quad (\text{VII.0.15})$$

Since the weight  $w_{ij}(\omega)$  is independent of  $\omega$ , its Fourier image in time domain amounts to a delta-function (see Eq. IV.3.10):

$$\int dt' w_{ij}(t - t') \varphi_j(t') = w_{ij}^{(\text{near})} \varphi_j(t). \quad (\text{VII.0.16})$$

(One may also include the next term proportional to  $\dot{\varphi}_j$ , see Sec. IV.3.)

Thus, we see that the system of neurons in general is described by the system of nonlinear differential equations with a non-local kernel. At long distances, this becomes the system of delayed differential equations, while at short distances it reduces to ordinary differential equations. At intermediate distances,  $k_{\omega} r \sim 1$ , one should use a generic nonlocal kernel.